Structural and optical properties of transition-metal compounds under pressure

Dissertation zur Erlangung des Doktorgrades
der Mathematisch-Naturwissenschaftlichen
Fakultät der Universität Augsburg

vorgelegt von
Kaneez Rabia

May 2012

Erstgutachter: Prof. Dr. C.A. Kuntscher
Zweitgutachter: Prof. Dr. A. Loidl

Tag der mündlichen Prüfung:10 May 2012

Contents

1 Introduction

Transition-metal compounds (especially oxides) are the most studied compounds in condensed matter physics due to their interesting physical phenomena, like a Mott insulating state, high-T_c superconductivity, ferromagnetism, antiferromagnetism, ferroelectricity, antiferroelectricity, charge ordering, etc. The main role in these phenomena is played by the d-orbital valence electrons of the transition metal ions. The strong electronic-correlations due to the spatial confinement in narrow d-orbitals play an important role in the properties of these materials. The internal degrees of freedom of d-electrons, i.e., charge, spin and orbital angular momentum and the lattice degrees of freedom form a delicate balance and therefore d-electron systems are highly susceptible to any external influence such as temperature, pressure, magnetic field, or doping, which can switch the material to a new phase. Moreover the orbital degeneracy in d-electron system is an important and unavoidable source of their complicated behavior.

Pressure is an important parameter affecting the electronic and the structural properties of the system. The external pressure is considered to be a cleaner way to tune the properties of the material compared to chemical pressure (doping) which additionally affects the translational symmetry of the crystal lattice and adds impurities during substitution. The compression induced by the external pressure changes the atomic separation and bandwidth of the electronic states. Infrared spectroscopy (IR) is a powerful method to investigate the electronic and vibrational properties of transition-metal compounds. In combination with the pressure technique it is an indispensable tool for investigating pressure-induced changes in the electronic structure of solids.

The development of new advanced materials is essential for progress in modern science and technology. Magnetoelectric materials are the new class of materials characterized by the coexistence of interrelated electric and magnetic dipole structures within a certain range of temperatures. This unique feature makes these materials potential candidates for many new applications in the fields of transducers, sensors and data storage. Among transition-metal oxides, the perovskite $BiFeO_3$ is a robust magnetoelectric multiferroic, with the coexistence of ferroelectric and antiferromagnetic order up to unusually high temperatures. It exhibits an antiferromagnetic Néel temperature

of ≈370°C and a ferroelectric Curie temperature of ≈830°C. Although the multiferroic materials have been studied extensively, only very little is known about the effect of external pressure on their multiferroic properties. In $BiFeO_3$ various instabilities can be driven by external thermodynamical variables, like temperature, pressure, electric or magnetic field. As a part of this thesis, the structural phase transitions in $BiFeO_3$ probed by using far-infrared spectroscopy are presented.

Since many of the spinels are common minerals, they also have great geological and geophysical interest; especially chromium spinel is regarded as important petrogenetic indicator in ultramafic to mafic rocks [1]. Some chromium spinels, e.g; $HgCr_2S_4$ and $CdCr_2S_4$ exhibit multiferroic behaviour. Chromium spinels with a general formula ACr_2X_4, where A= Zn, Cd, or Hg is a divalent nonmagnetic cation and X= O, S, or Se is a divalent anion are investigated. The Cr^{3+} ion is in the $3d^3$ configuration, its three 3d electrons occupy the t_{2g} levels with total spin S=3/2. The Cr-sublattice is formed by corner sharing tetrahedra named as pyrochlore lattice which exhibits a highly frustrated geometry of antiferromagnetically coupled spins. Although charge and orbital degrees of freedom in the ACr_2X_4 spinels are frozen, these compounds show a wide variety of magnetic properties ranging from those of a strongly frustrated antiferromagnet (AFM) to a Heisenberg ferromagnet (FM). In the ACr_2O_4 spinels, AFM nearest-neighbor interactions between Cr spins residing on a pyrochlore lattice are geometrically frustrated. The magnetic ground state of a frustrated antiferromagnet is highly degenerate which leads to unusual low-temperature properties. In this project three chromium spinel compounds: $ZnCr_2Se_4$, $HgCr_2S_4$ and $CdCr_2O_4$ were investigated.

Among vanadium spinels, ZnV_2O_4 and MgV_2O_4 were investigated. In these systems the V^{3+} with electronic configuration $3d^2$ has spin S=1. The two spins occupy the triply degenerate t_{2g} orbitals and the orbital degree of freedom is unfrozen in the system. The ZnV_2O_4 and MgV_2O_4 are Mott-Hubbard insulators in the crossover regime between the localized and itinerant limit, i.e., the on-site Coulomb repulsion and the bandwidth are comparable. The insulator-to-metal transition is induced by reducing the V-V distance, accomplished by applying external pressure.

The β-vanadium bronzes are typical examples of highly correlated electron systems. These compounds are represented as $\beta-A_xV_2O_5$ (A = Li, Na, Ag, Ca, Sr, and Pb) and are mixed-valent oxides with $V^{4+}(3d^1)$ and V^{5+} $(3d^0)$. The β-vanadium bronzes with stoichiometric composition x=1/3 crystallize in a monoclinic tunnel-like structure with space group C2/m. $\beta-Na_{0.33}V_2O_5$ is one of the best conductor among vanadium bronzes. In this project the pressure-dependent structural properties of the $\beta-Na_{0.33}V_2O_5$ at room temperature are investigated by high-resolution angle-

dispersive powder X-ray diffraction.

In many transition metal compounds most often the electronic excitations occur in visible (Vis) and ultraviolet (UV) energy range. In this thesis, the invesitigated Cr-spinel compounds exhibits the crystal-field d-d excitations and charge transfer excitations, which lie in this higher energy range. With the present investigated technique we could cover the energy up to 3 eV, thus, the energy of all spin allowed d-d transitions was not accessible. Since pressure affects the electronic states to a large extent, one can get a lot of information about electronic system if the range above 3 eV would be accessible for high-pressure technique. For this purpose, a part of the PhD project was devoted to the extension of pressure-dependent measurements in the Vis-UV frequency range. Thus, the Vis-UV microspectrometer was constructed for reflection and transmission measurements under pressure and at low temperatures. The test measurements in transmission mode at ambient conditions were done successfully, due to time constraints the pressure-dependent measurements were not carried out.

The contents of this dissertation are in the following sequence. The introduction to experimental techniques i.e., high pressure infrared microspectroscopy and high pressure X-ray diffraction are presented in Chapter 2. In Chapter 3, the design and construction of Vis-UV microspectrometer and test measurements are presented. The effect of external pressure on the crystal structure of $\beta-Na_{0.33}V_2O_5$ probed by X-ray diffraction measurement is presented in Chapter 4. In Chapter 5, the crystal structure and physical properties of perovskite materials, specifically the perovskite multiferroic $BiFeO_3$ and its experimental investigation by infrared spectroscopy under pressure are presented. The crystal structure of spinels and the pressure induced phenomena in the various chromium spinels and vanadium spinels are presented in Chapter 6.

2 Experimental Techniques

2.1 Fourier Transform Infrared(FTIR) Spectrometer

The FTIR spectrometer Bruker IFS66v/S is used in this work. This spectrometer covers a wide spectral region from 10-25000 cm^{-1}, i.e., far-infrared (FIR) to visible frequencies. The instrument is enclosed in a vacuum bench to eliminate the absorption features due to the CO_2 and H_2O in the mid-infrared range. Its main advantage occurs, when large number of scans are required of both sample and background for low frequency measurements. During this measurement, the change in air quality can introduce significant artifacts in the resulting spectra. Its optical layout is shown in Figure 2.1.

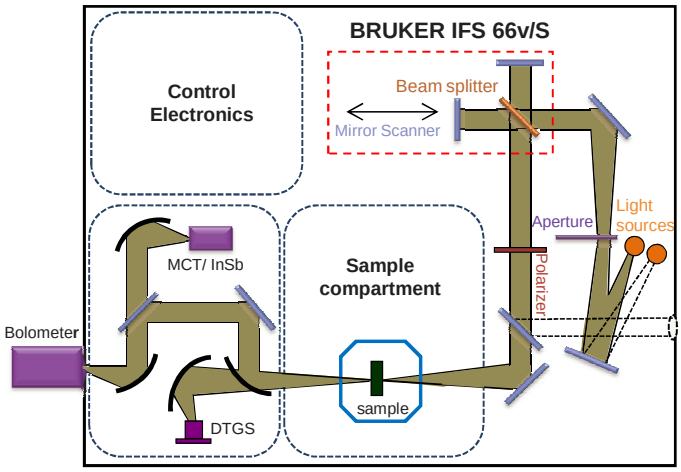

Figure 2.1: *Optical layout of a Bruker IFS66v/S Fourier transform infrared spectrometer.*

The light sources which are desired for different frequency ranges are given in Table 2.1 along with the obtained energy range and the required detectors and beamsplitters for the specified range. The beam from the sources passes through the aperture prior to entering the interferometer. The alignment of the interferometer is crucial and it is different for each beamsplitter, the controlling software is programmed with the

precise adjustments, made via stepper motor control of the stationary mirror. The center of each beamsplitter is partially silvered to act as a beamsplitter for a He-Ne laser beam that tracks the moving mirror. The moving mirror rides on a cushion of nitrogen gas to ensure smooth and reproducible movement. After leaving the interferometer block the infrared beam enters the sample chamber. For a simple transmission measurement the beam directly passes through the sample and enters the detector through some optical path, its paths toward different detectors are shown in Figure 2.1.

Table 2.1: *Different sources, beamsplitters, and detectors used in the Fourier transform spectrometer for measurements in various infrared frequency ranges.*

Frequency range	Source	Beamsplitter	Detector
Far-infrared 10 - 700 cm^{-1}	Hg discharge lamp	50 μm Mylar/Ge 23 μm 6 μm	Bolometer DTGS
Mid-infrared 500 - 8000 cm^{-1}	Globar	KBr/Ge	MCT DTGS
Near-infrared 2000 - 12000 cm^{-1}	Tungsten lamp	CaF_2	InSb
Visible/UV 10000 - 26000 cm^{-1}	Tungsten lamp	CaF_2	Si diode GaP diode

2.1.1 Working Principle of FTIR spectrometer

The FTIR spectrometer is based on the Michelson interferometer, its working principle is shown in Figure 2.2. The main parts of the Michelson interferometer are the fixed mirror, the movable mirror, and the beam splitter, which is fixed. The beam from the source is directed towards the beamsplitter, where the beam is divided into two parts. One half of the beam is reflected towards the fixed mirror and the other half of the beam is transmitted towards a movable mirror, which scans along the beam direction. Both parts of the beam are then reflected by mirrors and recombined (interference) at the beamsplitter. This recombined beam is directed through the sample and focused on the detector.

A laser beam undergoing the same change of the optical path as an infrared beam, serves to control the position of the mirror during the scan and initiates the collection of data points from the signal of the infrared detector at uniform intervals of mirror travel. The data points are digitalized by an analog to digital converter and stored in a computer memory. The result is an interferogram, i.e. a record of the signal of

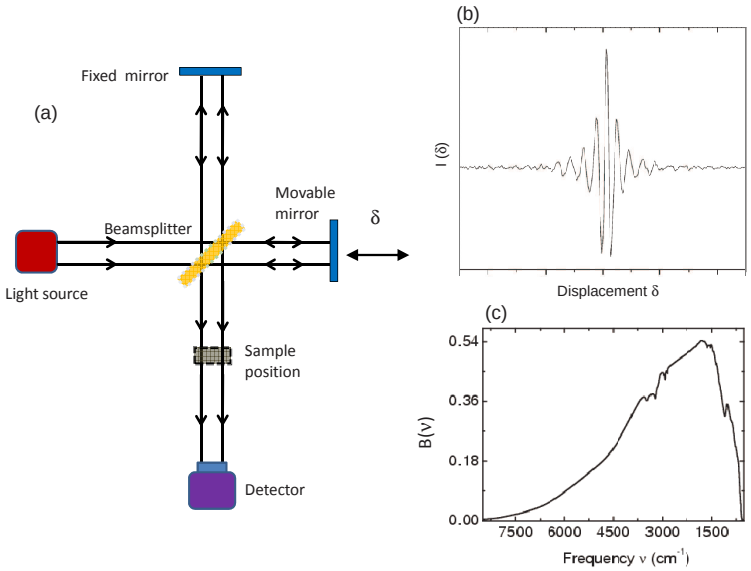

Figure 2.2: *(a)Schematic illustration of the Michelson Interferometer which explains the working principle of a FTIR spectrometer. (b) Interferogram in a broad frequency range (c) and the spectrum obtained after the Fourier transformation procedure.*

the infrared detector as a function of the optical path difference (δ) for the two beams in the interferometer (see Figure 2.2(b)). When the mirror scans, the δ varies and as a resultant an interferogram is produced. The maxima occur when δ is an integral multiple of wavelengths (i.e., δ=nλ; n=0,$\pm$1,$\pm$2, etc.). The minima occur when δ is an odd multiple or half wavelengths (i.e., δ=[(n+$\frac{1}{2}$)λ]). An ideal interferogram with a continuum source can be represented by the integral

$$I(\delta) = \int_0^\infty B(\nu) cos(2\pi\delta\nu) d\nu. \tag{2.1}$$

Therefore the interferogram implicitly contains information over the whole frequency dependence of light and its Fourier transform $B(\nu)$ is the power spectrum of the radiation. The Fourier transformation is performed on the interferogram using the following mathematical formula

$$B(\nu) = \int_0^\infty I(\delta) cos(2\pi\delta\nu) d\nu. \tag{2.2}$$

The Fourier transformation (FT) provides the frequency distribution of the intensity. A power spectrum obtained through FT is shown in Figure 2.2(c). One of the main advantage of Fourier transform spectroscopy is that all frequencies are measured

simultaneously, thus reducing the collecting time by a factor of n (where n is the number of points in the spectrum) and improving the signal to noise ratio by a factor of $N^{\frac{1}{2}}$ when acquiring and averaging N interferograms with respect to the same spectrum acquired with dispersive techniques (Fellget advantage).

2.1.2 Infrared microspectroscopy

In this project the infrared spectroscopy under high pressure is performed using a Syassen-Holzapfel-type diamond anvil pressure cell (DAC) [2]. The commonly used method for an in-situ pressure measurement in the DAC is the ruby luminescence. For pressure measurement, the very small sample size of few 10 micron is used. The sample is placed in the hole of the gasket along with a ruby ball for pressure determination. Finally the pressure transmitting medium is added into that hole. The gasket is usually made of copper beryllium alloy or stainless steel. Before using the gasket for an experiment, it is pre-pressed to a thickness of few ten microns by the diamond anvils prior of making a hole in it. The hole in the center of the pressed gasket is drilled by an electro discharge drilling machine. The hole of $\approx 1/3$ or $2/5$ of the size of the culet should be used for relatively incompressible pressure media.

Choice of pressure transmitting media

The pressure transmitting media are selected which are transparent to the measured frequency range. The different pressure transmitting media have different hydrostaticity limits, which change with the temperature. For example at room temperature tetrahydrofuran can be used as a hydrostatic pressure transmitting medium up to 6 GPa [3], methanol-ethanol mixture solidifies at 10.5 GPa. The argon gas solidifies at a low pressure around 1.3 GPa. Helium solidifies at 12.1 GPa, but it is considered to be the best pressure transmitting medium up to 40 GPa at 300K [4]. Soft solid materials like CsI, NaCl and other related materials are also used as a pressure transmitting media. In this project, for infrared measurements, the CsI is used as a pressure transmitting medium. For X-ray diffraction (XRD) measurement helium was used as a pressure transmitting medium .

Arrangement for Pressure dependent measurements

The arrangement of the pressure-dependent measurement is shown in Figure 2.3. Measurement of a small sample in the DAC requires a sharp focusing with a large numerical aperture and a precise positioning on the surface of the sample. A standard FTIR spectrometer arrangement does not satisfy these requirements. This problem has been

solved by the use of the IR microscope coupled to the FTIR spectrometer. The main parts of the infrared microscope are two identical Schwarzschild objectives. One objective is used to focus the light on the sample and the second one serves as a condenser for transmission measurements. The basic construction and working principle of a Schwarzschild objective is described in Chapter 3.

The objectives used in the currentt setup have a magnification of 15x and a working distance of 24 mm. The sub-100 micron foci are possible with the help of Schwarzschild objectives of the microscope. To select the area of the sample for measurement, the field apertures of different sizes in the range of 0.45 - 3.75 mm are used. To view the sample in reflection and transmission mode, the visible light is incident on the sample through a remote-controlled mirror system, which makes it possible to guide the incident light in the optical path of the microscope. All the detectors mentioned in Table 2.1 can be coupled to this microscope, and the microscope can work either in reflection or transmission mode.

For a measurement the DAC is mounted in a home built holder that ensures that the DAC is always placed in the same position. This holder is fixed to the microscope sample stage that allows to finely align the DAC. The adjustable field aperture, which is mounted in the microscope is kept fixed in a way that it collects only the signal from the selected sample area in the DAC. Moreover, the mirrors that couple the microscope and the interferometer are aligned to match the focus of the IR radiation to the visible focus of the white light of the microscope, to be sure that alignment of the DAC is exactly the same for IR light. In the microscope there is a video port (camera) to make photos of the samples.

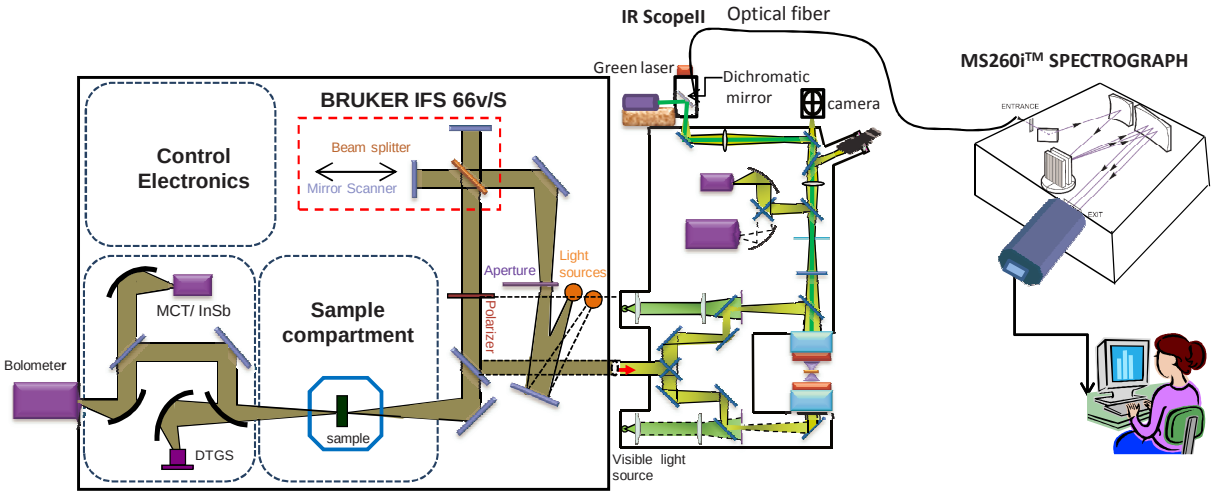

Figure 2.3: *Optical layout of the Bruker IFS66v/S Fourier transform infrared spectrometer coupled to an IR microscope illustrating the optical configuration for a pressure measurement.*

2.1.3 Pressure determination method

To determine the pressure in the cell, the green laser is shined on the ruby ball inside the DAC, and the fluorescence signal is then collected and sent through an optical fiber to a Ms260i^{TM} spectrograph equipped with a CCD camera (see Figure 2.3). The ruby is a α-Al_2O_3 crystal doped with Cr^{3+} ions which subsitute the Al^{3+} ions, coordinated with oxygen ions. The Cr^{3+} induce a trigonal distortion in the crystal because of its larger radius than Al^{3+}. The crystal field energy levels of Cr^{3+} in ruby are shown in Figure 2.4 (a). The Cr^{3+} ion in a cubic crystal field has a ground state as $^4A_2$ and its first excited state as ^2E.

When Cr^{3+} is excited by a laser, the electrons get excited from ground state $^4A_2$ towards the $^4T_2$ and $^4T_1$ [6], which populate the metastable state ^2E by non radioactive decay. From this level the electrons relax to lower energy levels under emission of radiation, namely the characteristic R (R_1, R_2) lines. The frequencies of the R lines are sensitive to temperature and pressure. Under hydrostatic pressure the ruby lattice compresses, which leads to a reduction of the Cr and O ion distance. Consequently the crystal field potential at the Cr^{3+} ions is increased and the splitting of energy levels changes. The energy gap between the metastable states and the ground state decreases and the R_1,R_2 lines shift to higher wavelength. The pressure is determined by tracing the position of the R_1 line at given experimental conditions. The relation used to calibrate the ruby pressure at room temperature is the following [7],

$$P(\Delta\lambda) = \frac{A}{B}\left[\left(1 + \frac{\Delta\lambda}{\lambda_0}\right)^B - 1\right], \tag{2.3}$$

The line shift is also temperature dependent, $\Delta\lambda$ is the wavelength shift of the R_1 line with pressure/temperature and λ_0 is the wavelength at ambient conditions. The parameters are A=1904 GPa and B=7.665. The pressure dependence of the ruby R_1 line is shown in Figure 2.4 (b).

2.1.4 Diamond Anvil Cell

The diamond anvils are produced from gem-quality and inclusion free single crystals with low birefringence, and cut in the simplified form of a brilliant (8 or 16 faces) and the working plane is produced at the culet. A very high pressure is generated in the DAC depending on the size of the culet. The culet size and the maximum pressure attained by it is inversely proportional to each other, a culet size of (0.2-0.3 mm) can generate higher pressure up to 100 GPa, a culet size of 0.6 mm can generate pressure

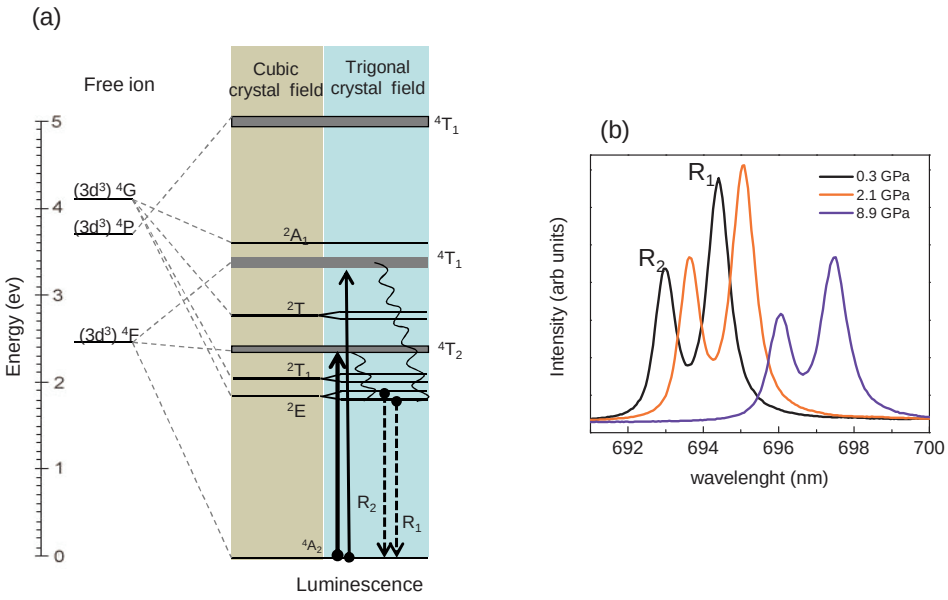

Figure 2.4: *(a) The luminescence process due to the crystal field splitting of Cr^{3+} in ruby [5]. (b) The pressured-dependence of R_1 and R_2 lines at room temperature.*

below 50 GPa, and an anvil size of 1 mm can generate pressure up to 20 GPa [3]. For the pressure study above 100 GPa or at extremely high pressures where plastic deformation is observable around the anvil surface, bevelled anvils are used [3].

Operation of DAC

The principle of operation of the DAC is very simple (see Figure 2.5). The sample is placed between flat parallel faces of two opposed diamond anvils. To obtain a hydrostatic pressure the diamonds do not press directly on the sample but compress a surrounding volume of pressure transmitting medium. There is a variety of ways to apply the load for pressure generation, depending upon the design of the cell. The mechanism of application of load is different for different types of DAC, e.g National Bureau of Standards (NBS) cell, the Basset cell, the Mao-Bell cell, the Syassen-Holzapfel cell, the membrane driven diamond anvil cell, and the Merrill-Bassett cell [8]. In this project a Syassen-Holzapfel cell is used for infrared measurements, and a membrane driven DAC is used for XRD measurement. The membrane driven DAC is explained later in this section 2.1.4.

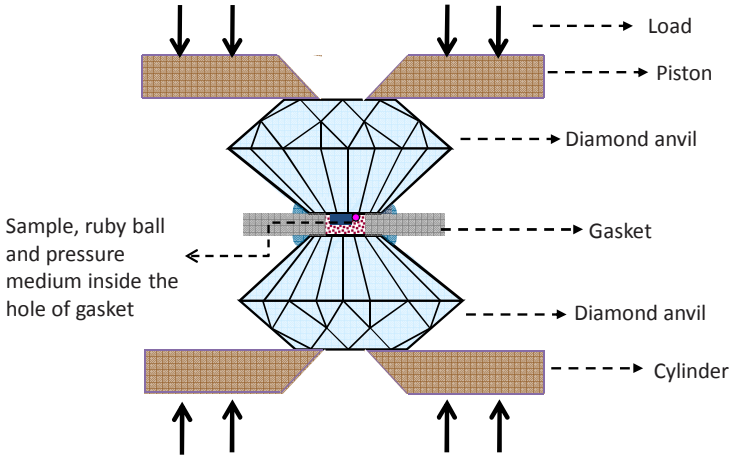

Figure 2.5: *Schematic drawing of the diamond anvil cell illustrating its operation.*

Syassen-Holzapfel DAC

The picture of the Syassen-Holzapfel DAC and its cross sectional view is shown in Figure 2.6. It is a clamped piston-cylinder cell. One of the diamond anvils is mounted in a X-Y translational stage incorporated in a fixed backing plate. The other diamond is mounted on a tilting stage in a moving piston. A tilting and translational diamond mount allows precise adjustments of the two diamond anvils with respect to each other. The force for compressing the anvils for pressure generation is produced by a thread-and-knee mechanism. A simple gear-set wrench synchronously turns two threaded rods which connect the front and back sides of the brackets and pulls the lower ends of the brackets together. Consequently, the upper ends of the bracket compress the moving piston and generate the pressure. The special geometry of this construction results in a large force multiplication. The guidance of a long moving piston assures parallelism of the diamond faces at high load, this DAC has excellent alignment stability [8].
The Syassen-Holzapfel DAC used within this project has a height of 38.7 mm and a length of $\approx$ 60 mm. The diamond anvils are made of type-IIa diamonds with a height of 1.5 mm and a culet diameter of 400 μm. The maximum pressure that can be generated in this DAC is around 25 GPa. The opening angle of the apertures at the piston and the cylinder assemblies are 40° and 50°, respectively, to minimize signal loss. A gasket made from stainless steel with an initial thickness of 0.25 mm is used in this DAC. A hole with a diameter of about 150-200 μm was drilled in the pre-indented gaskets of a thickness of about 70-80 μm, for measuring at pressures up to 10-15 GPa, and a hole with diameter of about 120 μm was used for measuring at pressures up to

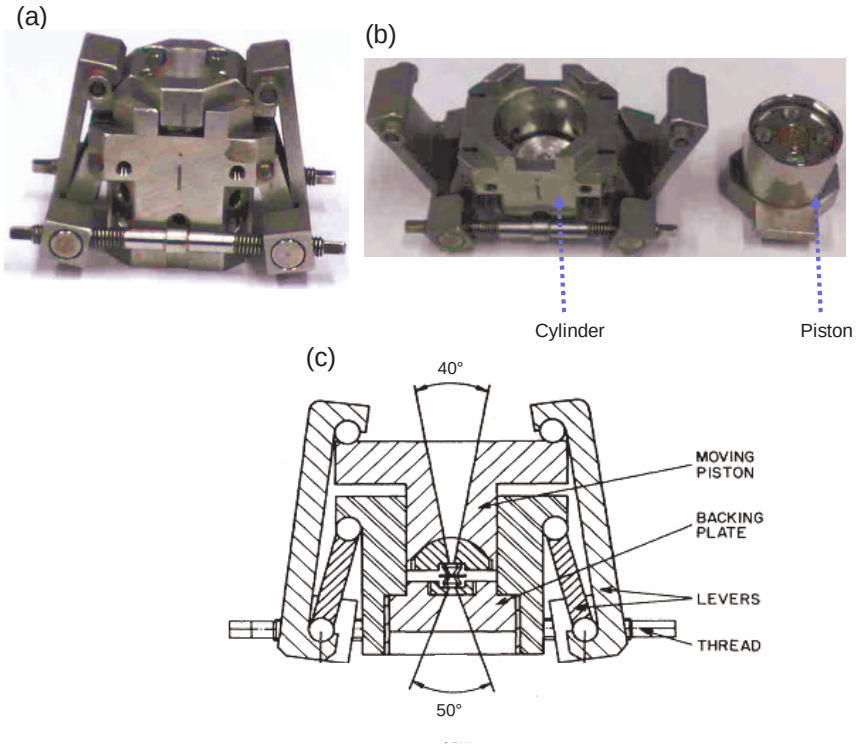

Figure 2.6: *(a) A picture of the Syassen-Holzapfel cell, (b) its two main parts, piston and cylinder, are shown. (c) Cross sectional view of the Syassen-Holzapfel pressure cell illustrating the inner construction, the figure is from Ref [9] with small modification.*

22 GPa.

Membrane-driven DAC

The typical membrane-driven DAC used for XRD is shown in Figure 2.7. The cell body is built out of 52RC maraging steel, except for the diamonds seats C and D, which are in the shape of half-spheres and made out of tungsten carbide. In Figure 2.7 (a), A is the position where the membrane is soldered, it is between the exterior case of the cell and the piston B. The force on the diamond is generated by the inflation of the membrane, which is made out of BeCu or stainless steel, the more explanation about the cell is given in Ref [10].

The schematic diagram of pressure generation in the DAC is shown in Figure 2.7 (b), where E is the gas (He) cylinder with maximum pressure of 20 MPa used as an input to inflate the membrane to apply force on the piston, F is an insulating valve, G is

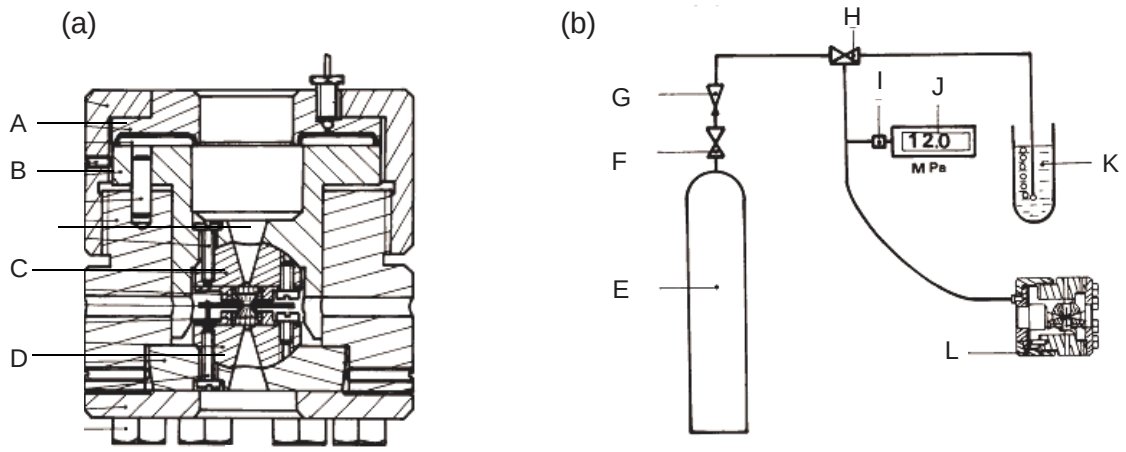

Figure 2.7: *(a) The design of the membrane DAC showing different parts, (b) schematic diagram showing how the pressure is applied in the DAC. The figure is adopted from Ref [10].*

the relief valve, and H is the double micrometeric valve used to control the pressure. The pressure is read out by a pressure gauge I, there is also a digital pressure display J. The gas leak is observed from a bubble setup K, by inserting the capillary in the alcohol. Finally, the membrane is connected with the DAC labeled as L.

The main advantage of a membrane DAC over other types of DACs where the initial external force is generated mechanically is that the gas pressure in the membrane can be monitored in-situ and precautions can be made in order to avoid high pressure, which could lead to the destruction of the cell. Another important point is that the membrane-driven DAC and the pressure regulator can be mounted so that it is not required to remove the DAC in order to change the pressure during an experiment. In this way systematic shifts of Bragg reflections, caused by inconsistencies of the position of the DAC, are prevented especially in case of single crystals.

.

2.1.5 IR properties of diamond

The DACs used for IR measurements employ type-IIa diamonds which do not contain nitrogen impurities and are insulating. The refractive index (n_{dia}) is 2.38 at 800 cm^{-1}. The dispersion of the refractive index of diamond is very small in the IR range (see Figure 2.8). The pressure effect on the refractive index of diamond is about -0.00052 /GPa [12]. Therefore the frequency- and pressure-dependence of n_{dia} and R_{dia}

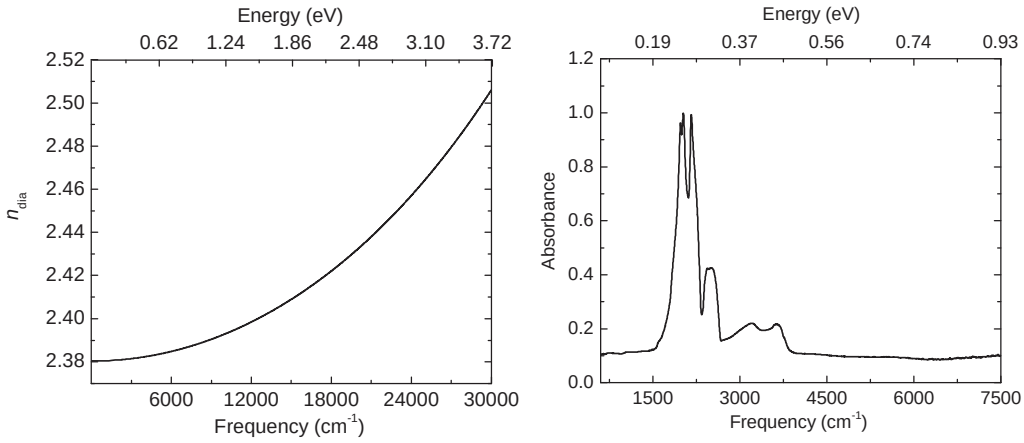

Figure 2.8: *(a) Dispersion of the refractive index of diamond in the infrared frequency range [11], (b) multiphonon excitations of the diamond in the MIR range.*

can be neglected. The IR reflectance at normal-incidence at the surface of diamond in air is given by

$$R_{\mathrm{dia}} = \left[\frac{n_{\mathrm{dia}}(\omega) - 1}{n_{\mathrm{dia}}(\omega) + 1}\right]^2. \tag{2.4}$$

The value of R_{dia} is 0.1667 using the refractive index value 2.38. There is significant multiphonon absorption in the frequency range 1700-4000 cm^{-1} (see Figure 2.8 (b)). These absorption features are discarded during the analysis of the measured data.

2.1.6 Measurement geometries

High pressure infrared reflectivity

The schematic configuration for quantitative reflectivity measurements is shown in Figure 2.9. The sample is placed in direct contact with the diamond window that faces the objective side, a solid pressure medium is used to keep the sample in contact with the diamond. The reflected intensity from the sample at sample-diamond interface is ($\mathrm{I_s}$). The intensity reflected from the diamond bottom ($\mathrm{I_b}$) is used as a reference. The reflectance spectrum at the sample-diamond interface is calculated by multiplying the ratio of the intensities $\mathrm{I_s}$ and $\mathrm{I_b}$ with the reflectivity of diamond ($\mathrm{R_{dia}}$).

$$R_{\mathrm{s-d}}(\omega) = \left[\frac{I_{\mathrm{s}}}{I_{\mathrm{b}}}\right] R_{\mathrm{dia}}. \tag{2.5}$$

However, to measure the intensity reflected from the bottom surface of the diamond is not possible during the measurement, so it can be measured only at the end of the

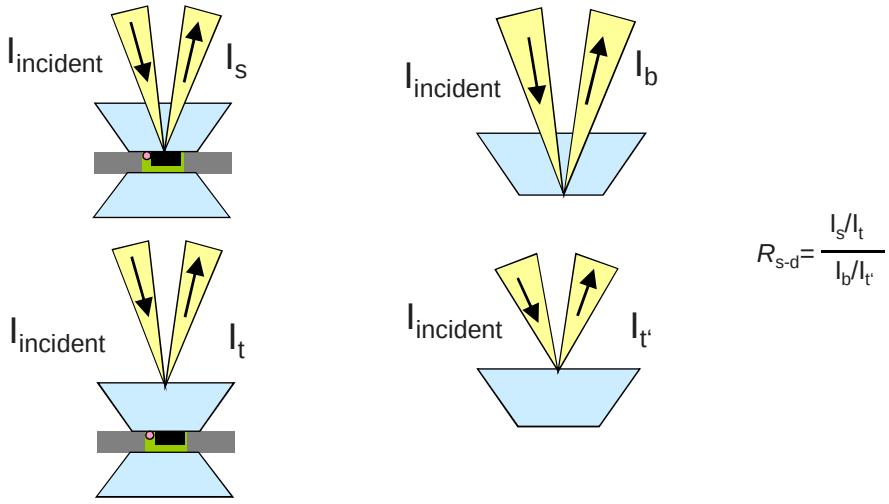

Figure 2.9: *The measurement configuration for the reflectance of a sample at the sample-diamond interface in a DAC.*

measurement. During the measurement only the intensity reflected from the diamond top (I_t) can be measured. At the end of the measurement, it is important to measure the ratio of intensities reflected from the bottom (I_b) surface of the diamond and the top ($I_{t'}$). Finally the absolute reflectivity was calculated according to the Equation 2.6.

$$R_{s-d}(\omega) = \left[\frac{I_s}{I_t} / \frac{I_b}{I_{t'}}\right] R_{dia} \tag{2.6}$$

High pressure infrared transmission

The configurations for transmission measurements are illustrated in Figure 2.10. Depending on the sample form, the reference measurements can be performed in two different ways: In case of bulk samples, the cell loading procedure is similar as for the reflectivity measurements. The sample is placed on one side of the gasket hole before filling with the pressure medium, in order to measure the reference spectrum for each measured pressure (see Figure 2.10 (a)). To calculate the transmission spectrum, the intensity transmitted through the sample (I_{sample}) is divided by the intensity transmitted through the pressure transmitting medium ($I_{reference}$) and subsequently the

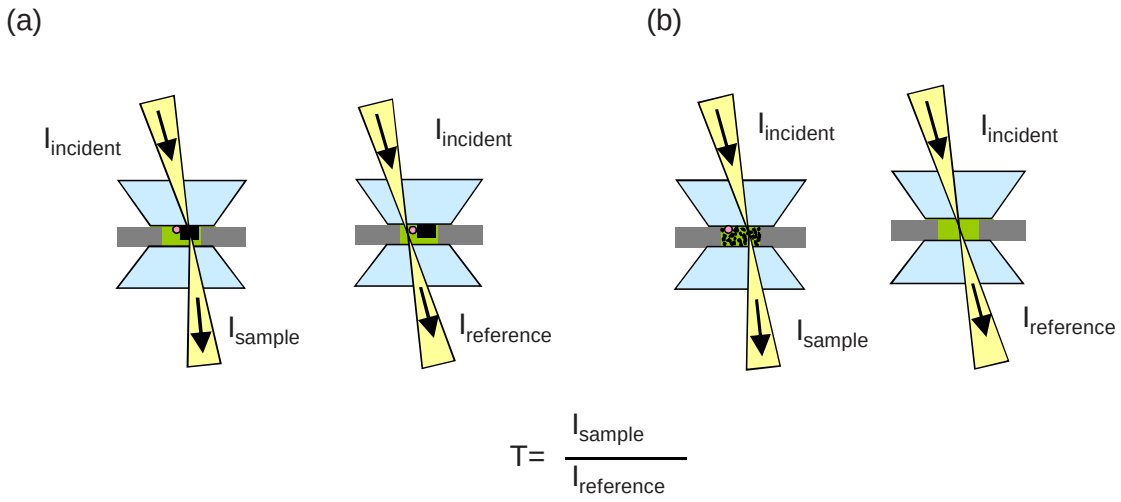

Figure 2.10: *The measurement configuration for transmission in DAC (a) for a single crystal sample or in pellet form, (b) for a powder sample.*

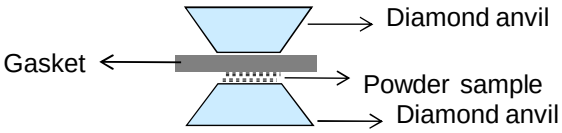

Figure 2.11: *Schematic representation of making a thin pellet out of a powder sample.*

absorption of the sample is calculated as

$$T = \frac{I_{\text{sample}}}{I_{\text{reference}}} \tag{2.7}$$

$$A = -log_{10}T \tag{2.8}$$

In case of powder samples, the cell loading process is a little bit different. There is no control while putting the sample inside the hole of the gasket and it can cover the complete area of the hole. In this case the reference can be measured at the end of the measurement by filling the cell with a solid pressure medium (see Figure 2.10 (b)). There is another way to load the cell with a powder sample. First, the pellet is made out of pure powder sample by pressing the sample in between two dimond anvils with a plane gasket, the schematic configuration is illustrated in Figure 2.11. The pellet is taken out and the DAC is cleaned. Now, the DAC is loaded again with this pellet in a similar way as for bulk samples. In this project, for the transmission measurement of ZnV_2O_4 and MgV_2O_4, the pellet made out of powder sample is used.

2.1.7 Dielectric response function

When light interacts with matter, two types of phenomena can occur: absorption and scattering processes. Light scattering can be on a macroscopic level (between interface of two types of materials, resulting in reflection and refraction) and on a microscopic level (e.g. Rayleigh and Raman scattering). These interactions have different physical origins; reflection and refraction results from a mismatch of the dielectric constants, whereas Rayleigh and Raman scattering are the result of induced polarization [13].

The propagation of the electromagnetic waves in the material is described in terms of the complex refractive index $\tilde{n}$. In case of optical parameters, the amplitude and phase shifts of the electromagnetic waves, which are transmitted through an interface or which are reflected from a boundary of two materials, constitute a response function. So we always deal with complex response function, describing the response of a system to a certain stimulus. For the optical response functions, the mathematics necessary to understand them is presented below. For more detailed information see Ref. [14–16]. The optical properties of the materials are described by the complex refractive index $\tilde{n}$:

$$\tilde{n} = n + ik, \tag{2.9}$$

where n and k are the refractive index and extinction coefficient of the material. The complex dielectric constant $\tilde{\epsilon}$ ($\tilde{\epsilon} = \epsilon_1 + i\epsilon_2$) can be determined if the refractive index is known. The relation between these two quantities is

$$\tilde{\epsilon} = \tilde{n}^2 \tag{2.10}$$

$$\epsilon_1 = n^2 - k^2 \quad ; \epsilon_2 = 2nk; \tag{2.11}$$

The complex dielectric function ($\tilde{\epsilon}$) and the complex polarizability ($\tilde{\alpha}$)are related with each other as,

$$\tilde{\epsilon} = 1 + 4\pi N\tilde{\alpha} \quad . \tag{2.12}$$

The complex polarizability is defined as

$$\tilde{\alpha}(\omega) = \frac{e^2}{m}\frac{1}{(\omega_0^2 - \omega^2) - i\gamma\omega} \quad . \tag{2.13}$$

The Equation 2.12 becomes

$$\tilde{\epsilon} = 1 + \frac{4\pi N e^2}{m}\frac{1}{(\omega_0^2 - \omega^2) - i\gamma\omega}. \tag{2.14}$$

The real and imaginary parts of the dielectric constant as a function of frequency are mutually related and illustrated in Figure 2.12. The ϵ_1 increases with increasing frequency, called normal dispersion. However, in a region near ω_0 the ϵ_1 decreases with increasing frequency, this region is called anomalous dispersion. ω_m is the frequency at which ϵ_1 is maximum or minimum. The region of anomalous dispersion is represented as γ, which is also the full width and half maximum of ϵ_2 curve. The maximum value of ϵ_2 is

$$\epsilon_2(max) = \frac{4\pi N e^2/m}{\gamma\omega_0} \quad . \tag{2.15}$$

The reflectivity (R) of a material at normal incidence is given by the Fresnel equation as:

$$R = \left|\frac{\tilde{n} - n_w}{\tilde{n} + n_w}\right|^2 \quad , \tag{2.16}$$

where n_{w} is the refractive index of the medium which forms the interface with the reflecting surface of the sample. When the medium is air or vacuum then the expression reduces to

$$R = \frac{(n-1)^2 + k^2}{(n+1)^2 + k^2} \quad . \tag{2.17}$$

For non magnetic materials,

$$n = \frac{1}{\sqrt{2}}\left(\epsilon_1 + (\epsilon_1^2 + \epsilon_2^2)^{\frac{1}{2}}\right)^{\frac{1}{2}} \quad ; k = \frac{1}{\sqrt{2}}\left(-\epsilon_1 + (\epsilon_1^2 + \epsilon_2^2)^{\frac{1}{2}}\right)^{\frac{1}{2}}. \tag{2.18}$$

The Lorentz model

The Lorentz model is the simplest model of a dielectric dispersion. It describes the resonant absorption of radiation in which the dielectric response function takes the form,

$$\epsilon(\omega) = \epsilon_\infty + \sum_j \frac{\Delta\epsilon_j \omega_{TO_j}^2}{\omega_{TO_j}^2 - \omega^2 + i\omega\gamma_j}, \tag{2.19}$$

where ω is the frequency of the incident radiation and ω_{TO_j} is the resonance frequency of the oscillator. In this model each mode is characterized by three parameters, the oscillator strength $\Delta\epsilon_j$, the frequency of transverse optical modes ω_{TOj}, and the damping of the modes γ_j. The interaction between the modes is neglected in this model. The ϵ_∞ represents the contribution at frequencies higher than the measured ones.

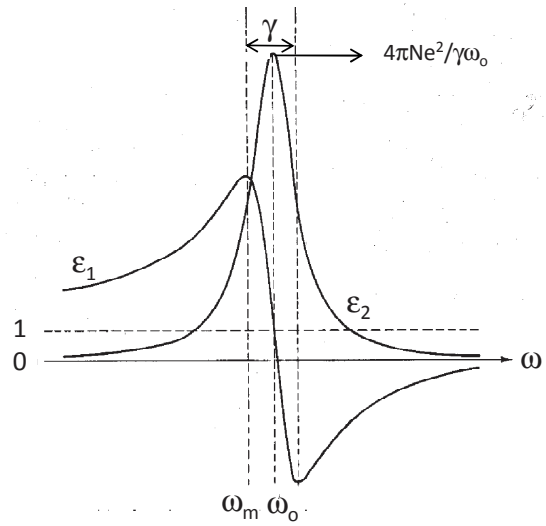

Figure 2.12: *Frequency dependence of the real $\epsilon_1(\omega)$ and imaginary $\epsilon_2(\omega)$ parts of the dielectric function for $\epsilon_{\text{inf}}>0$. The figure is taken from Ref [14] with small modification*

The 4-parameter model

The classical oscillator model (Lorentz model) often gives a wrong fitting to vibrational modes with asymmetric line shapes. In this case, it is convenient to use the factorized form of the dielectric function. The factorized model based on the frequency dependent form of the Lyddane-Sachs-Teller relation implicitly allows to couple the modes and differ the TO and LO phonon decay rates, γ_T and γ_L, respectively [17]. This is called 4-parameter model, and expressed as:

$$\epsilon(\omega) = \epsilon_\infty \prod_{j=1}^{n} \frac{\omega_{LO_j}^2 - \omega^2 + i\omega\gamma_{LO_j}}{\omega_{TO_j}^2 - \omega^2 + i\omega\gamma_{TO_j}}, \tag{2.20}$$

where ω_{TO_j} and ω_{LO_j} denote the transverse and longitudinal frequencies of the jth polar phonon mode, respectively. γ_{TO_j} and γ_{LO_j} denote the damping constants of he transverse and longitudinal jth polar phonon mode.

When fitting with this function, it is important to check that the value of complex permittivity remains positive, otherwise the parameters lose their physical significance, for example, negative losses or a finite conductivity at an infinite frequency. In the fitting procedure of the infrared reflectivity the parameter values were restricted to those which result in an optical conductivity vanishing at frequencies much higher than the phonon eigen frequencies. There are necessary conditions which should be fulfilled by

the parameters of the factorized oscillator model in order to avoid unphysical quantities. These conditions are $\omega_{LO} > \omega_{TO}$, $\gamma_{LO} \geq \gamma_{TO}$, and $\frac{\omega_{LO}^2}{\omega_{TO}^2} \geq \frac{\gamma_{LO}}{\gamma_{TO}}$.

The oscillator strength $\Delta\epsilon_j$, giving the contribution of the phonon mode to the static dielectric constant $\epsilon(0)$, can be calculated from the formula [18].

$$\Delta\epsilon_j = \frac{\epsilon_\infty}{\omega_{TO_j}^2} \frac{\prod_k (\omega_{LO_k}^2 - \omega_{TO_j}^2)}{\prod_{k \neq j} (\omega_{TO_k}^2 - \omega_{TO_j}^2)}. \tag{2.21}$$

The Kramers-Kronig Relation

The Kramers-Kronig relations are a set of equations that connect the real and imaginary parts of certain complex response functions. With this relation, the evaluation of the components of the complex dielectric constants or conductivity is possible when only one optical parameter such as reflectivity or absorbance is measured. When the reflectivity R(ω) is measured at normal incidence (over a broad energy range) on a surface covered by a transparent window, the Kramers-Kronig (KK) relation takes the form [19]

$$\phi(\omega_0) = -\frac{\omega_0}{\pi} P \int_0^{inf} \frac{\ln R_{s-d}(\omega)}{\omega^2 - \omega_0^2} d\omega + \left[\pi - 2 \arctan \frac{\omega_\beta}{\omega_0}\right], \tag{2.22}$$

where P is the principal value of the integral and ω_β is the position of the reflectivity pole on the imaginary axis in the complex frequency plane. In case of measurements on the sample-air interface, ω_β tends towards infinity and the second term vanishes. The second term is only taken into account in case of the sample-medium interface, when the refractive index of the medium is not unity, for example in the case of the sample-diamond interface. ω_β is an adjustable parameter, it is defined in such a way that the conductivity obtained by the KK analysis at low pressure coincides with the measured one of a free standing sample.

2.1.8 Synchrotron radiation facility for high pressure measurements

Synchrotron radiation is the name given to the radiation emitted when charged particles are accelerated with very high speed in a curved path or orbit. The typical energy of electrons in a synchrotron ring is of the order of a few GeV and it covers a broad spectral range from IR, visible light, UV, soft and hard X-ray regimes.

In this thesis, a part of the IR measurements under pressure, more specifically the FIR reflection measurements were performed at the synchrotron radiation facility, Angstroemquelle Karlsruhe (ANKA) at Karlsruhe, Germany. High pressure X-ray powder diffraction measurements of $\beta{-}Na_{0.33}V_2O_5$ were carried out at beam-line

ID09A in European Synchrotron Radiation Facility(ESRF) at Grenoble. The power density in the microscope plane and the signal to noise ratio are crucial parameters for high pressure IR studies with DAC. Infrared synchrotron radiation presents several advantages with respect to conventional sources other than a broad spectral range: i) high brilliance: as it is almost a point source and has higher photon flux in the far-IR, ii) emission is strongly collimated and iii) high degree of polarization. The above mentioned advantages of infrared synchrotron radiation are useful for improving the signal to noise ratio and reducing the number of acquisitions. The comparison of spectral distribution of intensity and 100 % line measured for a conventional source and synchrotron radiation are shown in Figure 2.13 (a) and (b), respectively [5].

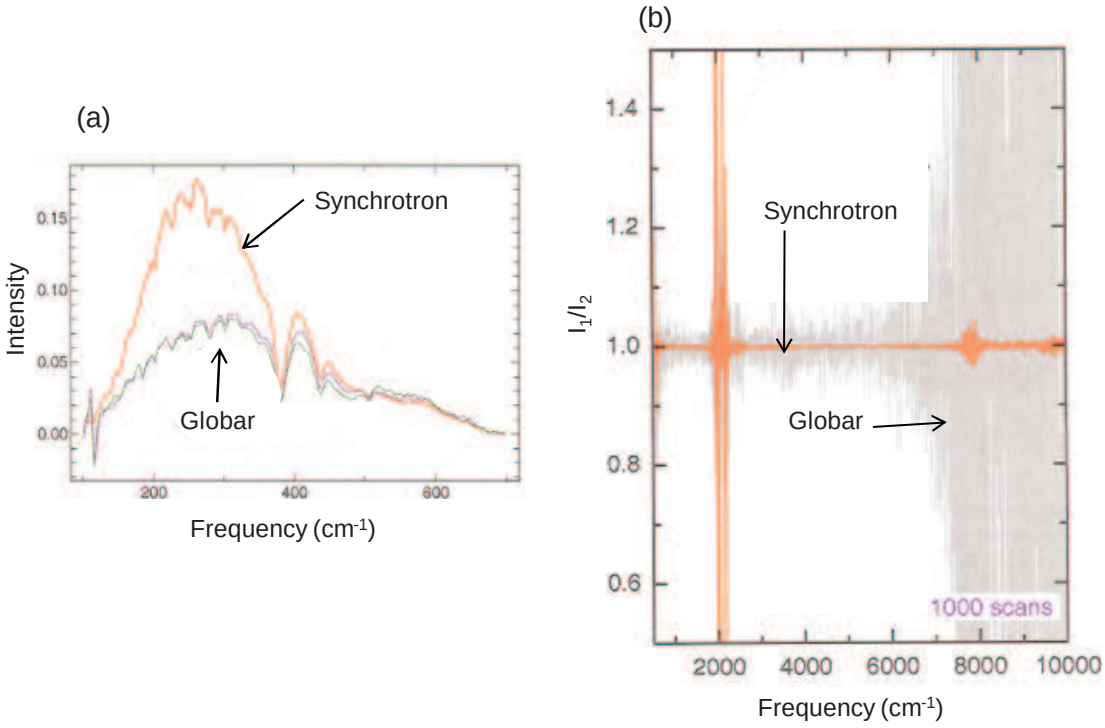

Figure 2.13: *(a)Comparison of spectral distribution of intensity measured with a bolometer for a conventional source and synchrotron radiation.(b) Comparison of 100 % lines for reflection of diamond anvil (lower inner surface) with a globar source and with synchrotron radiation, this 100 % lines correspond to a ratio of two spectra measured under identical experimental conditions. The figure is adopted from Ref [5].*

In the ANKA-IR beamline the similar instruments (Bruker IFS66v/S coupled to a IR microscope) are used, the further process to collect data is in the similar way as stated before in Section 2.1.2. The synchrotron current decays with time, therefore,

the measured spectra have to be normalized with the beam current available in a log file.

2.2 X-ray diffraction under high pressure

The X-ray powder diffraction method was first discovered by Debye and Scherrer. The first mathematical explanation of the actual positions of the X-ray diffraction spots was given by Bragg [20] and it is illustrated in Figure 2.14 where the *"A"* and *"A′"* are the two points at two consecutive planes separated by a distance *"d"* to show that the total reflection from the two planes is in phase. Since reflections from all points in one plane are in phase and the reflection from any point on another plane is also in phase with respect to the first one. The condition for reinforcement is given by:

$$BA^{'} + A'C = n\lambda \tag{2.23}$$

$$BA^{'} + A'C = 2d\sin\theta \tag{2.24}$$

$$n\lambda = 2d\sin\theta, \tag{2.25}$$

where n is an integer. A powder consists of a large number of randomly oriented micro-crystallites. When it is exposed to monochromatic X-rays of wavelength λ, all crystallites in a favorable orientation diffract the radiation according to the Bragg equation. Diffraction occurs if the angle between the direction of the incident X-ray beam and the normal vector of the plane is equal to 90°-θ. All the diffracted rays from a set of planes of spacing *"d_1"* will generate a cone of a semi-apex angle $2\theta_1$, planes of spacing *"d_2"* will generate a cone of an angle $2\theta_2$ and so on (see Figure 2.15 (a)). If a photographic film is placed perpendicular to the undeviated beam "XF" at the point "F", a pattern of concentric rings will be produced by those cones of diffracted rays which intersect the films [21]. The diffraction pattern (Debye Scherrer rings) for an ideal powder, where all the crystallites are of regular shape and all orientations are present is shown in Figure 2.15 (b). These orientations are equally frequent and the diffracted intensity on a Debye-Scherrer cone is independent of the azimuth, which means that complete information about the diffraction can be obtained by measuring along a radial intersection through the Debye-Scherrer cones. The Debye Scherrer rings of a non ideal powder are shown in Figure 2.15 (c).

If the total number of orientations of the crystallites irradiated by the X-ray beam is too small, the diffraction rings will be discontinuous and spotty rather than continuous and uniform in intensity. It can be improved by increasing the number of crystallites

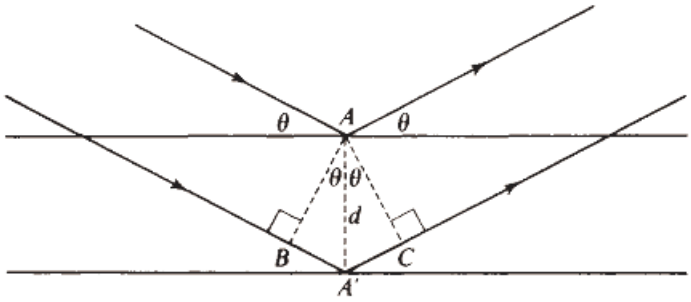

Figure 2.14: *Schematic drawing of Bragg´s law.*

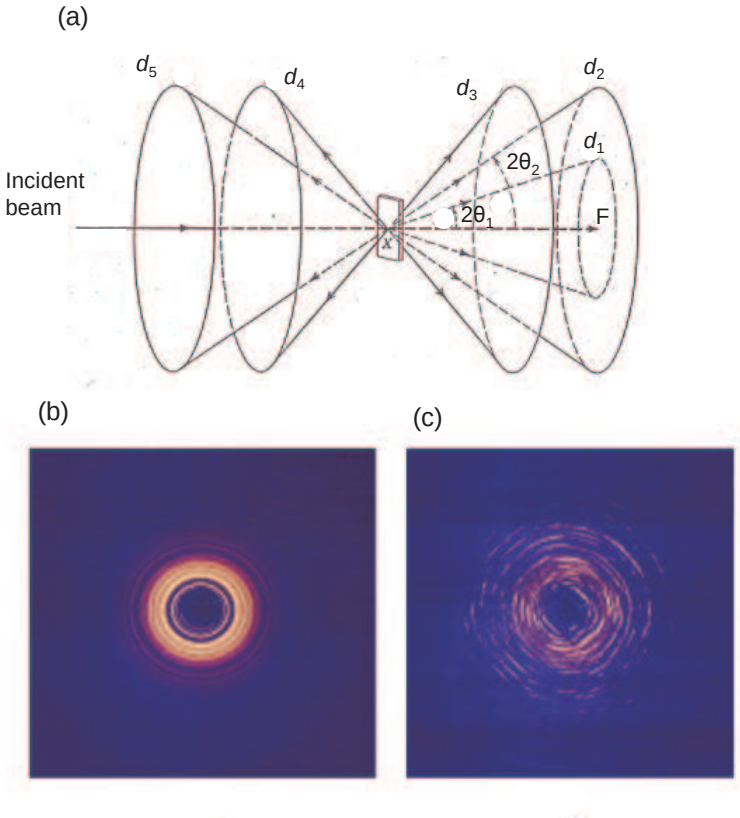

Figure 2.15: *(a) Diffraction of X-rays from a powder sample (the figure is adopted from [21]), (b,c) Debye-Scherrer rings from an ideal powder and from a non ideal powder, respectively.*

irradiated by the beam or by moving the sample in such way to take a variety of orientations for each crystallite with respect to the X-ray beam.

2.2.1 Experimental setup for high pressure X-ray powder diffraction

The room temperature high pressure X-ray powder diffraction measurement of $\beta-Na_{0.33}V_2O_5$ was carried out at beam-line ID09A with monochromatic radiation (λ=0.41142 Å) in ESRF at Grenoble. The membrane-type diamond anvil cell was used for pressure generation and it can be effectively used up to 40 GPa. The DAC supports only a very small sample, it needs a brilliant beam for the measurement. The schematic drawing of an experiment is given Figure 2.16.

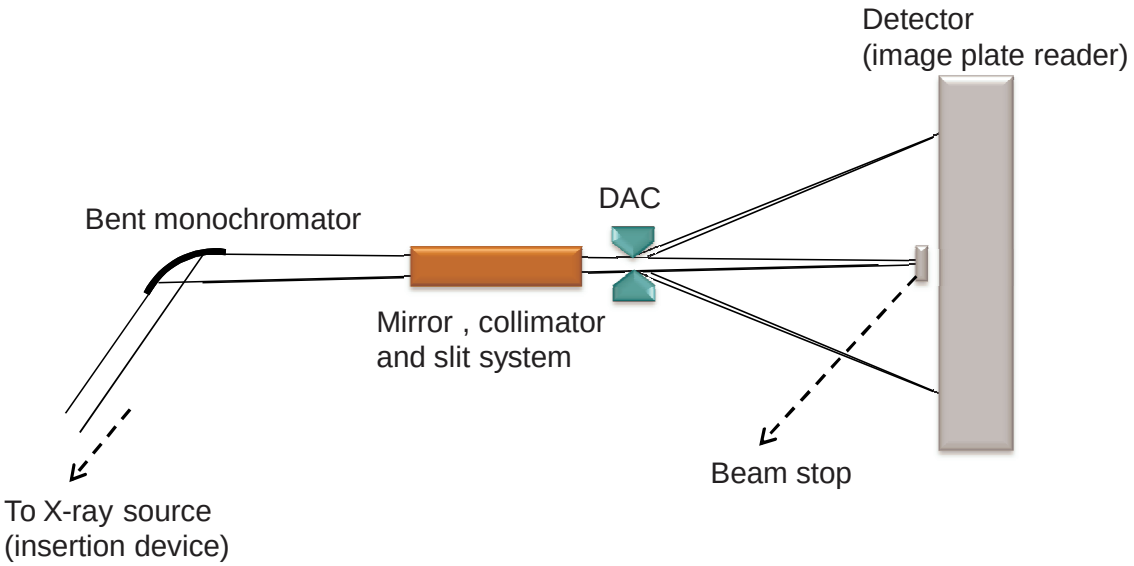

Figure 2.16: *Schematic drawing of the setup at beamline ID09A of ESRF.*

The beam from an in-vacuum insertion-device is vertically focused by a spherical mirror and horizontally by a bent Silicon (111) monochromator as shown in Figure 2.16. The typical working energy for high pressure experiments is 30 keV with a flux of 10^{11} photons/s at 200 mA. The beam size on the sample is normally about 30x30 μm^2. The DAC is mounted directly onto the diffractometer for room temperature measurements. The scattered radiation is collected by an image-plate detector MAR345. The DAC was rotated by $\pm 3°$ during the exposure to improve the powder averaging.

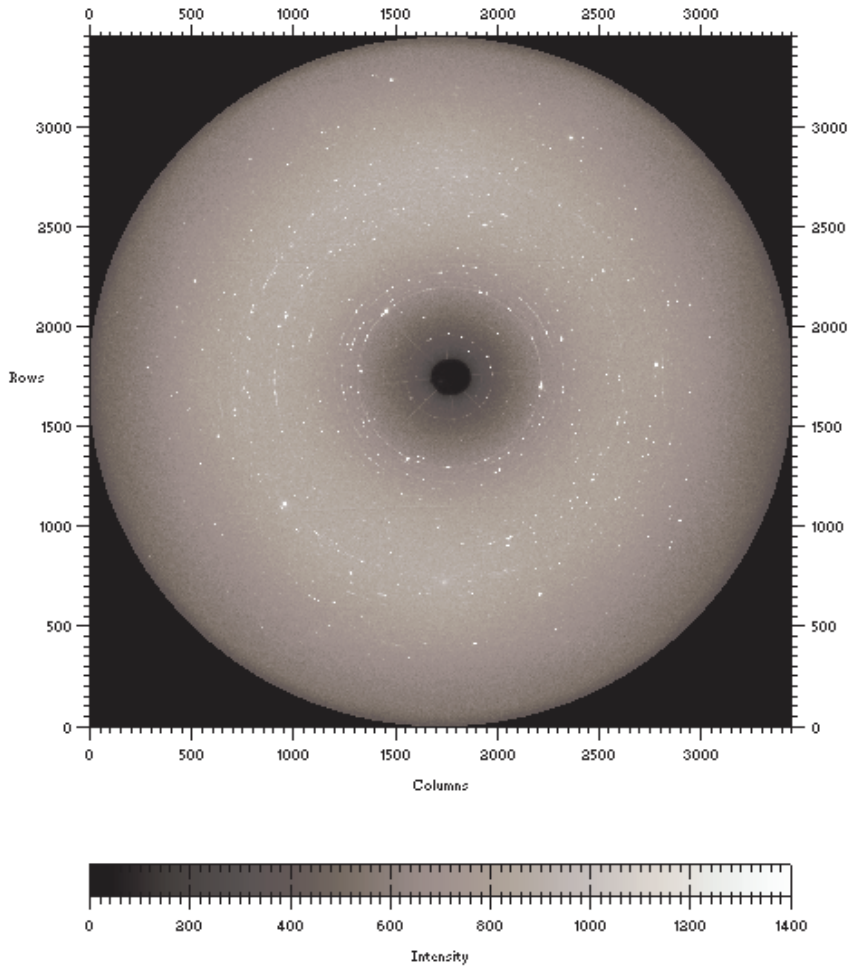

Figure 2.17: *X-ray powder diffraction data of* $\beta-Na_{0.33}V_2O_5$ *at 1.0 GPa, recorded on a MAR345 imaging plate detector.*

2.2.2 Data acquisition and processing

The single crystal of $\beta - Na_{0.33}V_2O_5$ grown by a flux method [22] was grounded into fine powder. The gasket with a hole drilled in the center of it was kept on the fixed part of the diamond anvil cell, the finely ground powder of $\beta-Na_{0.33}V_2O_5$ was put in the hole of the gasket along with a ruby crystal for the pressure determination. The pressure was determined by the ruby fluorescence method using a laser spectrometer (already described in Section 2.1.3). Pressurized helium (He) was used as a pressure transmitting medium to assure good hydrostatic conditions up to the highest investigated pressure of 20 GPa. Finally, the DAC was fixed in the diffractometer for an experiment. The position of the DAC relative to the X-ray beam was aligned, so that the beam passed through the hole in the gasket without hitting the gasket or the cell

body. In addition, an appropriate sample-to-detector distance was set, so that a sufficient number of Debye-Scherrer rings were present on the recorded image, and that the Bragg reflections were well resolved at low diffraction angles. The first step for collecting data is to set a desired value of pressure. When the DAC was approximately at the desired value of pressure, a certain time (5-10 minutes) is required to stabilize the pressure within the DAC. After an image was recorded, the image plate detector was read out and the image plate was erased so that no traces of the previously recorded image remained, which would have appeared as artifacts in the subsequently recorded image. The typical two dimensional image is shown in Figure 2.17.

The recorded image plate data were converted to tables of intensity versus scattering angle 2θ and corrected for errors due to parasitic diffraction employing the computer program named FIT2D. The diffraction radiation can geometrically be seen as the intersection of Debye-Scherrer rings. The radii of the rings contain information about the diffraction angle. The artifacts due to the diffraction on the ruby ball, diamond anvils, polycrystalline impurity phases with strong texture and the radiation scattered from the beam spot can be clearly viewed by zooming the image in the FIT2D program, because these are isolated spots which can be clearly distinguished from the diffraction originating from the sample. Some examples of these artifacts are shown in Figure 2.18, which must be excluded from the 2D image before integration. The integration is performed over the azimuthal angle.

In the FIT2D program, masking the spots which belong to artifacts is the convenient way to exclude them from the diffraction pattern of the samples. After masking, integration was performed, the integrated spectrum is shown in Figure 2.19. The particle statistics in high pressure XRD are considerable worse than the particle statistics of other types of X-ray powder diffraction experiments because of the small sample volumes in the DAC. The intensities of the Bragg reflections obtained in high pressure powder diffraction experiments are therefore less accurate. Short wavelengths are necessary to increase the number of Bragg reflections / Debye-Scherrer rings in the detection area of the detector. Nevertheless, the quality of high pressure powder diffraction data is often not sufficient for structure solution, but for already known structures the pressure dependence of the unit cell parameters can be obtained from the data.

In Figure 2.19, a high background is observed. One of the main contribution to this high background is the scattering of radiation by the pressure medium. The background was subtracted from all measured spectra at different pressures. The background subtracted spectra are presented in Chapter 4. The integrated powder diffraction data were saved, later this data were used by the crystallographic program

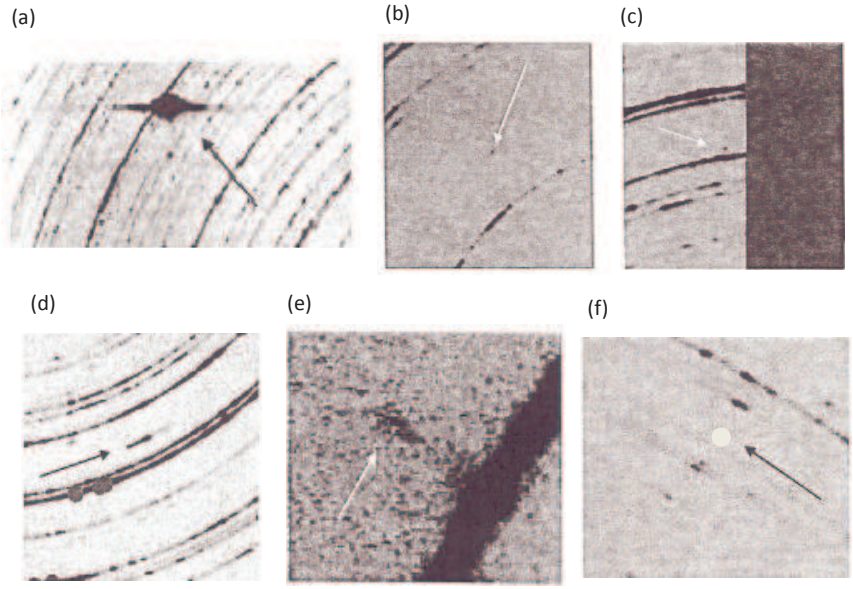

Figure 2.18: *The artifacts from the parasitic diffractions are marked with arrows, (a) the diamond single crystal reflections, (b-c) the diffraction spots originating from a single crystalline impurity phase, most probably from the rubies, (d) the diffraction of a polycrystalline impurity phase with a strong texture, (e) the diffuse streak near to the innermost powder ring is probably due to radiation scattered at the beam spot, and (f) either a defect on the imaging plate or dust on the backside of the DAC. The figure is adopted from [23].*

JANA2000, which is used for structural analysis.

2.2.3 LeBail fit

In a powder pattern where the peaks are overlapped, the extraction of individual intensities is complicated. The overlap can be imposed by symmetry or accidentally arise from near-equivalence of d-values for non equivalent reflections. The individual intensities were extracted from the powder pattern by a profile fitting procedure. The method used for profile fitting was proposed by LeBail [24]. The LeBail method is a modified form of the Rietveld whole profile method [25]. In Rietveld method the reflection intensities are computed from a structural model, while in the LeBail profile fitting method, the intensities of the reflections are adjusted in order to provide the best matching of the calculated and the experimentally observed diffraction patterns,

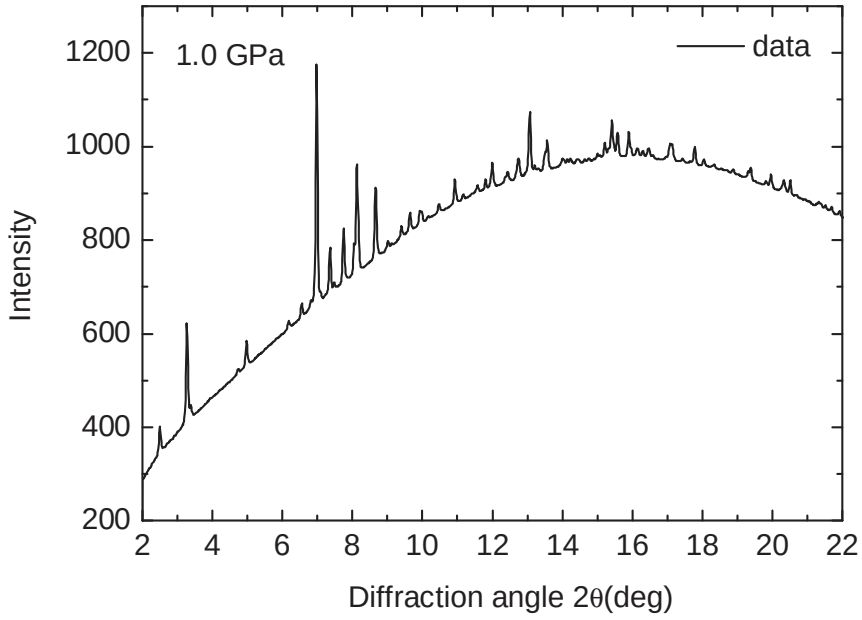

Figure 2.19: *The scattered intensity as a function of the scattering angle 2θ obtained from the image plate recording at 1.0 GPa.*

instead of structural parameters. In the LeBail method the intensities evolve iteratively, other parameters including background function, unit cell, and peak profile parameters can be refined simultaneously with the LeBail intensity extraction. The intensities thus obtained are proportional to the corresponding values of structure factor $|F|^2$. The LeBail method was chosen instead of the standard Rietveld method in order to overcome the effects due to powder quality, i.e. the LeBail method allows reliable simulation of peak intensities even if few pieces of the powder are not large enough to contain all possible crystalline orientations or it is partially oriented. The LeBail fits of the diffraction data were carried out by using the JANA2000 software.

To fit the experimental data the refinement was done without a structural model. The best fit of the calculated pattern to the observed pattern is judged by means of numerical criteria, called profile R factor (R_p) value and weighted profile R-factor (R_wp) value, which are defined as [26]:

$$R_\mathrm{p} = \frac{\sum_j |I_{\mathrm{obs},j} - I_{\mathrm{calc},j}|}{\sum_j I_{\mathrm{obs},j}} \qquad \textit{and} \tag{2.26}$$

$$R_\mathrm{wp} = \frac{\sum_j \mathrm{w}_j (I_{\mathrm{obs},j} - I_{\mathrm{calc},j})^2}{\sum_j \mathrm{w}_j (I_{\mathrm{obs},j})^2}. \tag{2.27}$$

R_wp has contribution of background statistics and the shape differences (width) between calculated and the observed profile. The w_j is the weighting factor for the

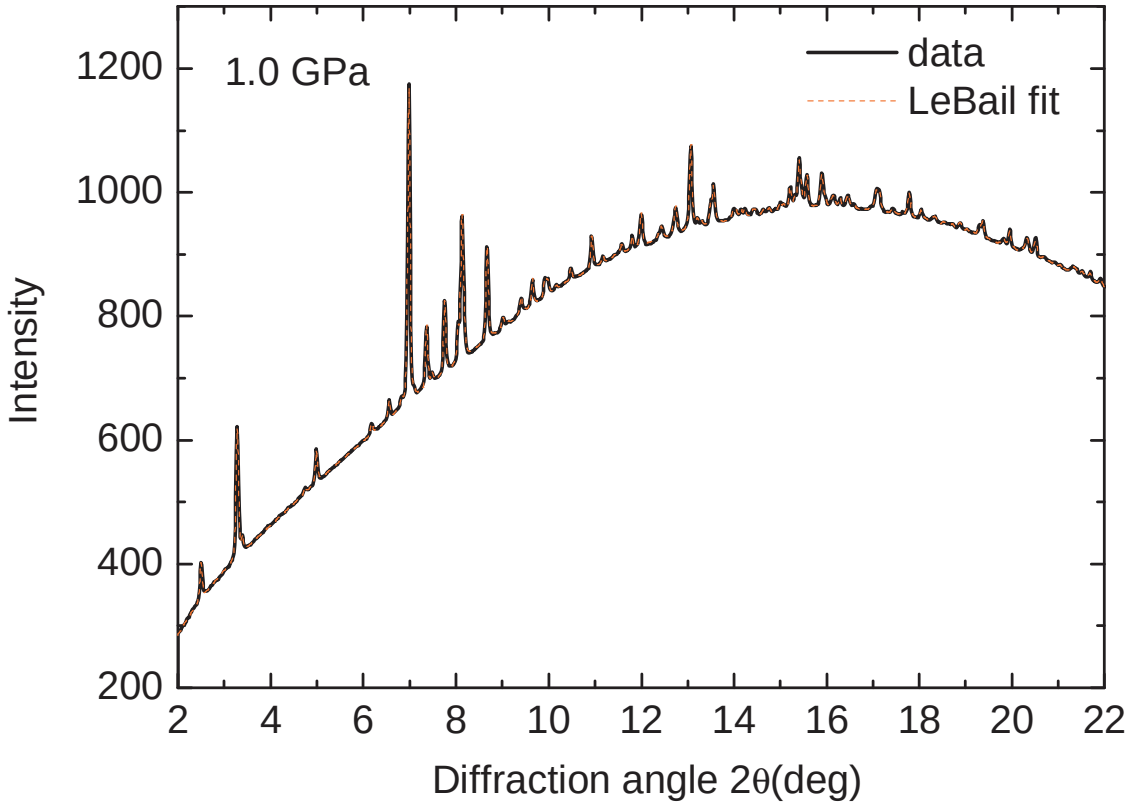

Figure 2.20: *The scattered intensity as a function of scattering angle 2θ obtained from the image plate recording at 1.0 GPa along with the LeBail fit.*

jth point and is defined as $w_j = 1/I_{\mathrm{obs},j}^{'}$ (when the background is included). The diffraction patterns of all pressures were well fitted with R_{p} and R_{wp} values less than 0.2 % and 0.3 %, respectively.

By accurately measuring peak positions over a long range of 2θ, the unit cell parameters were determined. The pressure-dependent lattice parameters were extracted from the LeBail fit of the integrated data. The difference between $I_{\mathrm{obs},j}$ and $I_{\mathrm{calc},j}$ is presented in chapter 4.

3 High-Pressure low-temperature (HPLT) Vis-UV microspectrometer

3.1 Motivation

The room temperature high pressure reflectivity and transmission measurements presented in this thesis were carried out using a commercial Bruker Spectrometer IFS66v/S, coupled with an infrared microscope (IRscope II). In this spectrometer we are limited to the highest frequency of 25000 cm^{-1}(3eV).

In many transition metal compounds the electronic excitations occur in visible (Vis) and ultraviolet (UV) energy range, such as the electronic excitations i.e., crystal-field *d*-*d*-excitations and charge transfer excitations of the investigated chromium spinel compounds in this thesis. Since pressure affects the electronic states to a large extent, one can get a lot of information about electronic system if the range above 3 eV would be accessible for high-pressure technique. Due to the energy limit of the IR spectroscopy, the all spin-allowed *d*-*d*-transitions of chromium compounds were not accessible in the experimental data presented in this thesis. In order to get access to the Vis-UV energy range for the high-pressure microspectroscopy, a part of this PhD project was devoted to the extension of pressure-dependent measurements to the Vis-UV energy range. Thus, the Vis-UV microspectrometer was designed and constructed for reflectance and transmission measurements under pressure and at low temperatures. There are other prototypes of Vis-UV microspectrometer for low temperature high pressure measurement,e.g. microptical double beam system [27], one channel set up [28]. The Vis-UV microspectrometer presented in this thesis is based on a novel optical scheme.

3.2 Vis-UV microspectrometer

The Vis-UV microspectrometer consists of three main parts: the light source (a 150 W Xe-arc lamp, covering a spectral range of 200-900 nm (≈1.3-6 eV)), the home-built microscope, and the spectrogrograph with CCD (charge-coupled devices) detector. The simple application of the microscope is to magnify the image of the object. In order to preclude influence of water vapour in the atmosphere, the microscope is usually purged with dry nitrogen, but there is also a possibility to use it under vacuum conditions. The elements inside the microscope are the Schwarzschild objective/condenser, plane mirrors, spherical mirrors, field stops, and a filter (see Figure 3.1 and 3.2). The diameter of field stop can vary between 0.5 mm and 3.75 mm.

The Schwarzschild objective forms a real, enlarged image of the object, which is viewed through the eyepiece. The filter is placed in the optical path of viewing mode, which blocks the UV and passes the visible light to view the sample. In viewing mode, after the field stop (2) there is moveable plane mirror (PM2) which is used to switch the system either to measurement mode or to the viewing mode depending on the position of PM 2. In viewing mode PM 2 directs the beam towards a lens which focuses the light at the plane mirror mounted at 90 ° angle bracket, which reflects the light on to the eyepiece in Z-direction. The translational and rotational stages, which are used to move the mirrors and to rotate the aperture wheels (field stops) and polarizer (if needed for measurement) are controlled by a program made by using a Labview software. There is a simple connection between the spectrograph and the users PC (USB interface). The basic arrangement of the microscope imaging system shown schematically in Figure 3.1 and 3.2 for transmission and reflection measurements, respectively.

3.2.1 Schematic drawing for transmission measurement

The optical layout in transmission mode is shown in Figure 3.1. The light from the source strikes on the lens which focuses the light towards movable plane mirror (PM 1) after passing through the selected aperture at field stop (1). The movable mirror switches the light path between reflection and transmission mode. The light reflected by movable PM 1 is sent to a spherical mirror by another plane mirror. Next to the spherical mirror the optical path is followed by two plane mirrors and finally the light is directed to the Schwarzschild condenser. The Schwarzschild condenser focuses the light to the sample, the transmitted light is then collected by the Schwarzschild objective and produces an image of the sample at the field stop. After the field stop there is a movable plane mirror (PM 2) which switches the beam path between viewing mode

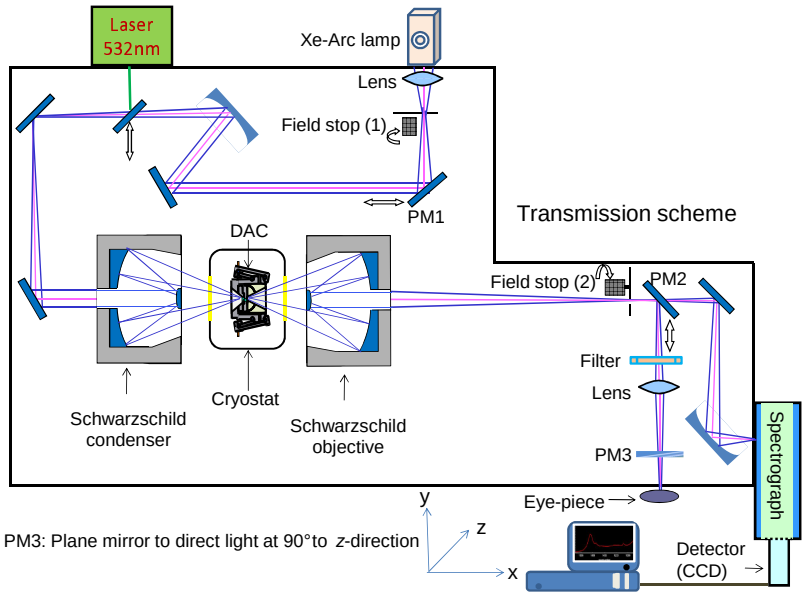

Figure 3.1: *Optical layout of Vis-UV microspectrometer illustrating the transmission mode. The double side arrows close to the mirrors indicate that the respective mirrors are at movable translational stages.*

and measurement mode. In viewing mode the alignment of the sample is controlled through the eyepiece. For measurement mode, the beam from the selected field stop (2) is deflected by the plane mirror towards the spherical mirror which focuses the beam at the entrance slit of the grating spectrograph and finally detected by CCD.

3.2.2 Schematic drawing for reflection measurement

In reflection mode, less optical components are used compared to transmission mode (see Figure 3.2). Light from the source strike on the lens, which focuses the light on field stop (1) where appropriate aperture is selected. After passing through aperture the light strikes on the half mirror, which deflects the incoming beam towards the Schwarzschild objective. The Schwarzschild objective focuses the light to the sample and then collects the reflect back light and produces an image of the sample at the field stop (2) and finally reflected light enters to the spectrograph or to the eyepiece depending on the selected mode. In reflection measurement only half of the cross section of the incoming beam is used. In Figure 3.2, the microspectrometer is in reflection mode, the dotted lines show the inactive transmission mode.

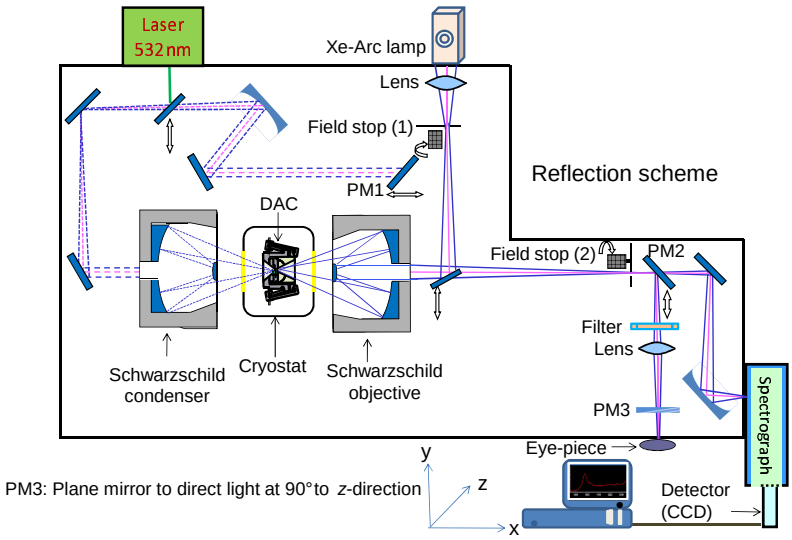

Figure 3.2: *Optical layout of Vis-UV microspectrometer illustrating the reflection measurement mode. The dotted lines show the light path for transmission mode. The double side arrows close to the mirrors indicate that the respective mirrors are at movable translational stages.*

Schwarzschild objective

The Schwarzschild objective is based on the combination of two concentric spherical mirrors, small convex mirror and a larger concave mirror facing each other as shown in Figure 3.3. The design is simple and elegant and useful for optical systems with small field of view and high resolution. The concave mirror has an aperture in the center thus permitting the light to reach the convex mirror, and reflected light from convex mirror is focused through concave mirror behind the convex mirror at point F (see Figure 3.3). The main advantages of a Schwarzschild microscope objective are that [5, 29]:

(i) It can be applied in a wide spectral range.

(ii) Chromatic errors are absent.

(iii) Some of the third-order Seidel aberrations cancel for certain object-image positions.

The radii of curvature of convex and concave spherical mirrors defines the magnification (M)of Schwarzschild objective, i.e.,

$$\mathrm{M} = \frac{g - 1 \pm \sqrt{g}}{g - 1 \mp \sqrt{g}}, \tag{3.1}$$

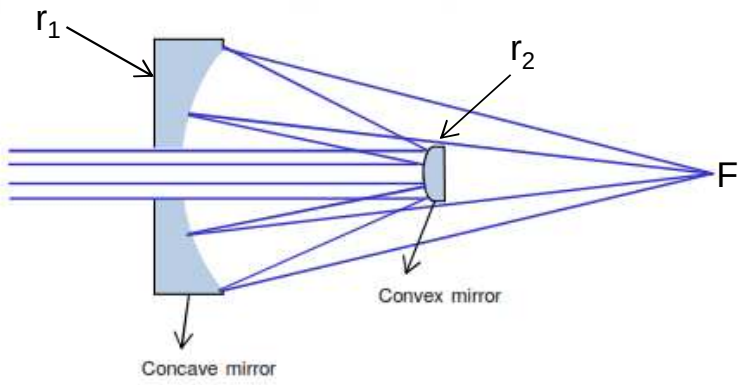

Figure 3.3: *Optical layout of the Schwarzschild objective. F is the focal point of the objective, and r_1, r_2 are the radii of curvature of convex and concave mirror, respectively.*

where $g = r_1/r_2$. The objectives are mounted on *xyz*-translation stages which allow the precise alignment of the focal position. The Schwarzschild objectives used in our experiment focus the radiations on a very small sample of approximate size $100\mu\text{m}\times100\mu\text{m}\times50\mu\text{m}$. When the sample is placed in DAC inside the cryostat the long working distance is needed. The commercially available Schwarzschild objectives offers a working distance, which is not long enough for measurement inside cryostat. For this purpose the home-made Schwarzschild objectives [30] with a large working distance were used.

Shamrock spectrograph SR-303i

The Andor Shamrock spectrograph SR-303i, with pre-aligned detector (CCD camera) was used, which is shown in Figure 3.4 (a), and its inside view (optical layout)is shown in Figure 3.4 (b). It has a triple grating turret, where three gratings with different groove density and blaze wavelength are mounted. This provides the flexibility to choose different resolutions for specific measurements. The graphical software user interface is simple and allows the user to fully control the spectrograph´s functionality including wavelength control and calibration, grating selection, and slit control etc.

The reflected or transmitted light from the sample enters the spectograph by spherical mirror (the last component of microscope), which focuses the light onto the slit of spectrograph. This incoming light enters the slit of spectrograph and strikes at the plane mirror (see Figure 3.4 (b)), where it is reflected towards the toroidal mir-

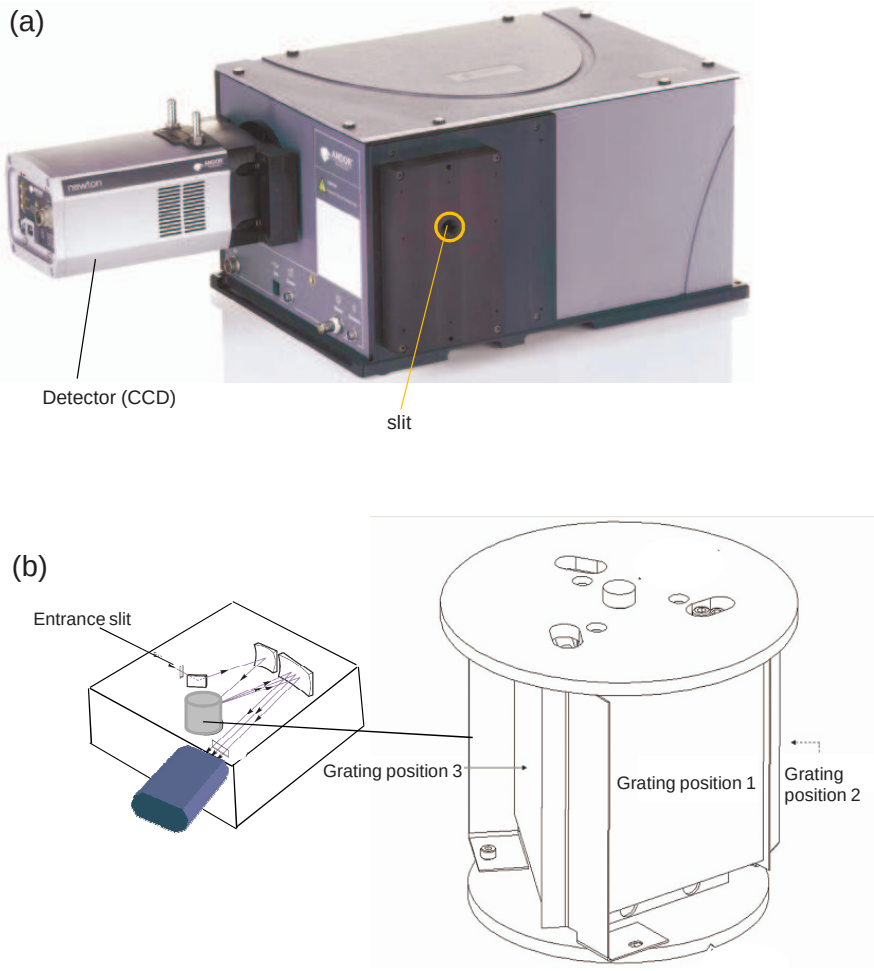

Figure 3.4: *(a) The picture of Andor Shamrock spectrograph SR-303i, adopted from Ref [31]. (b) Optical path inside the spectrograph.*

ror which sends the light to the grating. The grating produces an optical spectrum by diffraction of reflected light. This diffracted light, send to the detector (CCD) by another toroidal mirror is measured.

3.3 Test measurements

Several test measurements were carried out on different samples but the collected spectra were not like as it was expected. Since the setup is to investigate the materials under pressure in a broad spectral range. In the current design, one has to replace the antirefletion coated lenses for specific small wavelength range, which is not feasible way

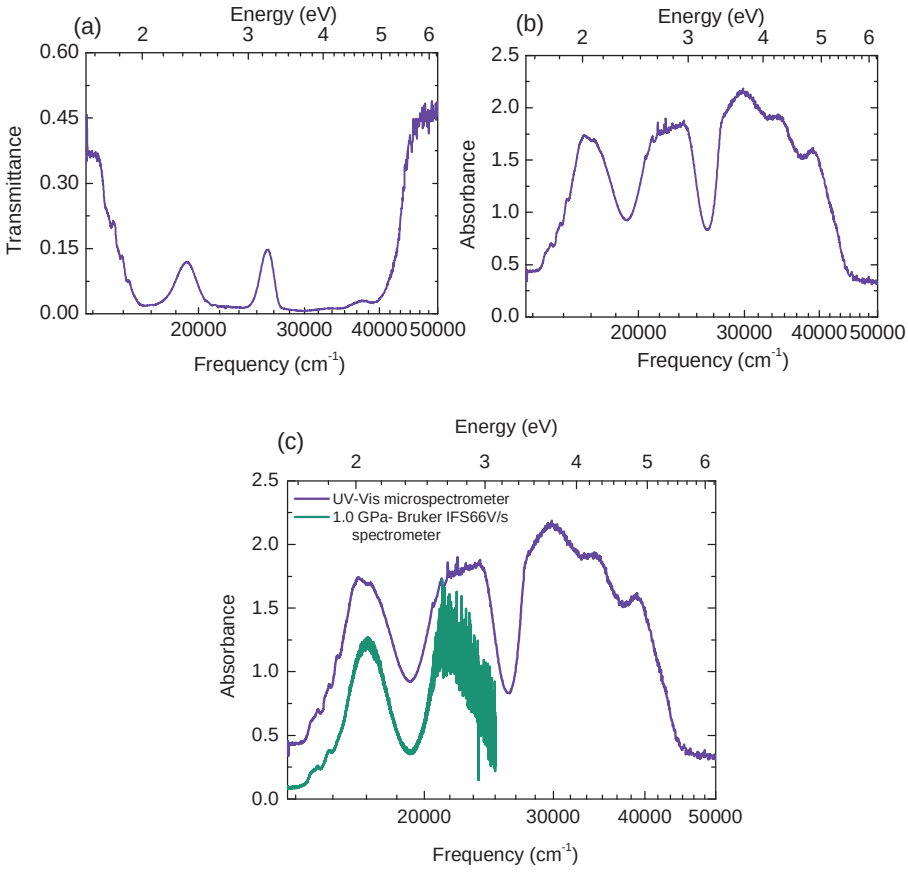

Figure 3.5: *(a) Transmission spectrum of $CdCr_2O_4$ and (b) absorption spectrum. The data is collected from the updated version of Figure 3.1 where focusing lens in front of light source is replaced by two spherical mirrors(see Ref [32,33]). (c) Comparison of absorption spectrum measured in Vis-UV microspectrometer with the spectrum measured at room temperature in Bruker FTIR spectrometer at 1.0 GPa.*

especially for pressure measurements. To find the proper solution of this problem and to figure out why test measurements are not in agreement with expected ones, even with a very good alignment of the system. For this purpose the ray tracing (ZEMAX program) was done as a master project of Kathrin Martin [32] and further as a PhD project of Armin Huber. Through ray tracing we came to know that condenser in the source assembly is also creating a problem for broad spectral range. The condenser from the source assembly was removed and focusing lens was replaced by two spherical mirrors. The new designs for transmission and reflection measurements without lens are shown in Ref [32, 33]. The test measurement carried out on single crystal of

$CdCr_2O_4$ in transmission mode at ambient conditions by new design is presented in Figure 3.5. The size of the sample was 0.8×0.5 mm. The aperture used to collect data was 0.5 mm and the data acquisition time was 1 second. Th grating used for this measurement has 600 grooves/mm. The measurement was done in three steps by choosing different central wavelength. The three obtained transmission spectra are merged (see Figure 3.5 (a)). The calculated absorbance spectrum is shown in Figure 3.5 (b). To check the reliability of this test measurement, the absorbance spectrum is compared with the absorbance spectrum measured at room temperature in Bruker FTIR spectrometer at 1.0 GPa, both spectra are consistence within the overlap frequency range as shown in Figure 3.5 (c). The interpretation of measured spectrum is given in Chapter 6.

4 High pressure X-ray diffraction study of $\beta-Na_{0.33}V_2O_5$

4.1 Crystal structure of $\beta-Na_{0.33}V_2O_5$

$\beta-Na_{0.33}V_2O_5$ crystalizes in a monoclinic tunnel-like structure with space group C2/m. The unit cell of $\beta-Na_{0.33}V_2O_5$ is shown in Figure 4.1. It consists of three structural units with three inequivalent V sites. The V_1 is coordinated with six oxygen atoms and forms an octahedron $(V_1)O_6$. These octahedra build a zigzag double chain structure along the b-axis by sharing their edges. The V_2 is also coordinated with six oxygen atoms and forms octahedron $(V_2)O_6$. These octahedra form a two-leg ladder by corner sharing. The third structural unit is $(V_3)O_5$ polyhedron, these polyhedra form a zigzag double chain along the b-axis. There are two possible sodium sites located in the tunnels, represented as a two-leg ladder along the b-axis. For a sodium stoichiometry x=0.33 every rung of the ladder contains one Na^+ ion. When x is below 0.33, the vacancy is created and some rung of the ladders will not contain Na^+ ion. When x is above 0.33, another possible site in the rung will be occupied with a Na^+ ion. The deviation from x=0.33 disorders the uniformity of the Na^+ chain and leads to different physical properties [22].

4.2 Physical properties of $\beta-Na_{0.33}V_2O_5$

The $\beta-Na_{0.33}V_2O_5$ belongs to low-dimensional β-vanadium bronzes ($\beta-A_{0.33}V_2O_5$) family, where A^{1+} (A = Li, Na, and Ag) is a monovalent ion. The β-vanadium bronzes are typical examples of highly correlated electron systems. They have attracted great interest because of their remarkable physical properties, such as temperature-induced metal-insulator transition, charge ordering, and pressure-induced superconductivity [36].

To understand the physical properties of this material, it is interesting to look at the pressure-temperature (P-T) phase diagram (see Figure 4.2) [36]. The $\beta-Na_{0.33}V_2O_5$ shows charge ordering (CO) at 135 K. As the pressure increases, the T_{CO} shifts to lower

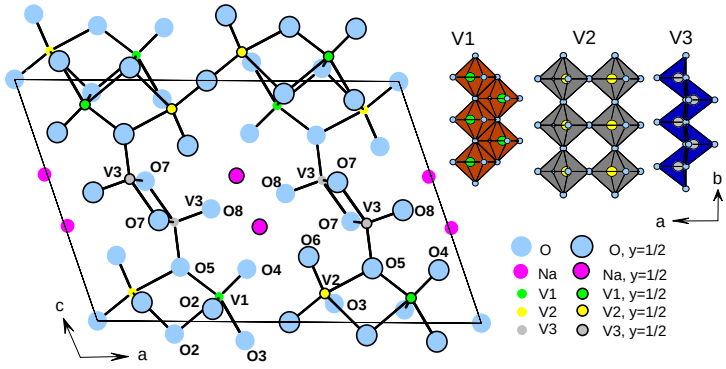

Figure 4.1: *Crystal structure of $\beta-Na_{0.33}V_2O_5$ projected in the (010) plane. The vanadium oxide two-leg ladder as well as the two kinds of vanadium oxide chains are also shown. The figure is adopted from Ref [34, 35].*

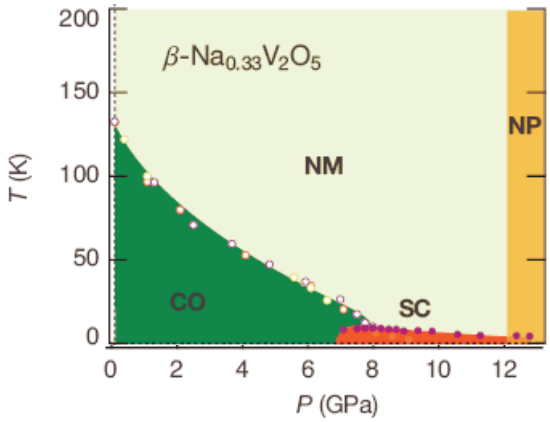

Figure 4.2: *The pressure-temperature (P-T) electronic phase diagram of $\beta-Na_{0.33}V_2O_5$ [36]. Notations CO, SC, NM and NP represent charge ordering, superconducting, normal metallic and the newly observed higher pressure phases, respectively.*

temperature. At 6.8 GPa the superconducting phase appears below 9 K, but charge ordering and superconducting (SC) phases coexist up to 7.3 GPa (see Figure 4.2). By further increasing the pressure the charge ordering phase disappeared and T_{SC} shifts to a lower temperature and at 12 GPa the superconducting phase vanishes and it leads to some non superconducting new phase (NP). The superconducting state competes with charge ordering and NP metallic states. Since the superconducting phase is adjacent to a charge ordered phase, an important role of charge fluctuations for the superconductivity is suggested [36].

The $\beta-Na_{0.33}V_2O_5$ is one of the best conductor among vanadium bronzes. At room temperature it shows a one dimensional metallic character along the b-axis, exhibiting lowest resistivity in this direction [22]. The recent polarization dependent of optical study of $\beta-Na_{0.33}V_2O_5$ on single crystal under pressure give an idea about structural changes happening at around 12 GPa [34,37]. In reflectivity measurements, for E $\parallel$ b, the overall reflectivity increases with the application of pressure up to 12 GPa and opposite trend is observed above $P_c \approx$ 12 GPa. The mid infrared band which is claimed to be of small-polaronic origin, shows red shift and its oscillator strength increases upon pressure application up to 12 GPa. The red shift shows the decrease of polaron binding energy revealing that the electron-phonon coupling tends to decrease with pressure. Above $P_c \approx$ 12 GPa, the opposite behavior of mid-infrared band is observed. For E $\perp$ b , the three phonon modes at around 1000 cm^{-1} harden with pressure in nearly linear way, without any abrupt changes. This frequency shift with pressure signifies that, there is no major change in the local V-O coordination up to 20 GPa. On low frequency side the new broad excitation with a shoulder on its high frequency side appears above 12 GPa. This feature is interpreted as redistribution of charge among different V-sites. These features also show hardening with increasing pressure. In infrared data there are no major changes which indicate structural changes in the system except anomalous changes at around 12 GPa. Indeed the structural phase transitions are unlikely at around 12 GPa [37].

In Raman data [34], the anomalous changes in pressure range 9-12 GPa, are interpreted in terms of charge transfer between different V-sites. For E $\parallel$ b, the phonon belonging to V_2-O_1-V_2 bending mode is hardly affected upon pressure application. This reveals that charge transfer occurs mainly among V_1 and V_3 sites [34], which indicate low compressibility along chain direction. In the optical data [34,37] most of the spectral features are present up to the highest applied pressure. The anomalous changes in the optical data at around 12 GPa reveal the change in electronic properties of the system. To understand the effect of pressure on electronic structure, knowledge about the variation of the crystal lattice was enviable. The pressure dependent X-

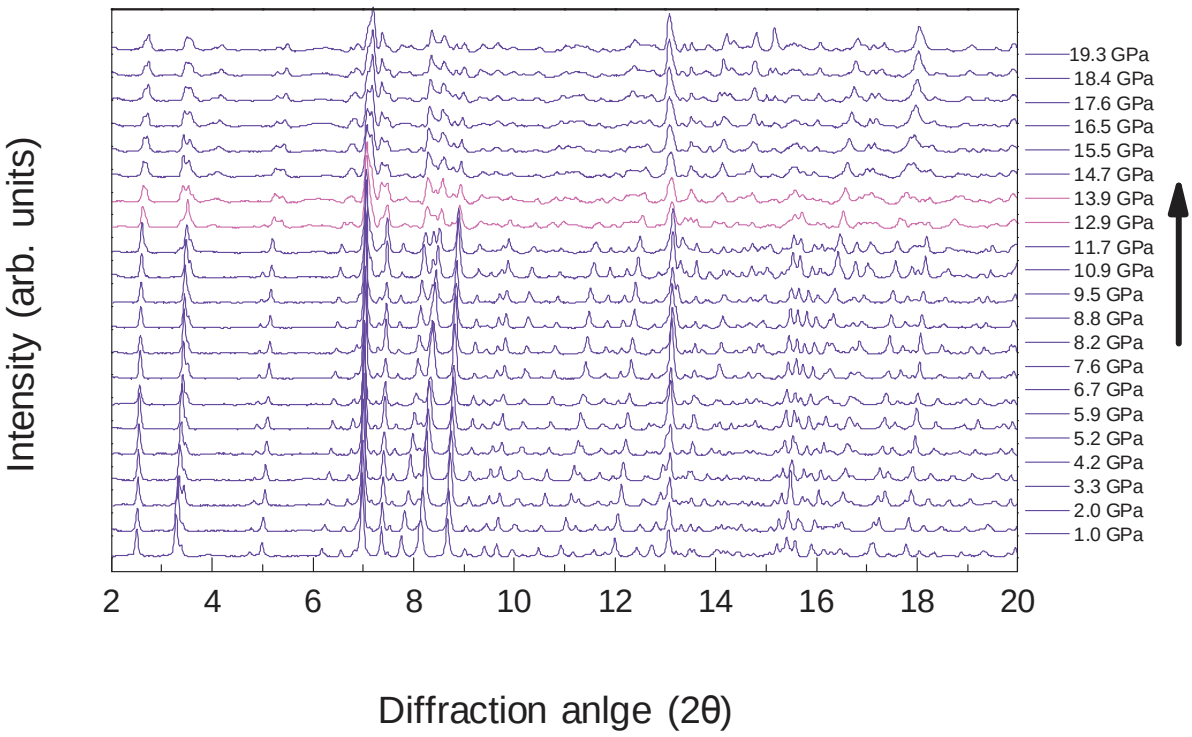

Figure 4.3: *Room-temperature powder XRD diagrams of* $\beta-Na_{0.33}V_2O_5$ *at different pressures. The arrow indicates the pressure values in ascending order. The diffraction patterns with purple colour indicate the pressure region (12-14 GPa) where the anomaly starts.*

ray powder diffraction measurements were carried out to get the information about pressure effect on the crystal lattice of $\beta-Na_{0.33}V_2O_5$.

4.3 Effects of external pressure on crystal structure of $\beta-Na_{0.33}V_2O_5$

The pressure-dependent structural properties of single crystal $\beta-Na_{0.33}V_2O_5$ were studied at room temperature by high resolution angle-dispersive powder X-ray diffraction (XRD). The measurements and analysis procedures are already described in section 2.2 of Chapter 2. The resultant integrated data for various measured pressures is presented in Figure 4.3. There is anomalous changes in the diffraction pattern at around 12-15 GPa. In order to get the unit cell parameters as a function of pressure, the diffraction patterns were fitted with the LeBail method by using the crystallographic computing program JANA2000. The diffraction diagrams of $\beta-Na_{0.33}V_2O_5$

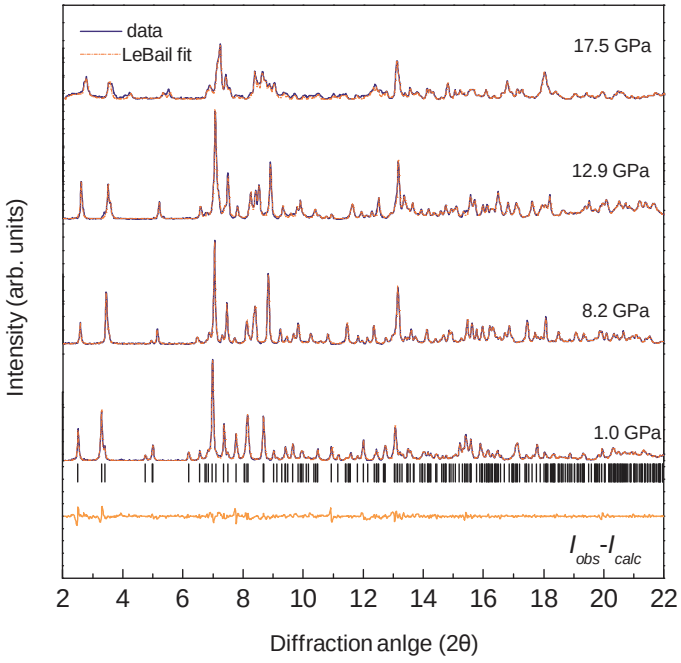

Figure 4.4: *Room-temperature powder XRD diagrams of $\beta - Na_{0.33}V_2O_5$ as a function of pressure together with the LeBail fits. For the lowest applied pressure (1.0 GPa), the difference curve (I_{obs}- I_{calc}) between the diffraction diagram and the LeBail fit is shown. Markers represents the calculated peak positions for the ambient pressure phase.*

for few selected pressures together with the LeBail fits are shown in Figure 4.4. To fit the lowest measured pressure data, the input given to the program for analysis was the crystallographic structure of the system at ambient-condition, which was monoclinic unit cell with space group $C2/m$ containing two formula units, with the parameters a= 15.44 Å, b= 3.61 Å, c= 10.08 Å, and β= 109.6°. The lattice parameters and their normalized values as a function of pressure are shown in Figure 4.5 (a), (b). The unit cell volume as a function of pressure is shown in Figure 4.5 (c). The lattice parameters a, b, and c decrease monotonically with increasing pressure up to $\approx$ 12 GPa, while the monoclinic angle β slightly increases. The diffraction diagrams could be well fitted with the ambient-pressure crystal structure (C2/m) up to the highest applied pressure of 20 GPa. To fit the X-ray data for P>15 GPa, different other crystal symmetries and also other space groups within the monoclinic system were tried out. The quality of the fits was worse for using other space group and symmetries. However, an anomaly is observed in the pressure dependence of all lattice parameters in the range 12-15 GPa followed by a monotonic decrease in the parameters a, b, and c and an increase in the

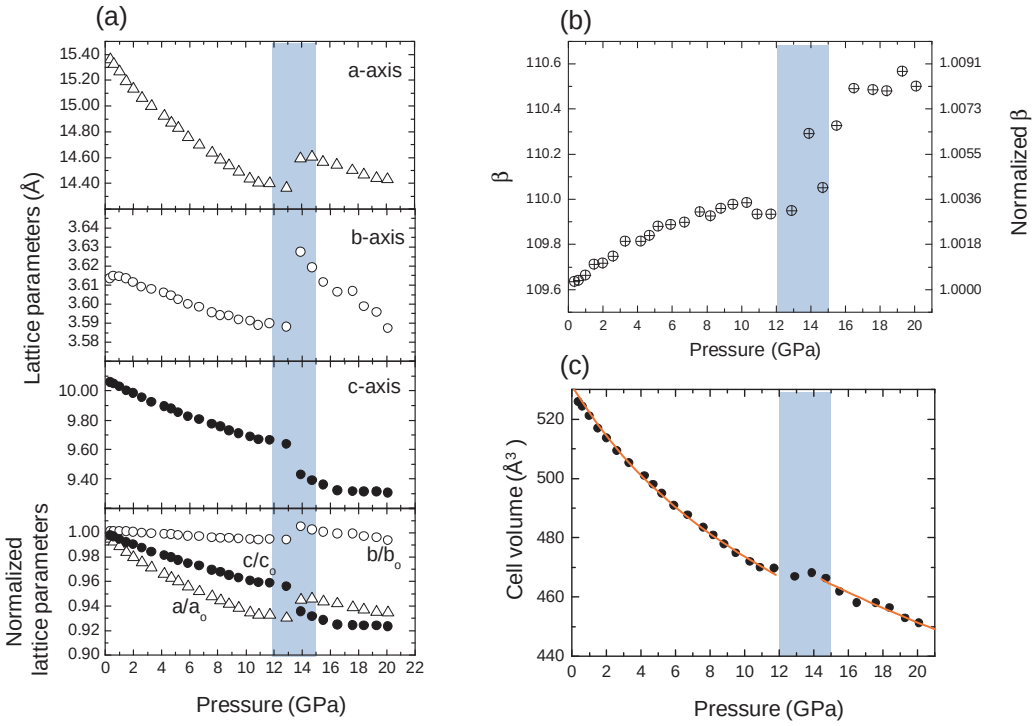

Figure 4.5: *(a-b)Lattice parameters and normalized lattice parameters and (c) unit cell volume of* $\beta - Na_{0.33}V_2O_5$ *as a function of pressure at room-temperature. The gray bars mark the anomalous pressure range. In (c) the red solid lines illustrate the fits according to Equation 4.1 to calculate the* B_0 *and* $B^{'}$ *in two pressure regions i.e., below and above the anomalous pressure range.*

angle β . The pressure dependence of the unit cell volume (V) was obtained from the lattice parameters. The volume was fitted according to the Murnaghan equation [38]:

$$V(p) = V_0[(B^{'}/B_0)p + 1]^{-1/B^{'}}. \tag{4.1}$$

Where $B_0 = -dp/dlnV$ is the bulk modulus and $B^{'}$ is its derivative at zero pressure. The *V(P)* together with the fitting curves in the low- and high-pressure range is shown in Figure 4.5(c). The ambient pressure unit cell volume V_0 was kept fixed at the experimental value of 531.228 Å^3. For P<P$_c$, the bulk modulus B_0 evaluated according to the Murnaghan equation is (53.8±1.5 GPa) and its derivative $B^{'}$ is 7.8 ± 0.5 GPa. In this case the pressure derivative $B^{'}$ is significantly larger compared to the value B$^{'}$≈4 typically found for three-dimensional solids with isotropic elastic properties. The higher value of B$^{'}$ thus suggests anisotropic compression properties of $\beta - Na_{0.33}V_2O_5$.

For P>15 GPa, the values $B_0 = (72.0 \pm 8.0$ GPa) and B$'$=$(6.1 \pm 1.3$ GPa) show the reduction of an anisotropic compression above P_c.

The results of XRD analysis show the extremely small compressibility along the b-direction, i.e. along the polyhedral chains, because the chains can be viewed as rigid objects (see Figure 4.1). This finding is consistent with earlier reports [39]. The decrease of the lattice parameters a and c is the indication that, the distance between the chain is reduced with the application of pressure. Accordingly, an enhanced interaction between the chains is expected, which endorse the charge transfer between them.

It can be concluded, $\beta - Na_{0.33}V_2O_5$ keeps the ambient pressure crystal structure up to 20 GPa according to the structural data. There are strong changes in the peak intensities and new peaks appeared at small diffraction angles at around P_c. These findings prove that the pressure application induces important structural modifications at P_c. These structural changes affect the electronic properties of the material, which could be observed from optical properties. The observed structural changes are consistent with optical studies, which showed that all spectroscopic signatures are present up to high pressure [34, 37]. The anomalies observed in the optical response at 12 GPa is also in full agreement with the anomalies in the results of XRD analysis. The non continuous decrease in the lattice parameter c at P_c in Figure 4.5(a), reveals the reduction of the distance between the $(V_1)O_6$ and $(V_3)O_5$ polyhedra. Above P_c, the probability of the transfer of charge between the V_1 and V_3 sites is enhanced , which is consistent with the earlier interpretation of the pressure-dependent Raman data [34].

5 High pressure infrared study of $BiFeO_3$

5.1 Multiferroics

Multiferroic are the materials in which at least two of the ferroic features such as ferroelectricity, ferromagnetism, ferrotoroidicity or ferroelasticity coexist in single phase. In a broader definition, it also covers materials with ferro- and antiferro-orders. Rare-earth ferrites, manganese-based perovskite, Cr_2O_3, and $BiFeO_3$ are the examples of multiferroics. In these materials, the ferroelectric and ferro/antiferromagnetic phases are coupled in such a way to produce a cross phenomenon known as the magnetoelectric effect , e.g., in orthorhombic $TbMnO_3$ the ferroelectric polarization can be induced with magnetic field and ferromagnetic ordering can be switched on by an electric field in hexagonal $HoMnO_3$ [40]. Such materials have attracted significant attention because of not only their interesting magneto-electrical properties but also their wide applications in the field of information storage, the emerging field of spintronics, and sensors [41–43].

The origin of ferroelectricity is different in different multiferroics. There is no unique theory about multiferroicity, every material has to be studied separately. However, different multiferroics are classified according to the mechanism that drives the ferroelectricity. The two major classes of multiferroics can be distinguished according to the mechanism that drives the ferroelectricity, as follows [42]:
(1) Multiferroics, where the ferroelectricity is driven by hybridization, covalency or other purely structural effects,e.g. $BiFeO_3$ is prototype material.
(2) Multiferroics, where the ferroelectricity is driven by some other electronic mechanism, e.g. correlation effects, with rare-earth manganites as prototype materials.
In the first category, both the polarization and the magnetic order are primary order parameters of the system. These materials show some coupling between these two primary parameters. In the second case, ferroelectricity always arises as a secondary effect that is coupled to some other form of ordering, such as magnetic- or charge-ordering. The understanding of multiferroics requires a good knowledge of well-known

ferroic properties such as ferroelectricity, ferromagnetism or ferroelasticity which have received extensive research efforts over the last decades.

5.2 The perovskite structure class

Perovskites form a large class of materials, deceptively simple in basic structure but immensely complex in compositional variations, symmetry changes, and physical properties. These materials exhibit many interesting and intriguing properties from both the theoretical and the application point of view. Colossal magnetoresistance, ferroelectricity, superconductivity, charge ordering, spin dependent transport, high thermopower and the interplay of structural, magnetic and transport properties are commonly observed features in this family.

The perovskite material has the chemical formula ABX_3. In perovskite oxide compounds, the mainly focused point is the chemistry of the BO_6 octahedra, since in a majority of the compounds the A-ion is an alkali, alkaline earth or a rare earth element and these species will not contribute to electronic states that govern transport or magnetic properties. The materials that deviate from the ideal ABX_3 chemistry both in terms of cation and anion deficiency can be regarded as perovskite related oxides. One example of A-ion deficient perovskites are the family of bronzes with general chemistry A_xBO_3 where *'A'* is an alkaline, alkali earth or rare earth and *'B'* for example is W, Re or Mo [44]. The multiferroic perovskite materials show structural instabilities, which are derived by various external parameters like temperature, pressure, electric, and magnetic field, etc. The magnetoelectric (ME) multiferroics often exhibit two structural instabilities, mainly due to the displacement of cations which gives ferroelectric (FE) properties and tilt of the BO_6 octahedra which play a key role regarding the magnetic properties [45].

5.3 Crystal structure

Crystal structure of perovskite

The crystal structure of perovskite is described with general chemical formula ABX_3, where *'A'* and *'B'* are two cations of different sizes, and X is an anion that bonds both cations. The A-atoms are larger than the B-atoms. The cubic-symmetry structure has the B-cation in 6-fold coordination, surrounded by an octahedron of anions. The ideal perovskite crystal structure is shown in Figure 5.1. In the ideal cubic unit cell of such a compound, the A-atoms sit at the cube corner positions (0, 0, 0), the B-atoms sit at

body center position (1/2, 1/2, 1/2) and oxygen atoms sit at face centered positions (1/2, 1/2, 0), (1/2, 0, 1/2) and (0, 1/2, 1/2) (see Figure 5.1 (a)). The structure can be described as a system of BO_6 octahedra joined at the corners and the A-ions are at the interstitial positions between the octahedra, as shown in Figure 5.1 (b).

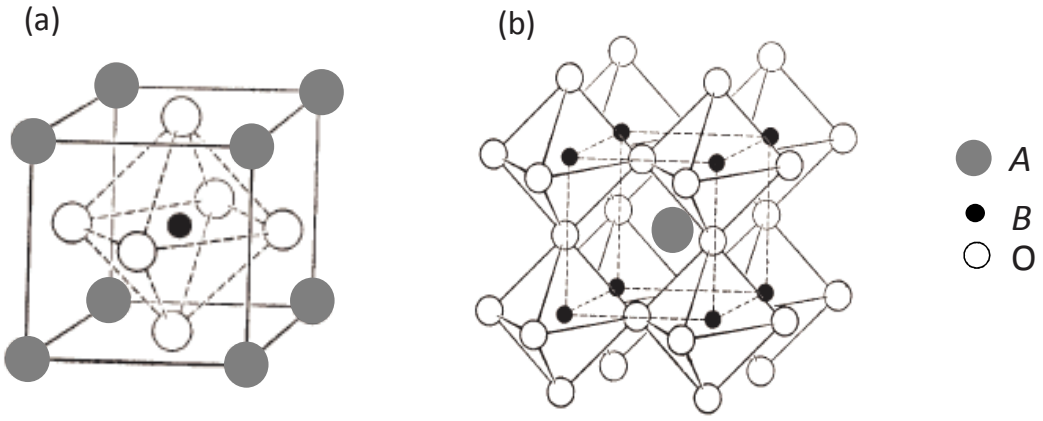

Figure 5.1: *Illustration of the perovskite crystal structure with the chemical formula ABO_3. The A, B and O-site atoms are represented by gray filled circles, small black filled circles, and open circles, respectively. (a) The unit cell of perovskite material, (b) the cubic $Pm\bar{3}m$ crystal structure. The figure is adopted from Ref [46].*

Crystal structure of $BiFeO_3$

$BiFeO_3$ is the only single phase room temperature multiferroic that is currently known, and it is commonly considered to be a model system for multiferroics. The atomic structure of $BiFeO_3$ was determined by Michel, et al., in 1969 [47], by performing X-ray diffraction on single crystals and neutron diffraction on powder samples. The room-temperature structure of $BiFeO_3$ is a highly rhombohedrally distorted perovskite with space group $R3c$ [47,48]. The $BiFeO_3$ crystal structure is different from the ideal perovskite crystal structure. The difference between the cubic $Pm\bar{3}m$ structure and the rhombohedral is the tilt of the adjacent FeO_6 octahedra and the displacement of Fe^{3+} and Bi^{3+} cations from their centrosymmetric position along $[111]_{pc}$ (pc denotes the pseudo cubic cell), as shown in Figure 5.2.

Due to the distorted rhombohedral crystal structure, the ferroelectric and ferroelastic order and a complex interplay between these parameters can be expected, despite of magnetic order parameter.

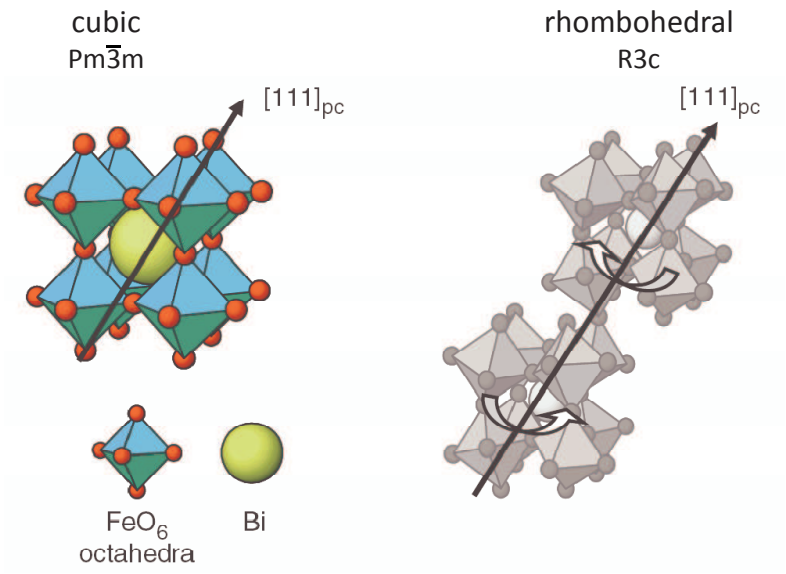

Figure 5.2: *Illustration of the ideal cubic $pm\bar{3}m$ and distorted rhombohedral crystal structure. The rhombohedral unit cell contains two connected $BiFeO_3$ perovskite units. This figure is adopted from Ref [45].*

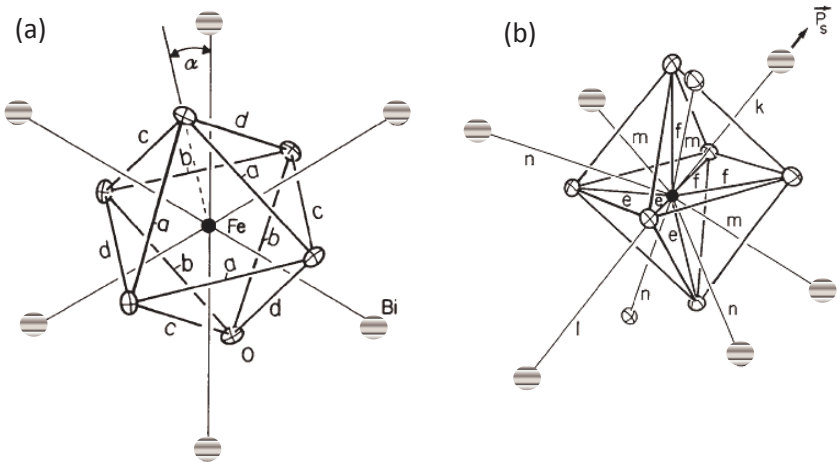

Figure 5.3: *A perovskite unit of $BiFeO_3$, (a) viewed along the threefold axis, (b) viewed perpendicular to the threefold axis. The shaded gray circles represent the Bi atoms, open circles with cross sign show O atoms, and filled circles show the Fe atoms. This figure is adopted from Ref. [48].*

A perovskite unit viewed along and perpendicular to the threefold axis is illustrated in Figure 5.3 [48]. The oxygen octahedron is distorted and its rotation is about $\alpha = \pm 13°$ around the threefold axis (see Figure 5.3 (a)). The Fe atom is shifted away from the center of the deformed oxygen octahedron by about 0.134 Å along the threefold axis (see Figure 5.3 (b)). The Bi atom is also shifted with respect to two neighboring octahedron centers by about 0.540 Å along the threefold axis. Bi-Fe distances are 3.0617 Å and 3.8726 Å labeled as *'k'* and *'l'* in Figure 5.3 (b), these distances explain the ferroelectricity. The antiferromagnetic superexchange occurs along the iron-oxygen chains even if the Fe-O angles are not exactly 180°. The main reason of the polarization of this material is the cooperative distortion of the Bi^{3+} and Fe^{3+} cations from their centro-symmetric positions

5.4 Normal vibrations of the perovskite lattice

It has been suggested through experimental and theoretical studies of solids, that the absorption bands in the infrared spectra are due to the excitation of optically active vibrations. The infrared allowed vibrations can be determined from the lattice symmetry arguments. The perovskite crystal with 3-degrees of freedom; translational, vibrational and torsional motion of the unit cell, 5 atoms, and N unit cells has total 15N-degrees of freedom (modes), 3N translational, 3N torsional, and 9N are the vibrational modes. The 9 vibrational modes of the unit cell are classified into 3 vibrational modes of A-site atom against the BO_3 group and 6 internal BO_3 vibrational modes. The interactions between these motions depend upon the masses and restoring forces of the vibrating atoms. The BO_3 group is arranged such that the B-atoms form octahedra with six oxygen O-atoms, and exhibit O_h symmetry [46], which describes six normal vibrational modes A_{1g}, E_g, $2F_{1u}$, F_{2u}, F_{2g}. To explain the normal vibrations of ABO_3 perovskite, here i used an example of $BaTiO_3$ [46]. I explain it for the case of $BiFeO_3$, because both compounds belong to the perovskite structure class. The illustration of the two F_{1u} normal vibrational modes is given in Figure 5.4; the two oxygen atoms along the Fe-O chain direction are labeled as O_I, and the other four oxygen atoms as O_{II}. In Figure 5.4 (a), the sketch of stretching vibrational modes is shown, which are mainly due to change in Fe-O_I bond length, and appears at high-frequencies compared to bending vibrational modes due to change in O_{II}-Fe-O_I bond angle, illustrated in Figure 5.4 (b).

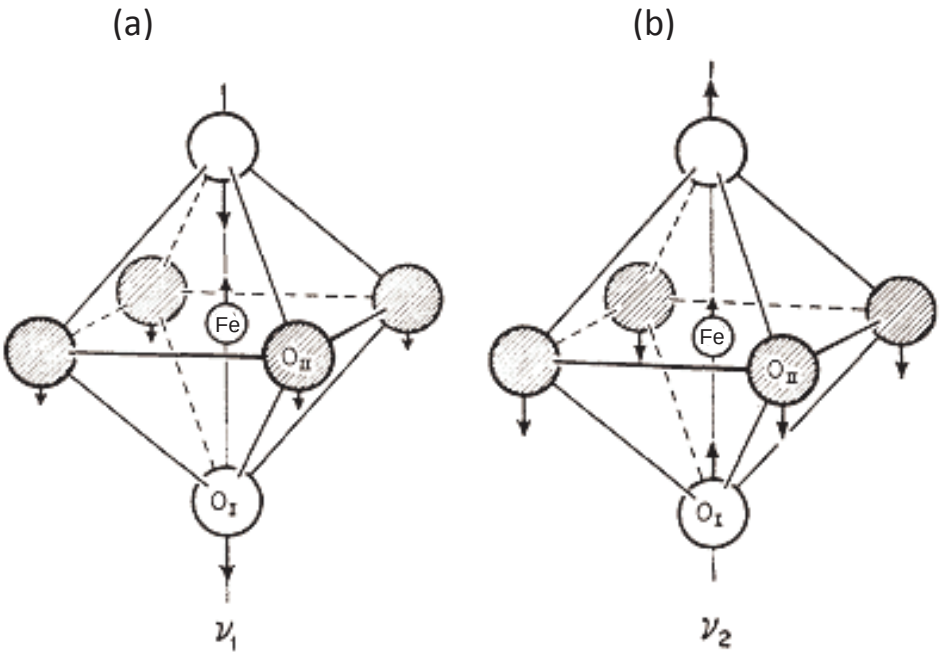

Figure 5.4: *The vibrations of FeO_6 octahedra (a) ν_1; the stretching modes observed in the higher-frequency range 400-850 cm^{-1} (b) ν_2 the bending modes observed in the lower-frequency range 200-400 cm^{-1}. The figure is taken from Ref [46] with small modification replacing Ti by Fe.*

The sign of the displacement and the magnitude depend on the force constant and the masses of the atoms. The vibrational modes will be triply degenerated, since three equivalent axes exist in a cubic lattice. By lowering the symmetry from cubic to tetragonal the degeneracy is partially removed and each of the bands (ν_1, ν_2) consist of doublet (E) and singlet (A_1) (see table 5.1). In the orthorhombic structure the degeneracy is completely removed, and each band is consist of three singlet (B_1, B_2 , A_1). In the rhombohedral structure the bands are again doublet and singlet, because the symmetry present in the rhombohedral structure is same as that of the tetragonal [46]. The rearrangement of symmetry species for different crystal symmetries are summarized in Table 5.1. The $BiFeO_3$ belongs to the $R3c$ ($C3_\nu{}^6$) space group shows 13 infrared- and Raman-active modes at room temperature, predicted by group theory analysis [49]. They can be classified according to the irreducible representations $4A_1 + 9E$, i.e., there are $4A_1$ modes polarized along the direction of the spontaneous polarization and $9E$ doublets polarized normal to this direction. In addition, there are $5A_2$ silent modes.

Symmetry	Point group	Species
Cubic	O_h	F_{1u}
Tetragonal	$C_{4\nu}$	E, A_1
Orthorhombic	$C_{2\nu}$	B_1, B_2, A_1
Rhombohedral	$C_{3\nu}$	E, A_1

Table 5.1: *The degeneracy of the ν_1 and ν_2 bands when the crystal structure changes, and symmetry species are rearranged relative to the point group of the respective crystal symmetry [46].*

5.5 Physical properties of $BiFeO_3$

The perovskite $BiFeO_3$ is a robust magnetoelectric multiferroic, with the coexistence of ferroelectric and antiferromagnetic order up to unusually high temperatures with Néel temperature $\approx$ 640 K and a ferroelectric Curie temperature $\approx$ 1100 K [50].

For many years, structural and physical properties of $BiFeO_3$ remained the subject of controversy. Recently much progress has been made to understand the multiferroics by investigating the effect of temperature, electric (magnetic) field, chemical substitution, and external pressure. The enhancement of ferroelectric polarization up to (60 $\mu C/cm^2$) [51] in epitaxial thin films of $BiFeO_3$, which is order of magnitude higher than previously observed polarization of bulk material (8.9 $\mu C/cm^2$) [52], was initially attributed to the effect of heteroepitaxial strain. The first-principle calculations [53] have shown that the large value of the ferroelectric polarization is an intrinsic character of $BiFeO_3$ and is not affected significantly by the presence of epitaxial strain. The concept has been experimentally proved by obtaining a comparatively high FE polarization (40 $\mu C/cm^2$) [54] of bulk $BiFeO_3$, much higher than the previously [52] observed value.

5.6 Pressure-induced phase transitions in $BiFeO_3$

$BiFeO_3$ is among the first discovered multiferroics, but its understanding is still limited; one of the reason is that, the synthesis of high quality $BiFeO_3$ samples is not easy and another reason is the lack of phonon studies of this material, which is important for the understanding of materials. The investigation of phonons has played a crucial role in the understanding of structural instabilities in classic ferroelectrics [49]. Phonons are also known to be influenced by spin correlations thus offering a potential complementary tool to magnetic probes, therefore the role of phonons with regard to multiferroic and magnetoelectric properties has attracted attention.

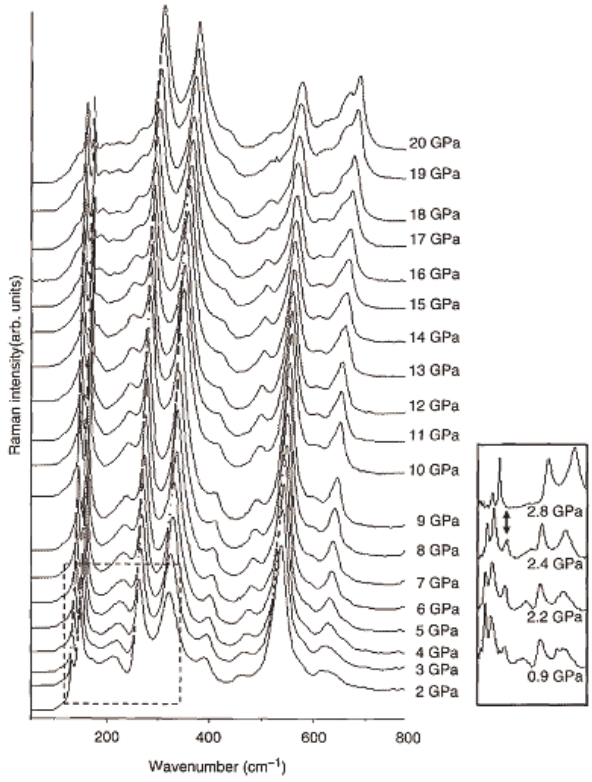

Figure 5.5: *Pressure-dependent Raman spectra of $BiFeO_3$, showing phase transitions at 2.5 GPa [45].*

The ME materials have been studied extensively, only very little is known about the effect of external high pressure on their multiferroic properties. The minute displacement of the atoms in the unit cell give spontaneous polarization, and it has been suggested that a phase transition in these ferroelectrics might results from the instability of one of the normal vibration modes of the lattice.

Regarding the phonon study, the Raman measurements under pressure on single crystal of $BiFeO_3$ by Haumont et al. [45] reveal the appearance of new modes and clear anomalies around 3 GPa only for the modes below 250 cm^{-1}, which are shown in Figure 5.5. They have also observed another phase transition at 9 GPa from the detailed analysis of different band chracteristics (wavenumber, intensity and/or line width). They have used argon as a pressure transmitting medium.

In Ref [55], the Raman spectra measured in the pressure range 0-50 GPa at room temperature clearly shows the two phase transitions below 10 GPa. In this study methanol-ethanol mixture was used as a pressure-transmitting medium. The spectra clearly illustrating the phase transitions are shown in Figure 5.6. In Figure 5.6 (c),

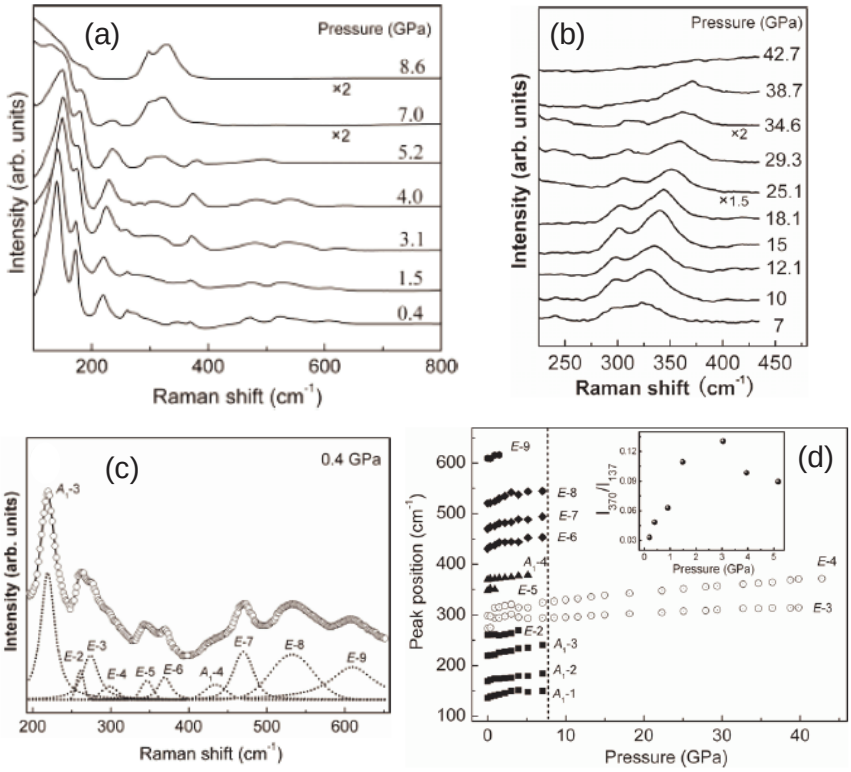

Figure 5.6: *(a)Raman spectra of $BiFeO_3$ measured in the pressure range of 0-8.6 GPa (b) Raman spectra of $BiFeO_3$ illustrating the lower-frequency phonons measured in the pressure range of 7-42.7 GPa. (c) The representation of E and A modes of the mid-frequency Raman spectra measured at 0.4 GPa. (d) The pressure-dependent evolution of the peak position of selected Raman modes. The vertical dotted lines indicate the pressures at which the transitions take place. The inset shows the intensity ratio of the E-6 mode to the A_1-1 mode in the pressure range of 0-6 GPa. The figure is adopted from [55].*

the modes polarized along the direction 'A' and normal to the polarization direction 'E'of spontaneous polarization are shown. In Figure 5.6 (d), the Raman modes near 300 cm^{-1} show the redshift of the phonon frequency at around 3 GPa which is attributed to the distortion of FeO_6 octahedra. Another phase transition is at around 8.6 GPa, clearly indicated by the disappearing of modes below 250 cm^{-1} together with the enhancement of two modes in the range of 300-400 cm^{-1} (see Figure 5.6 (b)), and these changes are attributed to the symmetry change from rhombohedral to orthorhombic. The third phase transition was observed at 44.6 GPa indicated by the

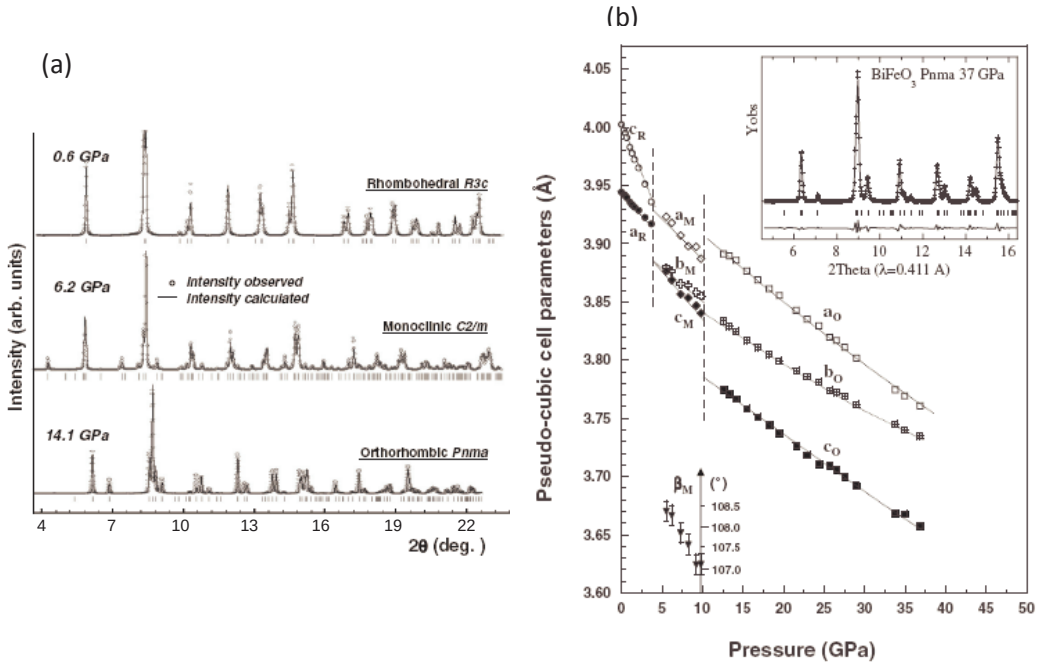

Figure 5.7: *(a)Diffraction diagrams with Rietveld refinement of $BiFeO_3$ at three selected pressures (0.6, 6.2, and 14.1 GPa) representing rhombohedral, monoclinic, and orthorhombic symmetries, respectively. (b) Lattice parameters of the pseudo cubic unit cell of $BiFeO_3$ as a function of pressure, clearly showing discontinuous changes at 3 GPa and 10 GPa revealing two structural phase transitions. The inset showing a part of the diffraction pattern obtained at the highest investigated pressure of 37 GPa, reveals the orthorhombic Pnma structure which is maintained even up to this pressure. The figure is adopted from Ref [56].*

disappearing of E-3 and E-4 modes, this transition is due to the symmetry change from orthorhombic to cubic, and it directly supports the speculated pressure-induced insulator-metal transition. The theoretical ab initio based calculations have predicted a single pressure-induced structural transition from the initial rhombohedral R3c structure to an orthorhombic Pnma ($GdFeO_3$-type) structure around 13 GPa [57].

The structural analysis of $BiFeO_3$ under high pressure up to 37 GPa was performed by X-ray powder diffraction experiments at the European Synchrotron Radiation Facility (ESRF) on the ID09A high-pressure beamline. Hydrogen as a pressure transmitting medium was used. The significant changes in the multiplicity and intensity of the Bragg peaks were observed at P_{c1}=3.6 GPa and P_{c2}=10 GPa, which reveal the

two structural phase transitions. The XRD results are shown in Figure 5.7. In Figure 5.7 (a), numerous weak reflections appear above 3.6 GPa in the diffraction pattern, which is evidence of new phase [56].

In Figure 5.7 (b), the pressure-dependence of the pseudocubic unit cell parameters of $BiFeO_3$ are given, which are instructive for phase transition. In this figure there are subscripts (R, M and O) with cell parameters, representing the space group rhombohedral, monoclinic and orthorhombic. The rhombohedral phase is very sensitive to pressure, which is reflected by significant decrease in both a_R and c_R. This first phase transition at P_{c1} from R3c to C2/m corresponds to a change in cation displacements and a change in the oxygen tilting system. Moreover, within the monoclinic region the lattice parameters decrease with increasing pressure leading to a compressibility, and the β_M angle decreases slowly from 108.24°(6.2 GPa) to 107.13° (9.8 GPa) but does not reach 90° before the M→O transition. A further increase in the pressure induces a phase transition at p_{c2} from the monoclinic phase to the Pnma orthorhombic phase, which is nonpolar, but with a distortion due to octahedra tilts. Another important point is that the discontinuous changes in the cell parameters at $P_{c1}$and P_{c2} indicate that both R→M and M→O phase transitions are of first order.

Controversial to the above findings, recently there were experimental [58–61] (X-ray diffraction, nuclear forward scattering, X-ray emission method, optical absorption and DC resistivity measurement) and theoretical [62] studies on $BiFeO_3$ under high pressure, where they found anomalies around 45-55 GPa in their data. They did not observe any anomaly below 15 GPa. This is surprising, because ferroelectric instabilities are known to be very sensitive to pressure, and therefore all ferroelectric perovskites usually show at least one structural phase transition below 15 GPa.
The aim of this study is to verify experimentally the occurrence of the pressure-induced phase transition sequence in $BiFeO_3$ below 15 GPa. High-pressure infrared studies of phonon modes are rare in the literature, mainly because of the experimental difficulties when compared with Raman scattering.

5.7 High pressure infrared reflectivity of multiferroic perovskite $BiFeO_3$

5.7.1 Far-infrared high pressure experiment

Repeated pressure-dependent far-infrared reflectivity measurements up to 10 GPa at room temperature were carried out on the surface of as-grown $BiFeO_3$ crystals (sample size about 80 μm × 80 μm × 40 μm) at the infrared beamline of the synchrotron radi-

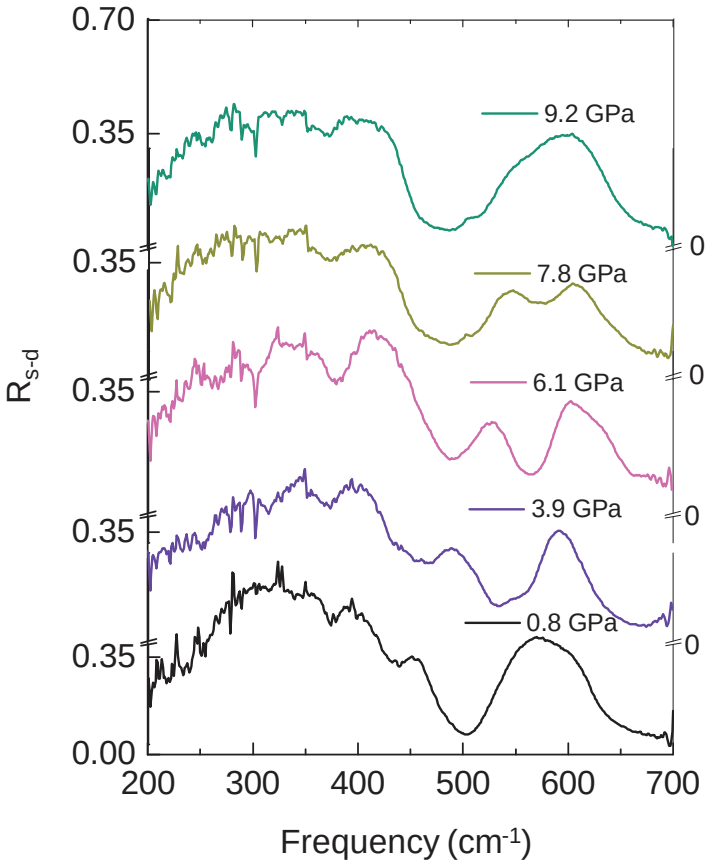

Figure 5.8: *Room-temperature reflectivity R_{s-d} spectra of $BiFeO_3$ for few selected pressures.*

ation source ANKA in Karlsruhe. The explanation about the measurement procedure is given in Chapter 2. The far-infrared reflectivity spectra for few selected pressure are shown in Figure 5.8.

5.7.2 Results and discussion

The reflectivity spectra were fitted with the generalized-oscillator model with the factorized form of the complex dielectric function, which is described in chapter.2. To fit the reflectivity data under pressure, the values of the high-frequency permittivity ϵ_∞ as a function of pressure are needed, which were calculated by using the Clausius-Mossotti relation [63]:

$$\frac{\epsilon_\infty(P)-1}{\epsilon_\infty(P)+2} = \frac{\widetilde{\alpha}N}{3\epsilon_0 V(P)}, \tag{5.1}$$

where $\widetilde{\alpha}$ is the average atomic polarizability of the unit cell, which was obtained

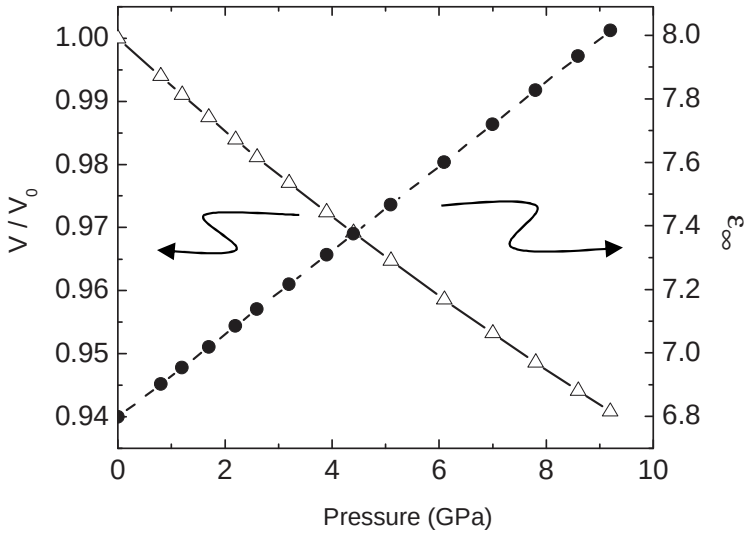

Figure 5.9: *Pressure dependence of the unit cell volume, calculated according to the first order Birch equation of state Equation (5.2) and the high-frequency permittivity ϵ_∞ as a function of pressure, calculated according to the Clausius-Mossotti relation, Equation (5.1).*

from the lowest-pressure data, *V(P)* is the unit cell volume as a function of pressure calculated from the first-order Birch equation of state [64, 65]:

$$P(x) = \frac{3}{2} B_0 x^{-7}(1 - x^2), \tag{5.2}$$

where $x = [V(P)/V(0)]^{1/3}$. For the bulk modulus at zero pressure we assumed B_0=111 GPa from the experimental XRD data [56]. The resulting pressure dependence of the unit cell volume is presented in Figure 5.9 together with the high-frequency permittivity ϵ_∞ as a function of pressure.

The estimated value of ϵ_∞ at ambient pressure is 6.8. It is higher than the value of 4.0 reported for $BiFeO_3$ ceramics [66], but lower than $\epsilon_\infty = 9.0$ reported for single crystals [49]. Therefore, the ϵ_∞ value used in this work is reasonable. The fit of the measured reflectivity spectrum at 0.8 GPa is compared to the simulated ambient pressure spectrum in the diamond anvil cell using the fitting parameters from Ref [49] are shown in Figure 5.10. Both reflectivity spectra look similar but the overall reflectivity level is different. The other main differences are the sharpness of the phonons and the mode at 274 cm^{-1} observed by Lobo et al [49] marked by an asterisk in the reflectivity curve, this mode becomes weaker in pressure measurements due to the broadening effect. This feature could not be resolved reliably in pressure-dependent measured spectra and therefore it was neglected in the fitting procedure.

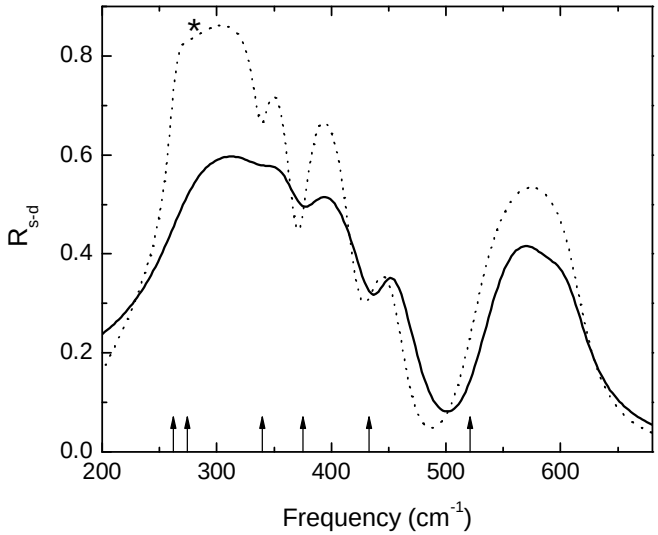

Figure 5.10: *Fit of the measured reflectivity spectrum of $BiFeO_3$ at 0.8 GPa (solid line) compared to the simulated ambient pressure spectrum in the diamond anvil cell using the fitting parameters from Ref [49] (dashed line). The arrows indicate the frequencies of TO phonons found by Lobo et al. [49] The asterisk marks the kink produced by the mode at 274 cm^{-1}.*

$\omega_{TO}(\gamma_{TO})$	$\omega_{TO}^{amb}(\gamma_{TO}^{amb})$	$\omega_{LO}(\gamma_{LO})$	$\Delta\epsilon$	$\Delta\epsilon^{amb}$
269 (51)	262 (9.1)	348 (41)	18.2	14.8
	274 (33.5)			2.45
348 (36)	340 (17.4)	374 (43)	0.023	0.27
380 (41)	375 (21.6)	433 (43)	0.32	0.475
443 (33)	433 (33.8)	472 (44)	0.15	0.301
529 (48)	521 (41.3)	588 (48)	0.69	1.14
592 (46)		614 (37)	0.019	

Table 5.2: *Room-temperature fitting parameters to describe the reflectivity spectrum of $BiFeO_3$ at 0.8 GPa, compared to the room-temperature parameters obtained at ambient pressure by Lobo et al. [49], denoted by $\omega_{TO}^{amb}, \gamma_{TO}^{amb}$ and $\Delta\epsilon^{amb}$.*

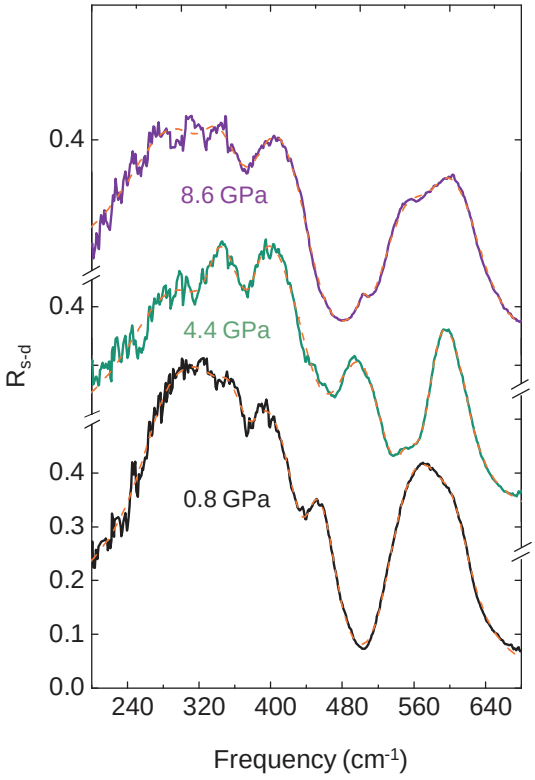

Figure 5.11: *Illustration of the fit with the 4p-model for three selected pressure (0.8, 4.4, 8.6 GPa); The dashed lines are the fits, the spectra are presented with an offset along the vertical axis for clarity.*

According to the fit of the data with the generalized-oscillator model the transverse optical modes are located at 269, 348, 380, 443, 529 and 592 cm^{-1} for the lowest measured pressure (0.8 GPa).
The frequencies of the these transverse optical modes are in good agreement with the results for $BiFeO_3$ single crystal obtained by Lobo et al [49] at ambient condition. The damping constants γ_{TO} are higher in the case of pressure measurements. The comparison of both results is given in Table 5.2.

The frequencies of the optical phonons have been calculated theoretically [67] and determined experimentally by infrared [49] and Raman [68, 69] spectroscopy on single $BiFeO_3$ crystals. All the phonon modes listed in Table 5.2, besides the weak mode at 592 cm^{-1}, belong to the E representation. E phonon modes are polarized normal the direction of spontaneous polarization $[111]_{pc}$. This indicates that the electric field of the synchrotron radiation used in infrared high pressure experiment was polarized approximately along the $[-110]_{pc}$ direction, similar to the experiment of Lobo et al. [49].

In Figure 5.11, the reflectivity spectra for three selected pressures with the corre-

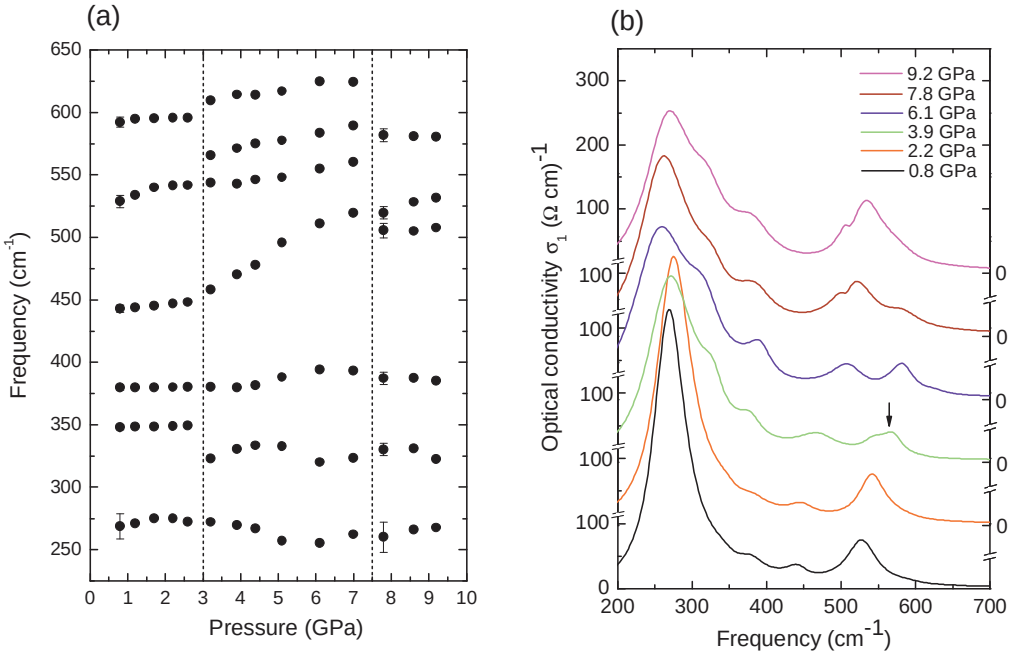

Figure 5.12: *(a) Frequencies of the transverse optical phonons in $BiFeO_3$ as a function of pressure, obtained by fitting the reflectivity spectra $R_{s-d}(\omega)$ with the generalized-oscillator model. The vertical dashed lines indicate the pressures of the two phase transitions. (b) Real part $\sigma_1(\omega)$ of the optical conductivity of $BiFeO_3$ for selected pressures, obtained by fitting the reflectivity spectra $R_{s-d}(\omega)$ with the generalized-oscillator model; the spectra are presented with an offset along the vertical axis for clarity. The arrow marks the position of the phonon mode at 565 cm^{-1} emerging above 3 GPa.*

sponding fits are shown. These spectra are presented with offset along the vertical axis for clarity. From the fit the frequencies as a function of pressure are extracted and plotted (see Figure 5.12 (a)). Below 3 GPa the reflectivity spectra in the measured frequency range can be well fitted using six oscillators. Above 3 GPa an additional oscillator was needed for a reasonable fit of the spectra. Finally, above 7.5 GPa the number of oscillators reduces to six again. The evolution of the optical conductivity $\sigma_1(\omega)$ with increasing pressure is shown in Figure 5.12 (b). One can clearly see the changes of the optical conductivity spectra across the transition pressures $P_{c1} = 3$ GPa and $P_{c2} = 7.5$ GPa.

On comparison with the phonon spectra of typical perovskite materials like $LaTiO_3$ and $BaTiO_3$, [46, 70] the experimentally observed modes can be attributed to FeO_6

octahedral bending and stretching modes (in the frequency ranges 200-400 cm^{-1} and 400-850 cm^{-1}, respectively). The Bi ions are involved only in the lower-frequency (<200 cm^{-1}) modes located below the measured frequency range of this study. The change in the pressure dependence of the phonon mode frequencies at P_{c1} and P_{c2} could thus be assigned to changes in the octahedral distortion, because the bending and stretching modes of the FeO_6 octahedra, exhibit a displacement of the Fe^{3+} cations from their centrosymmetric position along the pseudocubic $[111]_{pc}$ direction [48, 71].

The XRD data [56] under pressure supports our pressure-dependent far-infrared reflectivity data. $BiFeO_3$ undergoes two pressure-induced instabilities. A first structural phase transition occurs at 3 GPa and is attributed to the superimposition of FeO_6 octahedra tilts and cations displacement, and the structure changes from rhombohedral to monoclinic. A second structural phase transition at 7.5 GPa (IR) and 10 GPa (XRD) [56] is due to the structural changes from monoclinic to orthorhombic with *Pnma* symmetry. This second phase transition is an agreement with a recent theoretical *ab-initio* prediction. In second transition with *Pnma* symmetry the unit cell contains 4 formula units,i.e, twice the atoms than the rhombohedral $R3c$ unit cell with 2 formula unit. The phonon modes become doubled in orthorhombic structural phase. The increased number of modes in the *Pnma* phase compared to 13 modes in the R3c phase should originate from the splitting of the E symmetry doublets and the general doubling of all modes due to the unit-cell doubling. Therefore a splitting of the phonon modes across the transition pressure is expected, although some modes can vanish due to the selection rules. The infrared measurements present a similar effect above 7.5 GPa, where the phonon mode located at 520 cm^{-1} splits into two modes below the transition pressure (see Figure 5.12 (b)).

The second pressure-induced phase transition in infrared study occurs at P_{c2}=7.5 GPa. The X-ray powder diffraction study [56] shows the second phase transition from monoclinic to orthorhombic at 10 GPa, in this study the hydrogen was used as a pressure transmitting medium. The high pressure Raman study of $BiFeO_3$ by Y.Yang et al. [55] reveals one of the pressure-induced phase transition at 8.6 GPa, which is attributed to the symmetry change from rhombohedral to orthorhombic. They used methanol-ethanol mixture as a pressure transmitting medium. Another high pressure Raman study by Haumont et al. [45] shows one of the pressure-induced phase transition at 9 GPa, argon was used as a pressure transmitting medium in this study. The discrepancy in the P_{c2} was understood by different pressure transmitting media.

The recent high pressure X-ray diffraction study on single crystal of $BiFeO_3$ with hydrostatic (helium) and non-hydrostatic (silicon oil) pressure medium [72] show the phase sequence R3c$\longrightarrow$PhaseII$\longrightarrow$PhaseIII$\longrightarrow$Pnma

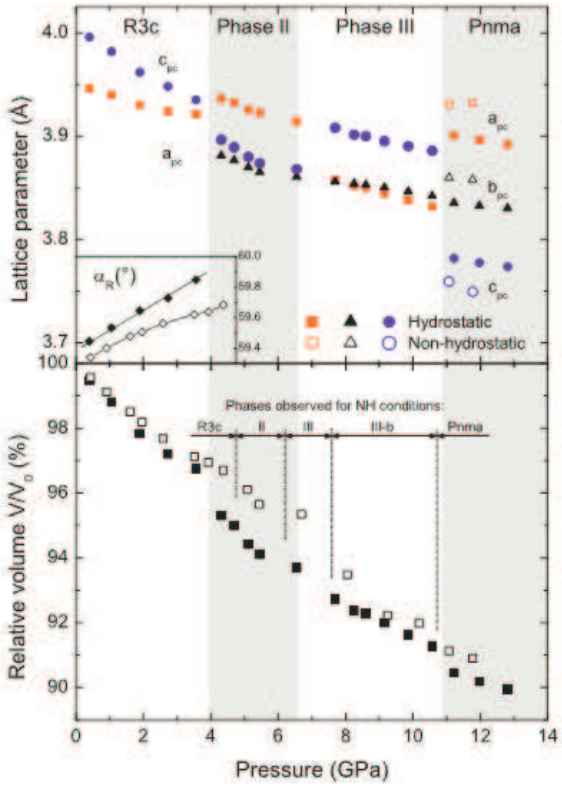

Figure 5.13: *The lattice constants in the top panel, the rhombohedral angle is shown as an inset. In the bottom panel the relative volume is shown. The filled and open symbols correspond to hydrostatic and non-hydrostatic conditions, respectively. The grey colored stripes represent the domains of various phases for hydrostatic conditions. The phase sequence for non-hydrostatic conditions is indicated by dashed lines in the volume plot. The figure is taken from Ref [72].*

and R3c⟶PhaseII⟶PhaseIII⟶PhaseIIIb⟶Pnma , respectively. The transition pressures are consistent with X-ray powder diffraction and infrared study [56], except the intermediate transition from PhaseII-PhaseIII. For PhaseII and PhaseIII orthorhombic space group is used by Belik et al. [73], but Guennou et al. [72] and Haumont et al. [56] used monoclinic C2/m space group to calculate lattice constants. The different phase transitions are shown in Figure 5.13, the transition pressure for PhaseIII in case of hydrostatic and for PhaseIIIb in case of non-hydrostatic conditions is consistent with P_{c2}=7.5 GPa of infrared data.

6 Effect of pressure on the optical properties of spinels

6.1 Crystal Structure of Spinels

The class spinels is described by the general formula AB_2X_4, where X represents the anion and A and B are the cations. The conventional cubic unit cell of spinels shown in Figure 6.1 (a) has 8 formula units, i.e., in total 56 atoms of which 32 are anions and 24 cations. The A-site cations are tetrahedrally coordinated with X-anions, while B-site cations are in octahedral environment, as shown in Figure 6.1 (b) and (c), respectively. There are 96 interstices between the anions in the cubic unit cell of which 64 are tetrahedral interstices and 32 octahedral interstices. Out of 64 tetrahedral interstices, 8 are occupied by cations and the remaining 16 cations occupy half of the 32 octahedral interstices [74].

The tetrahedrally coordinated cations form a diamond cubic sublattice and the octahedrally coordinated cations form a corner shared pyrochlore lattice as shown in Figure 6.1 (d). The anions are arranged in a pseudocubic close-packed (ccp) form. The A-site tetrahedra in spinels are isolated from each other and share corners with neighbouring B-site octahedra. No edge sharing occurs between A-site tetrahedra and other A- or B-site polyhedra. B-site octahedra share six of twelve X-X edges with nearest neighbor B-site octahedra. The other six edges are shared with octahedra that are surrounded with vacant sites. The X-X edges that are shared by the B-cations form chains in the lattice along the (110) directions. Because no intervening anions obstruct neighboring B-site cations, the B-B distances are short which facilitates the electrical conductivity in some spinels, via electron hopping between B-sites [75–77].

The manner in which the cations are distributed amongst the tetrahedral and octahedral sites gives rise to two different classes of spinels [75, 76]: (i) Normal spinels and (ii) Inverse Spinels. Many compounds that exhibit the spinel structure can accommodate significant amounts of cation disorder. A normal 2-3 spinel refers to a compound that is composed of divalent and trivalent cations, the divalent minority cations occupy the tetrahedral A-sites, whereas the trivalent majority cations reside

in octahedral B-sites. For example, $ZnCr_2Se_4$ is a normal spinel compound, which has a divalent cation (Zn) on the A-site and trivalent cation (Cr^{3+}) on the B-site. In inverse 4-2 spinels, e.g., $TiMg_2O_4$, the A-sites are filled entirely by divalent majority cations (Mg^{2+}), whereas the B-sites are occupied by divalent majority (Mg^{2+}) and quadravalent minority (Ti^{4+}) cations, in equal proportions. The structural formula for spinels with composition AB_2X_4 may be written as follows:

$$[B_i^{q+}A_{1-i}^{p+}]^{AIV}[A_{i/2}^{p+}B_{(2-i)/2}^{q+}]_2^{BVI}X_4 \tag{6.1}$$

where A^{p+} and B^{q+} are minority and majority cations, respectively. The first quantity in brackets represents the average occupancy of A-sites (coordination number of four (IV)), whereas the second quantity in brackets represents the average occupancy of B-sites (coordination number of six (VI)). The variable i is the so-called inversion parameter, which specifies the fraction of A-sites occupied by majority ions. For normal spinels, i=0; for random cation arrangements, i =2/3, and for inverse spinels, i=1, the variables p and q refer to the average charge of the cations occupying the A- and B-sites, for different cation configuration [74]. In this chapter, the investigated spinels are $A(Cr, V)_2X_4$, where A=Zn^{2+}, Mg^{2+}, Cd^{2+} and Hg^{2+} and X=O^{2-}, S^{2-}, and Se^{2-}. The B-site chromium and vanadium are trivalent cations.

Figure 6.1: *Crystal structure of normal spinels, (a) the cubic unit cell, (b) A-site cations form tetrahedra with anions at the X-site and (c) B-site cations make octahedra with the X-site anions. (d) A-site sublattice is a diamond cubic lattice and B-site sublattice forms network of corner shared tetrahedra named as pyrochlore lattice.*

6.2 Electronic States of *d*-electron systems

In solid state, the atomic orbitals form bands due to the periodic arrangement of the atoms. The band width is determined from the overlap of the valence of adjacent atoms. In transition-metal compounds, the overlap is determined by indirect transfer between d-orbitals through ligand p-orbitals. In this case the bandwidth is determined by the overlap of the d-wavefunction at a transition-metal atom and the p-wavefunction at the adjacent ligand atom. The ligand atoms form bridges between two transition-metal atoms, and because of this indirect transfer through ligand atomic orbitals, the d-bandwidth becomes narrower [78]. The $3d$-orbitals under the strong influence of the octahedral crystal-field (CF) split in a higher energy level e_g(two-fold degenerate) and lower energy level t_{2g}(three-fold degenerate). Apart from strong spin fluctuations, effects of orbital fluctuation and orbital symmetry breaking play important roles in many d-electron systems. In this regard the orbital degeneracy is an important and unavoidable source of complicated behavior. In this chapter, the investigated systems have Cr^{3+} and V^{3+} in octahedral environment. The electronic configuration is $3d^3$ and $3d^2$ with total spin S=3/2 and S=1, respectively.

6.2.1 Free transition metal ion

In the partially filled shell the interaction between electrons is less compared to the filled shell. The electrons in a shell of a free ion are subject to two main interactions; First, the electrons in a shell repel each other and the energy of the configuration (d^1, d^2, d^3, etc.) depends on how the electrons occupy the orbitals of the shell relative to one another. Secondly there is an interaction of electron spins and orbital angular momenta. The interelectronic repulsion breaks the degeneracy of the orbital into a number of energy levels. As an example, the splitting of the d^2 configuration due to the interelectronic repulsion and the spin-orbit coupling is shown in Figure 6.2. The energy levels S, P, D, F and G are characterized by the total orbital angular momentum L and total spin angular momentum S [79]. These energy levels are labeled by using the nomenclature $^{(2S+1)}X$, where the quantity (2S+1) is the multiplicity of that energy level. For the total angular momentum, L= 0, 1, 2, 3, 4, 5, ..., the X will be X= S, P, D, F, G, H...., respectively. The energy levels for d^3 configuration are ^4F, ^4P, ^2H, ^2G, ^2F, 2* ^2D, ^2P. The lowest energy level is determined by the application of the Hund´s rule, which states that the level with maximum multiplicity tends to lie lowest in energy [79]. The energies of the different levels are a function of the electron repulsion parameters called Racah parameters B and C. For the separation between the energy levels of the same multiplicity factor, only parameter B is involved, while for a different

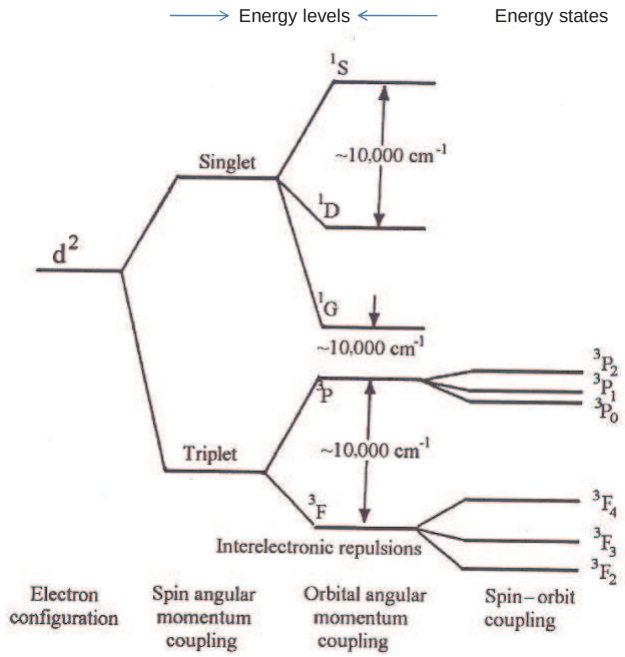

Figure 6.2: *The splitting of the d^2 configuration due to interelectronic repulsion and spin-orbit coupling, which is the case for V^{3+}. The energy levels are named singlet and triplet according to the total spin (S) values 0 and 1, respectively. The figure is adopted from Ref [79].*

multiplicity of energy levels both B and C are involved. For free transition-metal ion, the energy separation between adjacent energy levels is of the order of 10,000 cm^{-1} and it is larger than the spin-orbit coupling energies of transition-metal ion in the first transition series.

Each energy level of a configuration (d^n) is (2L+1)(2S+1)-fold degenerate. In case of an unfilled shell of electrons of free ion, the spin-orbit coupling is considered as a small perturbation on the energy levels which are set up by electronic repulsion. The each energy level (*S*, *P*, *D*, etc) is split up into a number of states, which are specified by the total angular momentum J due to L-S coupling. Each state is (2J+1)-fold degenerate. The J ranges from $|L - S|$ to $|L + S|$, and the lowest value of J, $|L - S|$, lies at the lowest energy. The nomenclature to represent the state energy is $^{(2S+1)}L_J$. The parameter which measures the strength of the interaction between spin and orbital angular momenta of a single electron is ζ. The experimentally observed and theoretically calculated energy levels of Cr^{3+}ion [80] are shown in Figure 6.3.

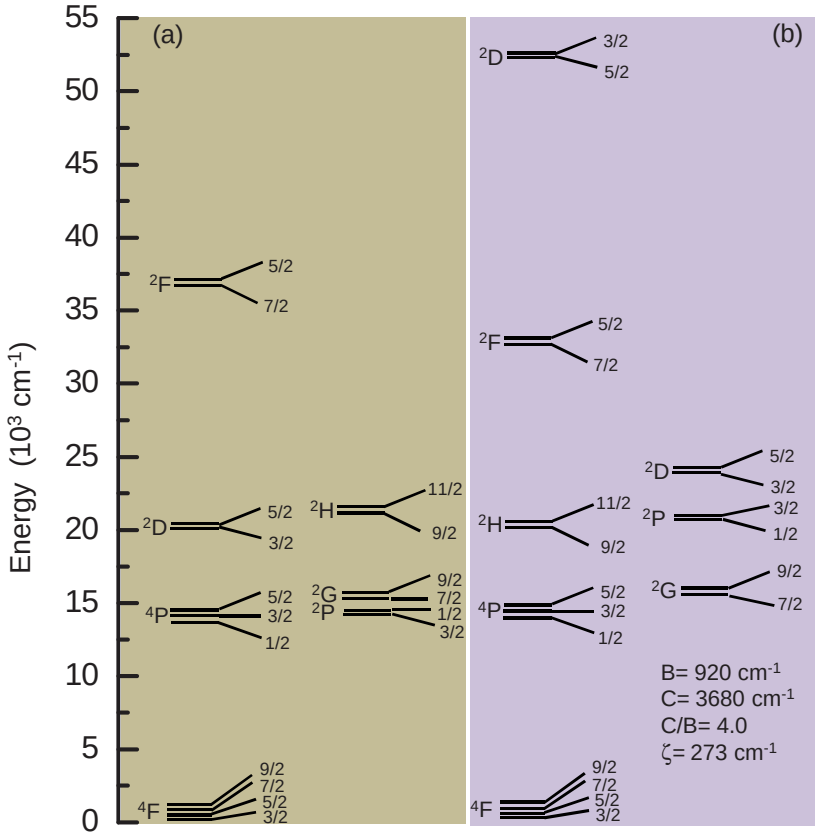

Figure 6.3: *(a) The experimentally observed energy levels and (b) the theoretically calculated energy levels of the Cr^{3+} free ion. The figure is adopted from Ref [80].*

6.2.2 Crystal-field

The crystal-field theory describes the electrostatic interaction between the central metal ion and surrounding ions or ligands. In case of an isolated transition-metal atom or ion all five *d*-orbitals are alike in energy (five-fold degenerate). In a crystal, the spherical symmetry of the ion will be reduced due to the strong anisotropic CF and the fivefold orbital degeneracy is lifted. This leads to a splitting of the energy levels and is called the crystal field splitting (Δ_{CF}). If the electrostatic interaction between the metal ions and ligands is stronger than the electron-electron interaction within the ion, this gives a strong crystal-field. If the electrostatic interaction between the central metal ion and surrounding ligands is less than the electron-electron interaction but larger than the spin orbit coupling, the crystal-field will be intermediate. The crystal-field effect is weak if the electrostatic interaction between the central metal ion and surrounding ligands is smaller than the electron-electron interaction and the spin

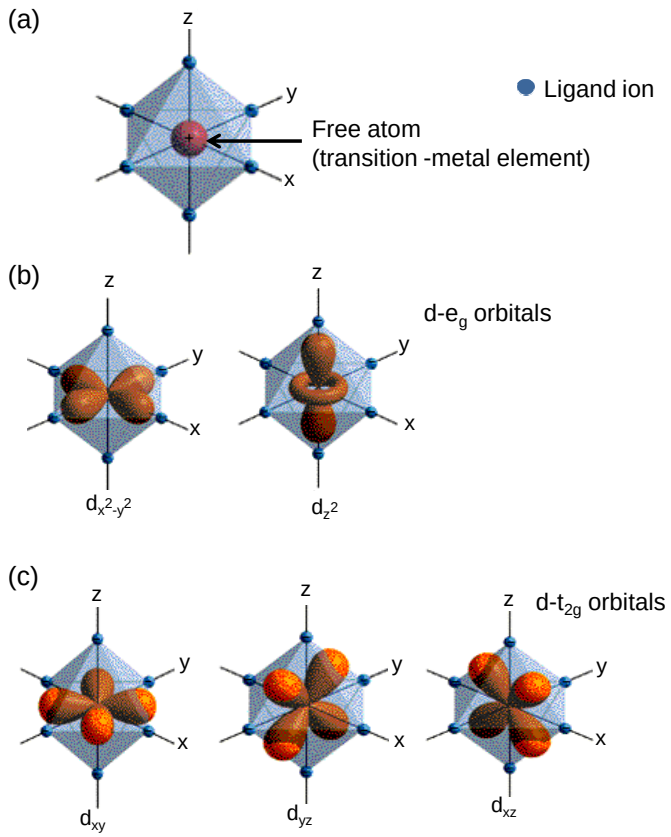

Figure 6.4: *The configuration of transition metal 3d-orbitals under octahedral crystal-field. The blue colour filled circles pointing towards the x, y, and z axes are the ligand atoms.*

orbit coupling [81]. Moreover, the interaction of d-orbitals of transition-metal ion with ligand atoms in octahedral and tetrahedral environment is different.

Octahedral crystal-field

In case of the octahedral crystal-field, all d-orbitals will not interact to the same extent with the six ligand atoms located on the +x, -x, +y, -y, +z and -z axes respectively, which are illustrated in Figure 6.4. The orbitals which lie along these axes (i.e. $d_{x^2-y^2}$, d_{z^2}) will be destabilized more because of the strong repulsion between the electrons of the ligand ion and the d-electrons of transition-metal ion. Therefore these $\mathbf{d}_{x^2-y^2}$, d_{z^2} (e_g) orbitals will be at higher energy than the orbitals which lie in between the axes (i.e. d_{xy}, d_{xz}, d_{yz}) (t_{2g}) orbital. The splitting of five d-orbitals in the octahedral crystal-field with cubic O_h symmetry is shown in Figure 6.5. This crystal-field splitting between the

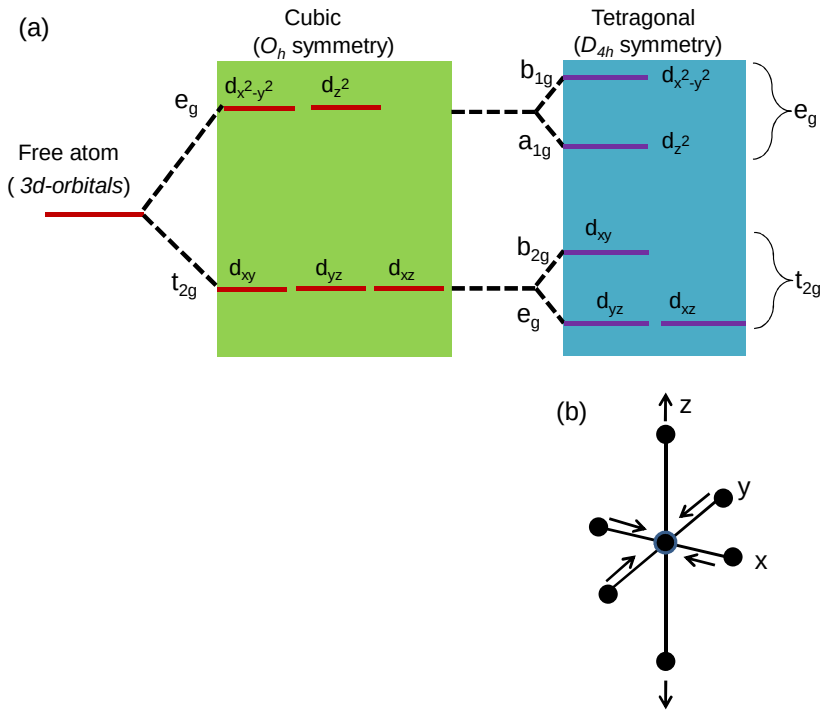

Figure 6.5: *(a) Crystal-field splitting of 3d-orbitals under the octahedral crystal field of cubic O_h and tetragonal D_{4h} symmetries (b) the distortion of the octahedron during the transition from cubic symmetry to tetragonal symmetry. The figure is taken from Ref [81] with small modification.*

t_{2g} and the e_g levels is often defined as 10Dq. When the symmetry changes from cubic to tetragonal, the two e_g orbitals of the octahedral field become non degenerate as a_{1g} and b_{1g} in the tetragonal field. Degeneracy among the t_{2g} orbitals in O_h symmetry, is partially lifted to become b_{2g} and e_g in the tetragonal field with D_{4h} symmetry.

By considering the tetragonal symmetry on transition metal site, the distortion of the octahedron by moving the two ligands (along z-axis) away from the central metal ion exhibits D_{4h} symmetry is shown in Figure 6.5. In this case the repulsion is lower between ligand electrons and the metal electrons in *d*-orbitals that have a substantial electron distribution along z. Thus the energies of thed_{xz}, d_{yz}, and d_{z^2} orbitals are lowered. It is assumed that the stretching along the z-axis is accompanied by a counterbalancing contraction in the xy-plane, so as to maintain the overall energy of the system, then the orbitals with substantial electron distribution in the xy-plane will experience increased repulsions. Thus, the d_{xy} and $d_{x^2-y^2}$ orbitals rise in energy.

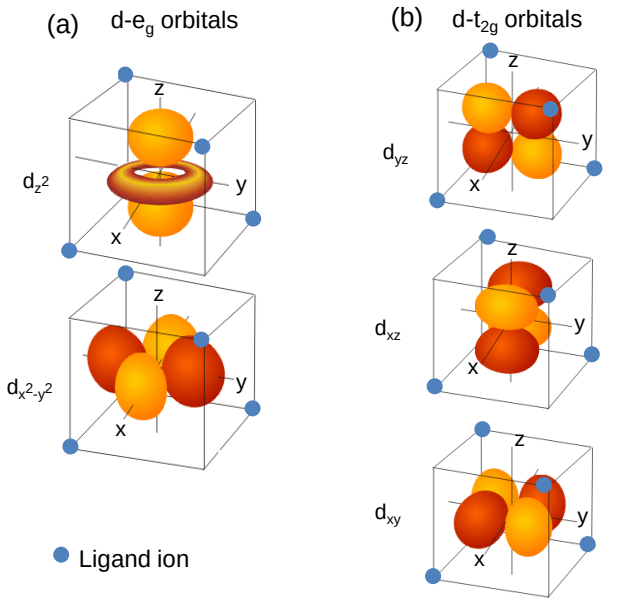

Figure 6.6: *The configuration of transition-metal 3d-orbitals under tetrahedral ligand arrangements. The blue colour filled circles are the ligand atoms.*

Tetrahedral crystal-field

In a tetrahedral arrangement of T_d symmetry, the $d_{x^2-y^2}$ and d_{z^2} orbitals (e_g orbitals) lie between the ligands, while the d_{xy}, d_{xz}, d_{yz} orbitals (t_{2g} orbitals) are directed more in the direction of the ligands as shown in the Figure 6.6. As a result, the electrostatic

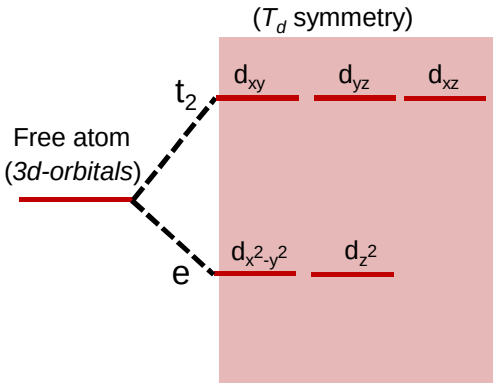

Figure 6.7: *The splitting of 3d-orbitals under the tetrahedral crystal-field of T_d symmetry. The figure is taken from Ref [81] with small modification.*

repulsion between the electrons of the ligand and the e_g orbitals of the transition-metal is less compared to the electrostatic repulsion between the electrons of ligand atoms and that of t_{2g} orbitals of the transition-metal. Consequently the e_g orbitals have lower energy compared to t_{2g} orbitals. This is because only four bonds are formed and the metal orbitals used in the bonding do not point right at the ligands as they do in octahedral complexes. The splitting of the five d-orbitals in tetrahedral crystal-field with T_d symmetry is shown in the Figure 6.7.

Spin states

In d^1 - d^3 electron systems, Hund´s rule predicts that the electrons will not pair and occupy the t_{2g} levels. In comparison to that, in d^4 electron systems, three electrons can occupy the t_{2g} levels but for the fourth electron there are two possibilities: either it goes to the e_g level, and electrons do not pair, called the high spin (HS) state or it occupy the t_{2g}levels and therefore electrons are partially paired and leads to low spin (LS) state. Both HS and LS are illustrated in Figure 6.8. The investigated materials

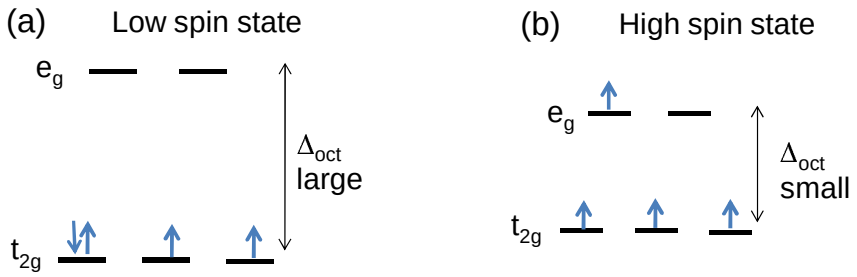

Figure 6.8: *(a) Low-spin (LS) state and (b) high-spin (HS) of a transition-metal ion in an octahedral environment with a d^4 configuration.*

described in this chapter have Cr^{3+} and V^{3+} in octahedral arrangement with electronic configuration $3d^3$ and $3d^2$, respectively.

6.2.3 Tanabe-Sugano diagram

For d-electron systems, the splitting of energy levels depends not only on the CF effect but also on the electrostatic repulsion between d-electrons and the spin orbit interaction. The Hamiltonian for the d-orbitals is [82]

$$H = H_{CF} + H_{es} + H_{so}. \tag{6.2}$$

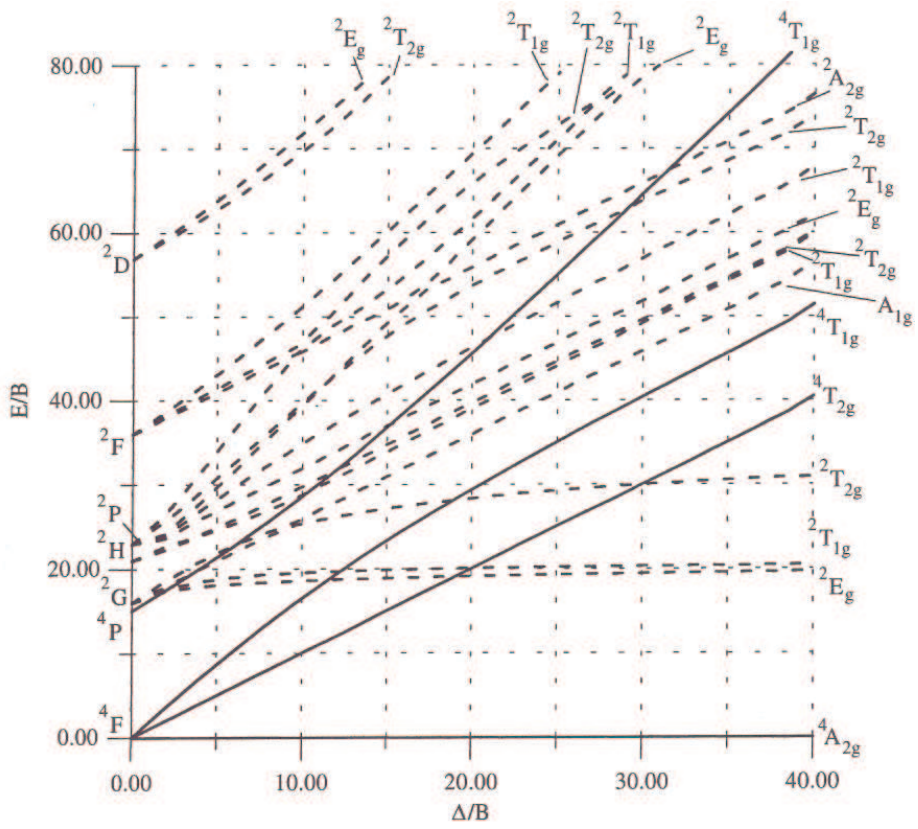

Figure 6.9: *Tanabe-Sugano diagram of energy levels for a chromium ion with $3d^3$ configuration in an octahedral crystal field (B= 933cm^{-1}, C =4.5B). The solid lines show the level of spin-allowed transitions. The figure is adopted from Ref [79].*

H_{CF} represents the CF splitting, H_{es} is the electrostatic repulsion between d-electrons and H_{so} is the spin orbit interaction. For the $3d$-series the magnitude of spin-orbit coupling is smaller compared to the other terms in the Hamiltonian. The electronic repulsion is expressed in terms of Racah parameters denoted by A, B and C. A does not appear in crystal field term, only B and C are present in CF term.

In transition-metal ions, Racah parameters are to be further reduced by fixing the ratio C/B to a value at around 4.5. When spin-orbit coupling is ignored, the energy levels calculated for d^n system will depend on the ligand field strength (Δ) and B [79, 82]. The results are presented in the form of Tanabe-Sugano diagrams by plotting the energies of the levels along the vertical axis in units of B against the ratio Δ/B. Tanabe-Sugano diagrams are used for the interpretation of spectra in a quantitative way. A Tanabe-Sugano diagram for the d^3 configuration in an octahedral field is shown

in Figure 6.9. The arrangements of d-electrons are different in various states such as ^4F and ^4P, and interelectronic repulsion is different in these states [82]. The solid and dotted lines show the level of spin-allowed and spin-forbidden transitions, respectively. The ruby lines R_1 and R_2 shown in Figure 2.4 are the first two spin-allowed transitions from ground state $^4A_2$ toward the $^4T_2$ and $^4T_1$.

6.2.4 Metal-insulator transition

The Electron correlation effect is the most fascinating and challenging subject in condensed matter physics. In solids with d- or f-electrons, the electron correlations are generally strong. In general, the correlation effect is large when two electrons with spin up and down occupy the same d-orbital of a transition-metal atom. The transition-metal oxides with partially filled d-electrons are poor conductor and indeed often insulator. This insulating behavior is due to strong coulomb repulsion between electrons, which prevents the electrons to move at all and this state is called Mott Insulator [78].

The metal-insulator transitions (MIT) are extensively studied in d-electron system. These MIT are actually derived by strong correlation effect associated with the electron-electron interaction and the interplay between charge, orbital and spin degrees of freedom. For non-interacting or weakly interacting systems the metal and insulating states are based on the filling of the electronic bands. For insulators the highest filled band is completely filled; for metals, it is partially filled. In other words, the Fermi level lies in a charge gap in insulators while the level is inside a band for metals.

A prototype of theoretical understanding for transition between the Mott insulator and metals is achieved by using single band Hubbard model, given below [78, 83],

$$H = H_t + H_U, \tag{6.3}$$

$$H_t = -t\Sigma_{\langle ij\rangle}(c^+_{i\sigma}c_{j\sigma}), \tag{6.4}$$

$$H_U = U\Sigma_i n_{i\uparrow}n_{i\downarrow}. \tag{6.5}$$

H_t is the kinetic energy term which expresses the quantum mechanical hopping of electrons in a conduction band. The operators $c^+_{i\sigma}$ and $c_{j\sigma}$ are standard fermionic creation and annihilation operators for an electron with spin s (either $\uparrow$ or $\downarrow$) at the site i and j, respectively. The second term H_U, considers the local Coulomb interaction U between the electrons. The operator $n_{i\sigma}{=}c^+{}_{i\sigma}\ c_{i\sigma}$ represents the occupation number of electrons with spin σ at the site i.

In this Hamiltonian every electron is considered to be in single orbit within a band without any electron-electron interaction. The simplifications are needed to describe

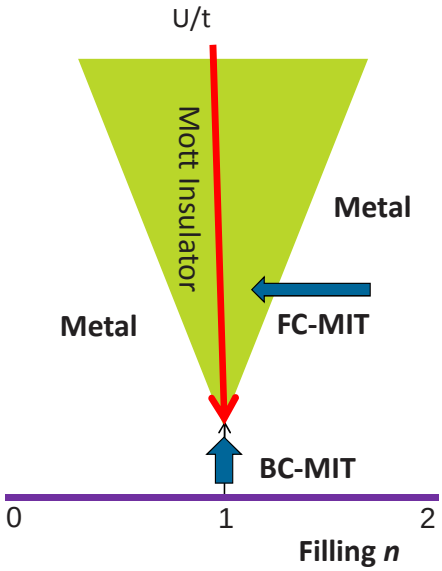

Figure 6.10: *Metal-insulator phase diagram based on the Hubbard model in the plane of the electron correlation strength U/t and filling n. Two routes for the metal-insulator transition (MIT) are shown: the FC-MIT filling-control MIT (FC-MIT) and the bandwidth-control MIT (BC-MIT). The figure is adopted from Ref [78].*

the *d*-electron system by this model. One has to assume that either the ligand *p*-orbitals are far from *d*-orbitals of the transition-metal or they are strongly hybridized and form a single band. A detailed description of this approach can be found in Ref [78].

There are two important parameters in the Hubbard model: the electron-correlation strength U/t and the band filling n. The schematic phase diagram in terms of these parameters is shown in Figure 6.10. The metal-insulator transition (MIT) occurs by varying the controllable parameters. Two routes for the MIT are the filling-control MIT (FC-MIT) and the bandwidth-control MIT (BC-MIT). The green shaded area is in principle metallic but under the strong influence of MIT. In this regime fluctuations of spin, charge, and orbital correlations are strong, the metallic phase with such strong fluctuations near the Mott insulator is called the anomalous metallic phase. In case of a nondegenerate band, i.e. with n=0 and n=2 fillings the system behave as a band insulator. The filling at noninteger n usually leads to the metallic phase. The interesting phase is the half-filled case(n=1), where the change of U/t drives the insulator-to-metal transition (Mott transition) at a critical value of U/t except in the case where the critical value U is zero. At a finite U a bandwidth control (BC)-MIT

occurs. In case of BC-MIT, the metallic state from the Mott insulator is obtained by increase the hopping integral t with the application of pressure, which reduces the relative strength of electron correlation. The on-site Coulombic interaction is almost unchanged during this process. The BC-MIT are observed in A(Zn, Mg)V_2O_4 presented in this chapter.

6.3 Classes of magnetic systems

There are various classes of magnetic materials despite the conventional magnets such as ferromagnets, antiferromagnets, and ferrimagnets, which possess different spatial dimensions, ranges, and signs of interactions and exhibit the anisotropy of the magnetic spin. The different ground states of the magnetic system are categorized with the perspective of frustration and disorder in the lattice, which are shown in Figure 6.11.

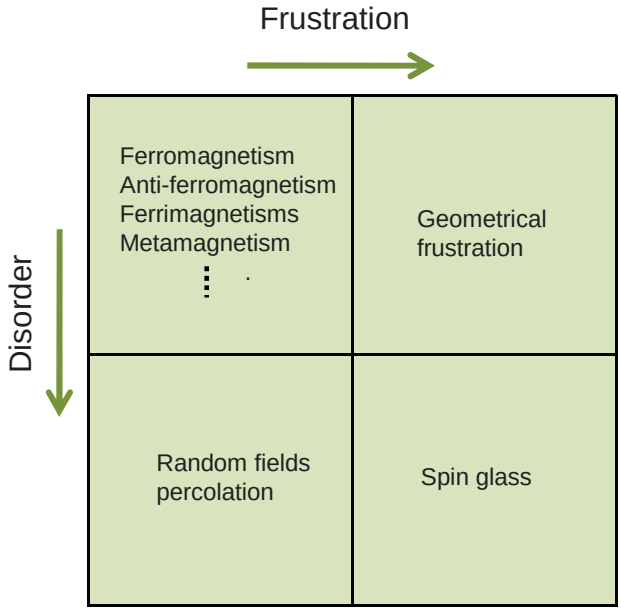

Figure 6.11: *The ground states of magnetic systems with perspective of frustration and disorder in the lattice. The figure is adopted from Ref [84].*

There is a natural interrelationship, if we treat the site disorder and frustration as independent parameters. The top left box in Figure 6.11 lists the well understood magnetic classes, which corresponds to both weak frustration and low disorder. The lower left box shows the phenomena of random field magnetism and percolation effects due to low frustration and high disorder in the lattice. The spin glass state exhibits high

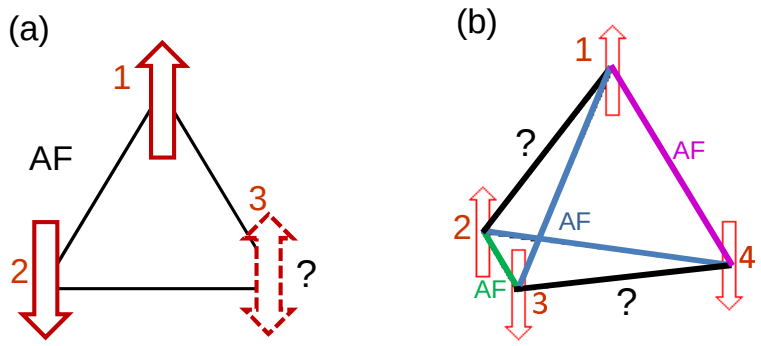

Figure 6.12: *Frustrated lattices: (a) Triangular lattice, where 3 magnetic ions reside on the corner of a triangle.(b)Tetragonal Lattice, with 4 magnetic ions on the corner of tetrahedron. The solid lies indicate the nearest neighbor interactions and interrogative marks show undefined orientation of electron spin and undefined interactions between spins which leads the system to frustration.*

frustration and high disorder. The upper right box represents geometrical frustrated systems that possess a high degree of frustration and little or no disorder among the spins [84].

Geometrical frustration is an important feature in magnetism, where it stems from the topological arrangement of spins. One example is a triangular arrangement of antiferromagnetically (AF) interacting spins as shown in Figure 6.12 (a), where the three magnetic ions reside on the corners of a triangle, the energy is minimized when each spin is aligned antiparallel to its neighbors. Once the first two spins align anti-parallel, the third one is frustrated because of its two possible orientations, up and down, giving the same energy. The third spin cannot simultaneously minimize its interactions with both of the other two. Thus the ground state is two-fold degenerate. Another example is a tetragonal arrangement of antiferromagnetically interacting spins (see Figure 6.12 (b)), where four magnetic ions reside on the corners of a tetrahedron. In this case it is not possible to arrange the electron´s spins in a way that all interactions between the spins are antiparallel. There are six nearest-neighbor interactions, of which four are antiparallel and thus favourable, but two of which (between 1 and 2, and between 3 and 4) are unfavourable. It is impossible to have all interactions favourable, which make the system frustrated.

The geometrically frustrated antiferromagnets display properties unlike other well

known types of magnets because of their degenerate ground states. Examples of frustrated lattices are shown in Figure 6.13. The Kagome and triangular lattices are two dimensional, their analogues in three dimensions are pyrochlore and face centered cubic (FCC), respectively. The physical properties of a system are different with different frustrated lattices as a structural unit. The investigated materials described in this chapter have a pyrochlore lattice and geometrical frustration plays an important role in their physical properties.

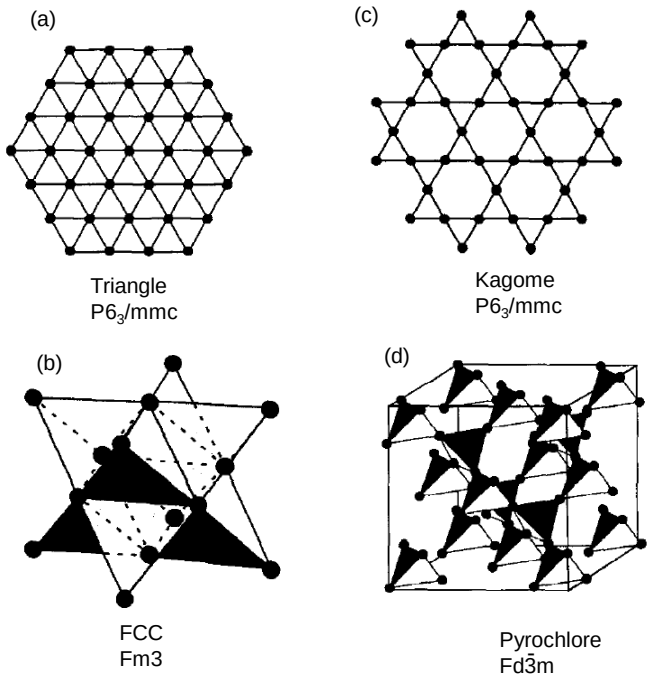

Figure 6.13: *Frustrated magnetic lattices with nearest neighbor AF interactions, (a) the triangle lattice with edge sharing triangles, (b) FCC lattice with edge sharing tetrahedra, (c) the kagome lattice with corner sharing triangles, and (d) the pyrochlore lattices with corner sharing tetrahedra. The associated space groups are given with their corresponding lattice. This figure is adopted from Ref [84].*

6.4 Chromium Spinels

Chromium spinels are the most extensively investigated among spinels family of materials. They belong to the frustrated magnetic class (geometrical and bond frustrated).

At low temperatures they show ferromagnetic and antiferromagnetic order. The investigated Cr-spinels compounds with formula ACr_2X_4 have A-site non magnetic divalent cation (Zn, Cd, or Hg) and B-site (Cr^{3+}) magnetic trivalent cation. The Cr^{3+} ions are octahedraly coordinated with various elements of group VI (i.e., O, S, and Se). The physical properties vary widely from oxides to chalcogenides (S and Se).

The Cr^{3+} ion is in the $3d^3$ configuration, its three 3d electrons occupy t_{2g} energy levels exhibiting high spin state with total spin S=3/2. In this case the orbital degree of freedom is frozen. The Cr-sublattice form a pyrochlore where spins are localized forming as a highly frustrated system.

Frustrated magnets are very sensitive to various types of perturbations which lift the degeneracy of the ground-state manifold. Depending on the size of the anions, ferromagnetic (FM) and antiferromagnetic (AFM) exchange compete. If the competing interactions are equal, they almost cancel each other and the situation is called a bond frustration revealing Curie-Weiss temperatures close to 0 K [85]. It is this coexistence of geometrical frustration and bond frustration which constitutes a variety of complex ground states as a function of Cr-Cr separation. The frustration is released by a spin-driven Jahn-Teller effect [86, 87] inducing lattice anomalies and strong symmetry breaking in the dynamic variables.

Oxides with spinel structure are geometrically frustrated, and this frustration often causes extensive degeneracy in the ground state of the system and prevent any ordering down to low temperatures. For example $CdCr_2O_4$ undergoes the AFM ordering only at 7.8 K [88,89]. Most of the oxide spinels are antiferromagnetic insulators with negative Curie-Weiss temperature, dominated by strong direct Cr-Cr exchange [85].

Most chalogenide Cr-spinels are simple Heisenberg ferromagnets [90] and hence are not expected to be geometrically frustrated. In $ZnCr_2Se_4$ the direct exchange is almost suppressed because of the increase of the Cr-Cr distance unlike in ACr_2O_4, and spin arrangements are dominating by 90° ferromagnetic Cr-Se-Cr exchange and Curie temperature of 115 K [91, 92]. Below temperature $T_N \approx 21$K, the spins order antiferromagnetically [93, 94].

In $HgCr_2S_4$ the FM exchange interactions are strong and dominating. $HgCr_2S_4$ shows ferromagnetic correlation with Curie-Weis temperature of ≈142 K, and it goes to antiferromagnetic order at 22 K [85]. This compound shows simultaneous occurance of the colossal magnetocapacitance and colossal magnetoresistance, and short-range ferroelectric order develops at low temperatures $T < 70$ K [95].

Often the magnetic transitions are accompanied by the structural distortion. In $ZnCr_2Se_4$, at T_N the spins order antiferromagnetically and the structure changes from cubic $Fd\bar{3}m$ to tetragonal $I4_1/amd$ symmetry, with a small contraction along the c axis

of c/a = 0.9999 [96]. The size of the splitting of phonon modes at the structural transitions has been attributed to spin-phonon coupling effect [93]. The recently found phenomena in magnetic spinels, e.g., heavy-fermion-like liquid states, spin-singlet states, composite spin degree of freedom, spin-orbital liquid and orbital glass states, as well as the colossal magneto-capacitive coupling in spinel multiferroics, bear the sign of the geometrical frustration that enhances the spin, orbital, and lattice fluctuations [90]. Since magnetic interactions depend on interatomic distances, one expect the structural anomalies at low temperatures and high pressures, which can be manifested in the phonon behavior.

6.4.1 Phonons in Cr-Spinels

The atoms in solids are bound to their equilibrium positions by the forces that hold the crystal together. When atoms are displaced from their equilibrium positions, they experience restoring forces, and vibrate at characteristic frequencies. These vibrational

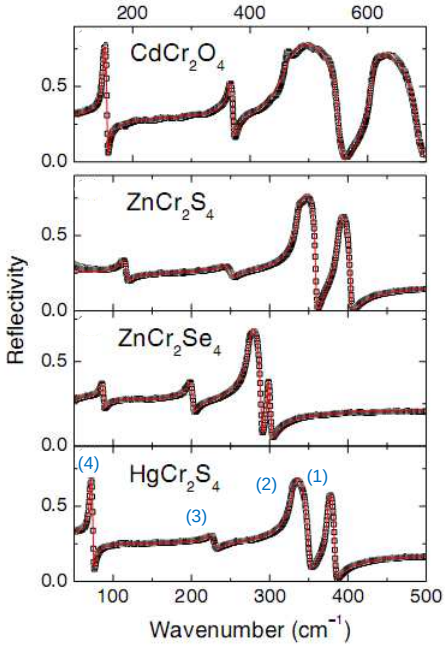

Figure 6.14: *The far-infrared reflectivity spectra of different Cr-spinels, showing four infrared active phonons, which are labelled as 1-4 starting from higher-frequency. The black squares represents the experimental data and red solid lines show the fitting. The figure is adopted from Ref [85] with small modification.*

frequencies are determined by the phonon modes of the crystal. The resonant frequencies of the phonons occur in the infrared (IR) spectral region. The detailed selection rules for deciding which phonon modes are IR active can be derived by using the group theory.

From the lattice symmetry of the normal spinels, the group theory analysis predicts four infrared active triply degenerated T_{1u} phonon modes in the FIR spectrum [97].

$$\Gamma = 4T_{1u} \qquad (\mathrm{IR-active}) \tag{6.6}$$

$$+A_{1g} + E_{1g} + 3T_{2g} \qquad (\mathrm{Raman-active}) \tag{6.7}$$

$$+2A_{2u} + 2E_u + T_{1g} + 2T_{2u} \qquad (\mathrm{silent}) \tag{6.8}$$

The four infrared-active phonon modes of various Cr-spinel compounds are shown in Figure 6.14. The phonon modes are named as *mode*1-4 starting from higher-frequency to lower-frequency. In Figure 6.14, the second phonon mode (*mode* 2) in all compounds is more intense compared to other modes. The phonons of the various pure

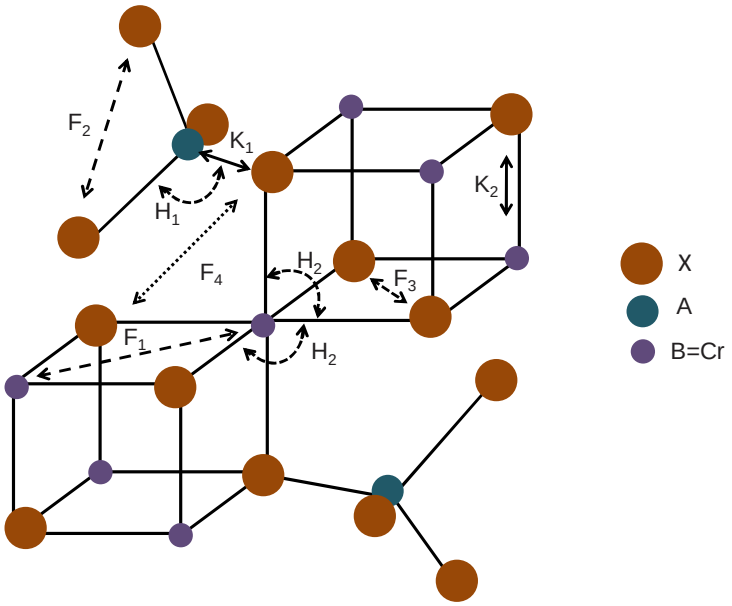

Figure 6.15: *The short range force constants K_i, F_i, and H_i of the AB_2X_4 spinel structure. The figure is adopted from Ref [98].*

and mixed spinels were studied comprehensively by Raman and infrared spectroscopy. However, the assignment of the origin of four infrared active phonon modes had been

Internal Coordinates	Force Constants
A-X	K_1
Cr-X	K_2
Cr-Cr	F_1
X-A-X	H_1
X-Cr-X	H_2
X-X (1)	F_2
X-X (2)	F_3
X-X (3)	F_4

Table 6.1: *Short range force constants illustrating the internal coordination of different atoms in the AB_2X_4 spinel structure [98].*

Phonon Modes (TO and LO)	Force Constants
$T_{1u}(1)$	K_2, F_1, C, F_3
$T_{1u}(2)$	K_2, C, H_2, K_1
$T_{1u}(3)$	F_1, F_2,F_3, K_1
$T_{1u}(4)$	K_1, F_3, K_2, F_2

Table 6.2: *Force constants contributing to IR active phonon modes [104].*

a subject of controversy. In literature, there are two different types of interpretation proposed for the origin of phonon modes. In Ref [99–101] two high frequency phonon modes are assigned to the displacement of the Cr-X bond in the CrX_6 octahedra and the two low-frequency phonon modes to the tetrahedra AX_4. It has been examined experimentally [56, 102, 103] that the materials, which have an octahedral sublattice in their structural unit, exhibit phonon modes belonging to octahedral vibrations at higher-frequencies compared to the other lattice vibrations.

Lutz and coworkers [98, 104–108] claimed that almost all atoms contribute to the four infrared active phonon modes and assigning few phonon modes to the tetrahedra and other to octahedra is wrong. They employed the short range model (SRM), the rigid-ion model (RIM) and the polarizable-ion model (PIM) for the lattice dynamical calculation to get the detailed information on bonding, structure, and dynamics of the spinel structure. The short range force constants of the spinel structure AB_2X_4 are defined in Table 6.1 and illustrated in Figure 6.15.

The infrared active vibrational modes of zone center phonons obtained for $MnCr_2S_4$ according to the PIM calculations are illustrated in Figure 6.16. Almost all the atoms contribute to all four vibrational modes except that the contribution of A-site atoms to the higher-frequency phonon modes (*mode*1,2) with $T_{1u}(1)$ and $T_{1u}(2)$ symmetry,

respectively is less compared to the other two phonon modes. The division of the phonons into the vibrations of tetrahedral AX_4 and the octahedral BX_6 or the cube B_4X_4 units of the structure is not possible [104]. However, one can say that for higher-frequency phonons the contribution of octahedron vibrations is higher compared to tetrahedron vibrations. The contributions of different atoms to the phonon modes are

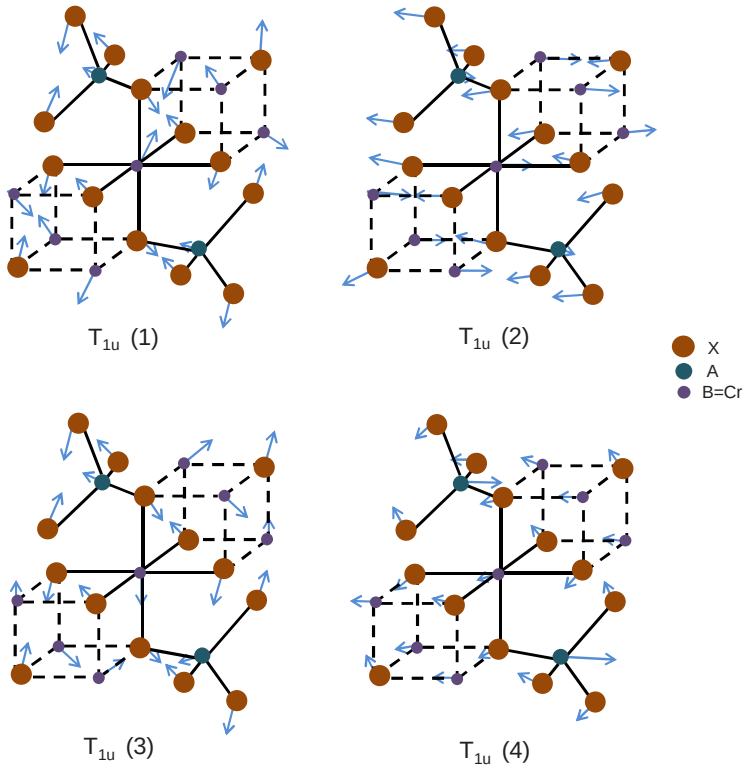

Figure 6.16: *Infrared active normal vibrational modes of zone center phonons of $MnCr_2S_4$ obtained by PIM calculations. It is assumed that the other Cr-spinels show similar vibrational modes. The figure is adopted from Ref [104].*

summarized in Table 6.2 in the form of short range force constants and long range force constant'C'. From the short range force constants it is clear that the potential of the spinel structure is mainly controlled by Cr-X(K_2 octahedron) and A-X (K_1 tetrahedron) stretching as well as by X-X (F_2-F_4) and Cr-Cr (F_1) repulsive forces where the bending forces (H_1, H_2) can be neglected. The$X$-X forces are important for all modes except $T_{1u}(2)$, and Cr-Cr interactions are predominant for $T_{1u}(3)$ and $T_{1u}(1)$. It is assumed that the vibrational modes of other Cr-spinels should be similar.

6.4.2 Crystal-field excitations in Cr-Spinels

The Cr^{3+} ion in octahedral environment exhibits three spin allowed crystal-field transitions, namely the intra-atomic*d*-*d*-transitions. These spin-allowed transitions are from the ground state $^4A_{2g}$ to the $^4T_{2g}(^4F)$, $^4T_{1g}(^4F)$ and $^4T_{1g}(^4P)$(see Figure 6.9). The transition from the ground state to $^4T_{2g}(^4F)$ is located at 10 Dq = Δ_{oct}, where Dq is the coulombic parameter of the ligand field [79]. The value of Δ_{oct} depends on the following factors;
(i) The nature of the transition-metal ion.
(ii) The metal's oxidation state. A higher oxidation state leads to a larger splitting.
(iii) The arrangement of the ligands around the metal ion.
(iv) The nature of the ligands surrounding the metal ion. The stronger the effect of the ligands, the greater the value of Δ_{oct} will be.
Usually, the CF excitations are parity-forbidden, because of inversion symmetry at transition-metal ion site. These transitions become allowed by virtue of lattice vibrations which locally break the center of symmetry. The matrix element for a *d*-*d*-transition induced by a photon is [109],

$$\langle \psi_{final} \left| p \right| \psi_{initial} \rangle \,, \tag{6.9}$$

where p is the dipole operator with odd parity and the parity of a 3d electron wave function is even. In case of inversion symmetry (see Figure 6.17 (a)), the above matrix element vanishes.

$$\langle even \left| odd \right| even \rangle = 0. \tag{6.10}$$

The symmetry breaks at transition-metal site due to an odd-symmetry phonon which is excited simultaneously with the orbital excitation, this will give a small amount of odd character to the 3d wave function (see Figure 6.17 (b)) [109]. Because of mixed states (odd and even) the *d*-*d* excitation are observed in the spectrum. The spin selection rule is (ΔS=0), the transition between states with identical spin quantum number are allowed, i.e, the transitions from spin states singlet$\longrightarrow$singlet, doublet$\longrightarrow$doublet and triplet$\longrightarrow$triplet, etc are allowed. The transition from different spin states will be forbidden

The observed CF excitations for investigated Cr-spinel compounds are shown in Figure 6.18. In reflectivity measurements of free-standing sample of $ZnCr_2Se_4$ and $HgCr_2S_4$, the E1 band was observed at around 15000-15500 cm^{-1}. The small peak at around 13000 cm^{-1} marked with arrow in optical conductivity spectrum of $HgCr_2S_4$ is probably spin-forbidden transition. The center of gravity of these excitations are marked with arrow in real part of optical conductivity spectra, obtained from fitting. In case of $CdCr_2O_4$ the CF excitations were weak in reflectivity spectrum and were more

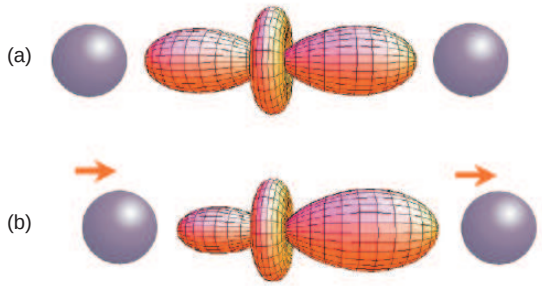

Figure 6.17: *(a) The $3d_{z^2r^2}$ orbital of a transition-metal ion is in between two negatively charged ligands. (b) The inversion symmetry on the transition-metal site breaks by exciting a bond-stretching phonon. The sketch indicates an increased electron density on the right side, where the distance to the negatively charged ligand has increased. The figure is adopted from Ref [109].*

clear in absorption measurements. The absorbance spectrum of $CdCr_2O_4$ at lowest measured pressure 1.0 GPa is shown in Figure 6.18 b. The CF excitation (10Dq) is at 16760 cm^{-1}. The weak excitations marked with arrow are spin forbidden transitions, which become allowed due to spin orbit coupling [110].

6.5 Investigated Cr-spinel compounds

The single crystals of Cr-spinels: $ZnCr_2Se_4$ and $HgCr_2S_4$ were grown by chemical transport reactions [85, 100], and $CdCr_2O_4$ were grown by a flux method. These materials have been investigated by infrared spectroscopy under pressure in the frequency range 200-24000 cm^{-1}. Far-infrared (FIR) reflectivity measurements were carried out at beamline IR1 of ANKA synchrotron source Karlsruhe. The CsI was used as a pressure transmitting medium in all infrared measurements.

Analysis Procedure

For analysis of the reflectivity data, the region around 2000 cm^{-1} is cut out from the data, since the diamond multiphonon absorption causes artifacts in this range. The data in this frequency range was linearly interpolated. For fitting the infrared data, the Lorentz model (given in Chapter 2) was used. The pressure-dependence of the high-frequency permittivity ϵ_∞ used for fitting the reflectivity data, was calculated according to the Clausius Mossotti relation [63]. The unit cell volume as a function of pressure was calculated from the first-order Birch equation of state [64, 65], explained

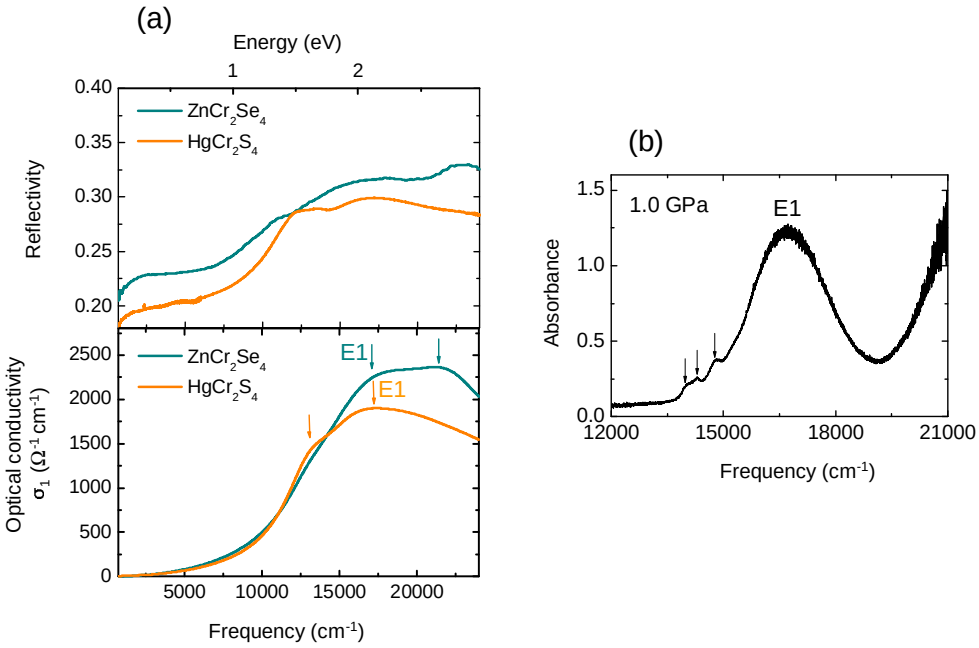

Figure 6.18: *Crystal-field excitations of Cr^{3+} ion in octahedral environment (a) for $ZnCr_2Se_4$ and for $HgCr_2S_4$. In lower panel of (a), the arrow at low-frequency side for $ZnCr_2Se_4$ shows the first CF excitation E1 (10Dq). In case of $HgCr_2S_4$, the arrow at high-frequency side is E1, while the low-frequency side arrow indicates the spin-forbidden transition. (b) The absorbance spectrum of $CdCr_2O_4$ at 1.0 GPa showing E1 band and three spin forbidden transition at low-frequency side, marked with arrows.*

in Chapter 5. The pressure-dependence of ϵ_∞ and unit cell volume are illustrated in Figure 6.19. The value of the bulk modulus was assumed to be B_0=100 GPa and B_0=200 GPa for chalcogenides ($ZnCr_2Se_4$ and $HgCr_2S_4$) and for oxides ($CdCr_2O_4$), respectively, based on XRD study [111]. The value of ϵ_∞ is also frequency dependent. For $ZnCr_2Se_4$ and $HgCr_2S_4$ the value of ϵ_∞=2 was determined up to 100000 cm^{-1} (using extrapolation), and ϵ_∞= 8 up to 700 cm^{-1}. In case of $CdCr_2O_4$ ϵ_∞=3 was obtained up to 100000 cm^{-1} and ϵ_∞=6 up to 1000 cm^{-1}.

6.5.1 Results and analysis of $ZnCr_2Se_4$

The reflectivity (R_{s-d}) spectra of $ZnCr_2Se_4$ along with the fit, for few selected pressures in the frequency range 250-24000 cm^{-1} are shown in Figure 6.20. The overall reflectivity of the sample in the diamond anvil cell is lower as compared to the free-standing

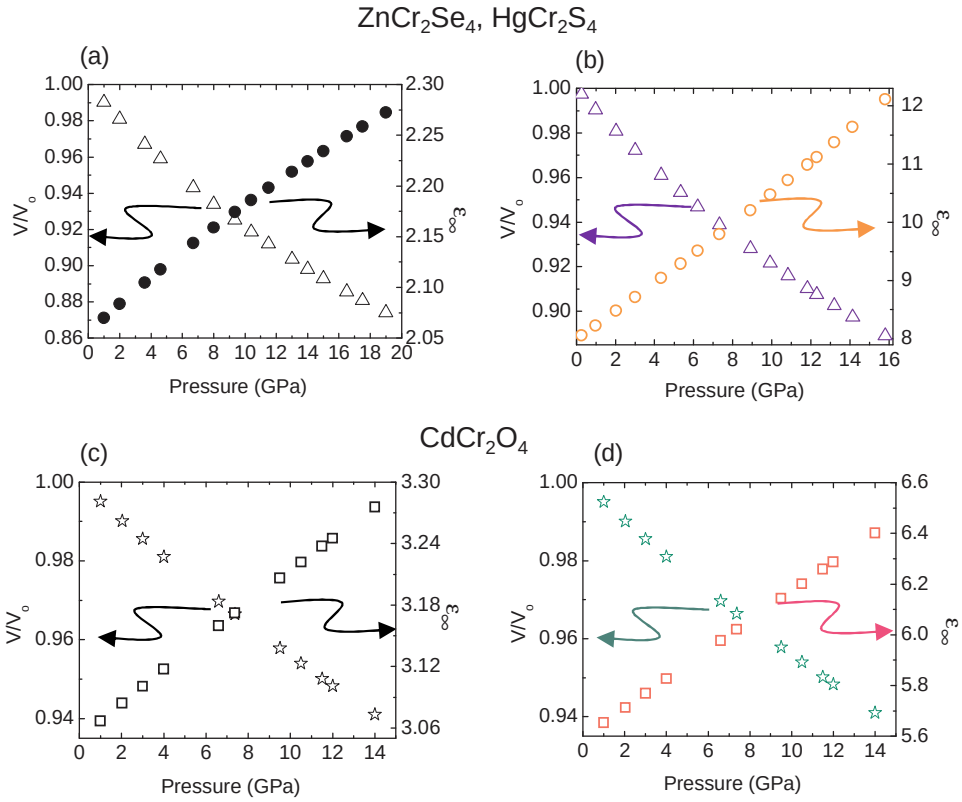

Figure 6.19: *Pressure-dependence of the unit cell volume and ϵ_∞ of $ZnCr_2Se_4$ and $HgCr_2S_4$ (a-b), and for $CdCr_2O_4$ (c-d) . The unit cell volume was calculated according to the first order Birch equation of state (Eq. (5.2)) and the high-frequency permittivity ϵ_∞ was calculated according to the Clausius-Mossotti relation (Eq. (5.1)).*

sample [93] due to the smaller refractive index step at the sample-diamond interface. The measured reflectivity spectra in the FIR frequency-range for few selected pressures are shown in Figure 6.21. The spectra are offset along the vertical axis for clarity. The pressure-dependent reflectivity spectra in the spectral range 2500-24000 cm^{-1} up to 19 GPa are shown as an inset of Figure 6.20, which clearly shows the increase of reflectivity with increasing pressure. The fits obtained from the Lorentz model were used for extrapolation at the lower and higher frequencies of experimental data, which is necessary for the KK analysis to calculate the real part of optical conductivity. The KK relation used for the reflectivity R_{s-d} phase is already described in Chapter 2 and it is recalled here:

$$\phi(\omega_0) = -\frac{\omega_0}{\pi} P \int_0^{+\inf} \frac{\ln R_{s-d}(\omega)}{\omega^2 - \omega_0^2} d\omega + \left[\pi - 2\arctan\frac{\omega_\beta}{\omega_0}\right] \tag{6.11}$$

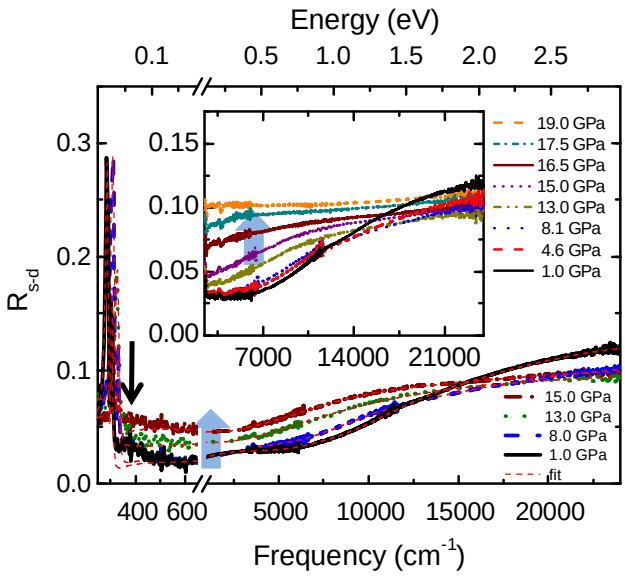

Figure 6.20: *Room-temperature R_{s-d} spectra of $ZnCr_2Se_4$ for few selected pressures. The red dashed lines are fits with the Lorentz model. In a lower pressure range, the small feature at around 400 cm^{-1}, marked with arrow is an artifact and excluded in fitting procedure. Inset: Pressure-dependent reflectivity spectra in the spectral range 2500-24000 cm^{-1}.*

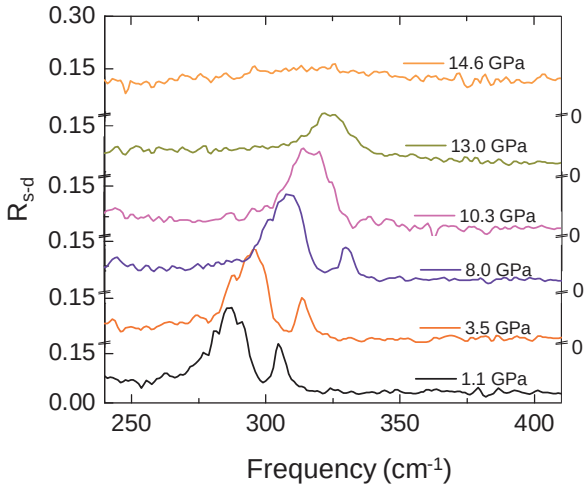

Figure 6.21: *Room-temperature reflectivity R_{s-d} spectra of $ZnCr_2Se_4$ in FIR frequency region, showing two phonon modes. The spectra are offset along the vertical axis for clarity.*

where ω_β is the position of the reflectivity pole on the imaginary axis in the complex

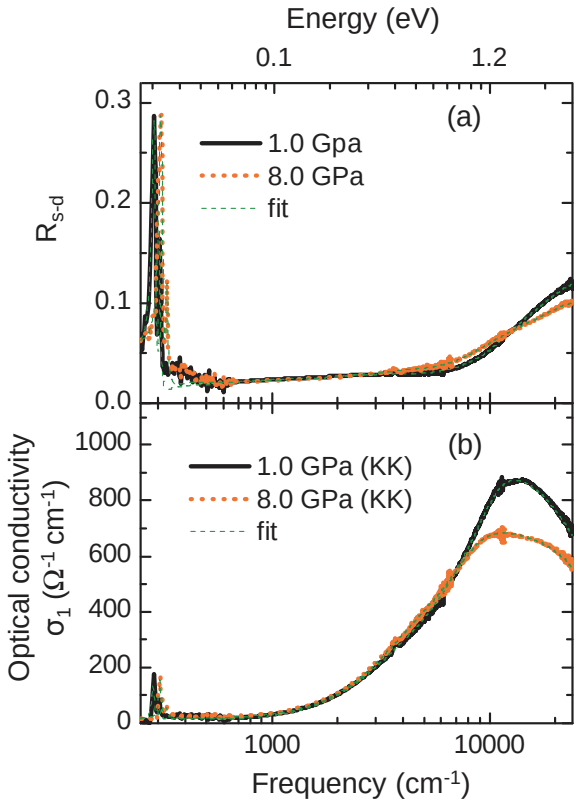

Figure 6.22: *(a) The measured reflectivity R_{s-d} of $ZnCr_2Se_4$ along with the Lorentz fits. (b) The corresponding optical conductivity $\sigma_1(\omega)$ spectra obtained from the fit (green colour dashed lines) compared with those obtained by the KK analysis.*

frequency plane. The criterium for the proper value of ω_β is the agreement between the optical conductivity obtained by the KK analysis and that from the initial fit. The output of the KK analysis is achieved for the parameter ω_β=9000-4200 cm^{-1} in the pressure range 1.0-19.0 GPa, respectively. A comparison of these two spectra, for two selected pressure (1.0 and 8.0 GPa) is given in Figure 6.22, which shows a good agreement between the spectra. This agreement holds for the optical conductivity spectra obtained in the whole range of applied pressures.

To extract the phonon parameters, the optical conductivity data in the FIR frequency region was fitted with the Lorentz model. The results are shown in Figure 6.23. The phonon modes harden with increasing pressure. There is no significant change in damping and oscillator strength of both phonon modes up to P $\approx$ 10 GPa, above 10 GPa, the high-frequency phonon mode (*mode* 1) is no longer visible (see Figure 6.21

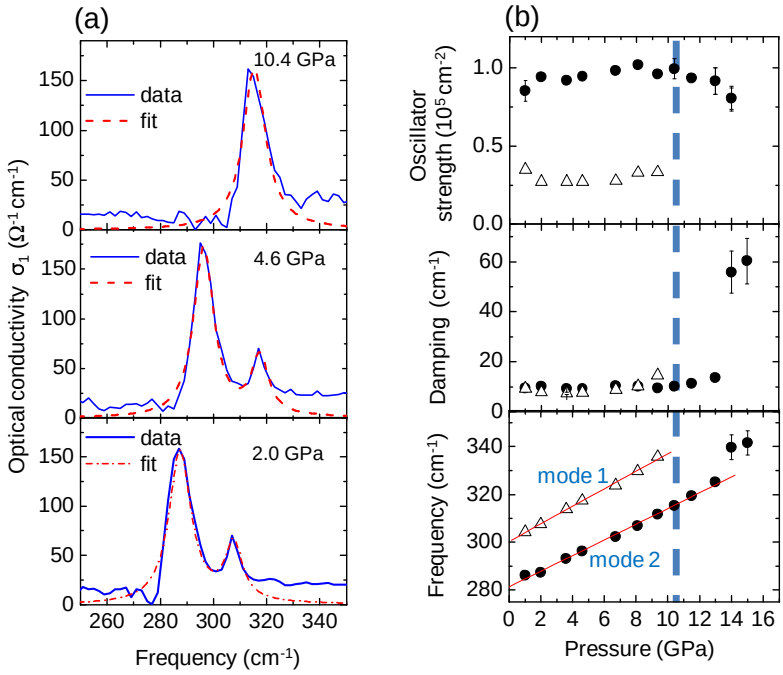

Figure 6.23: *(a)Illustration of the Lorentz fits of the real part (σ_1) of the optical conductivity of $ZnCr_2Se_4$ for three selected pressures 2.0, 4.6, and 10.4 GPa in the FIR refquency range. (b) The oscillator parameters obtained from the fit of the optical phonons are: frequency, damping, and oscillator strength. The red color solid lines show the fits of the phonon frequencies according to Equation 6.12. the dashed vertical line indicate the transition pressure.*

and Figure 6.23 (b)). By further increasing the pressure, the remaining low-frequency phonon (*mode* 2) starts to lose its strength and becomes damped. At 14 GPa no phonon resonance can be clearly resolved. To determine the pressure coefficient for two observed phonons, the frequency of phonon as a function of pressure was fitted with the following equation:

$$\omega(P) = \omega_o + A \times P, \tag{6.12}$$

where P is the applied pressure, ω_o is the phonon frequency at zero pressure and A is the pressure coefficient. For the high-frequency phonon mode (*mode* 1), the value of A is 3.68±0.1 cm^{-1}/GPa, which is somewhat higher than the value of A=3.28±0.07 for low-frequency phonon mode (*mode* 2), which indicates that the bondings belong *mode* 2 are stronger than that of *mode* 1.

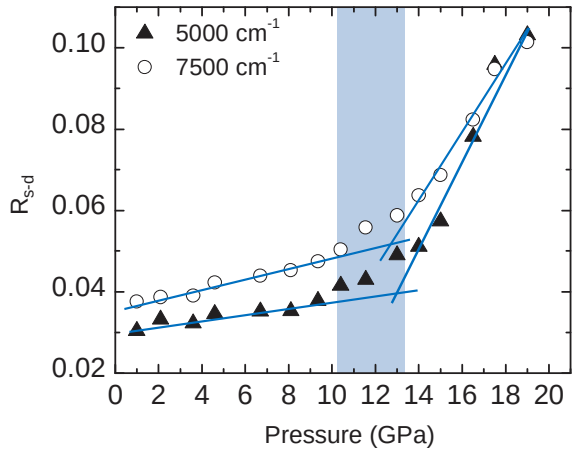

Figure 6.24: *The change in reflectivity (R_{s-d}) level of measured spectra of $ZnCr_2Se_4$ at 5000 cm^{-1} and 7500 cm^{-1} with the increase of pressure. The blue solid lines are guide to eye to see the transition pressure region, and blue colour vertical bar indicates that pressure region.*

There is anomalous change in the phonon parameters at around 10 GPa indicating a pressure-induced phase transition (see Figure 6.23 (b)). The transition pressure (P_c) (see Figure 6.24) is also confirmed by plotting the change in the reflectivity spectra as a function of pressure at two different energies at 5000 cm^{-1} and 7500 cm^{-1}, since, the reflectivity in this frequency range characterizes electronic response of the system. The reflectivity versus pressure curve shows that there is a continuous increase in R_{s-d} with increasing pressure up to 10 GPa. By further increasing pressure there is drastic increase in R_{s-d} indicating that the new structural phase is more susceptible to external pressure.

The Cr^{3+} ion in octahedral environment exhibit three crystal-field transitions namely the intra-atomic *d-d*-transitions. These transitions occur in a specific energy range. The transition from ground state to $^4T_{2g}$ is located at 10 Dq(Δ_{oct}), where Dq is the coulombic parameter of the ligand field. The *d-d* transition at 10Dq is named as E1. To discuss the high energy excitations, the reflectivity spectra were converted into a real part of the optical conductivity. In the conductivity spectra, at 1.0 GPa, the E1 absorption band at 15000 cm^{-1} reaching a maximum of 830 $\Omega^{-1}cm^{-1}$ (see Figure 6.25, becomes broader and gradually shifts toward the low-frequency region by increasing pressure. Rudolf et al. [93] observed the two CF excitations (intra-atomic *d-d* transitions) in reflectivity measurements of $ZnCr_2Se_4$ at 18000 cm^{-1} and 22000 cm^{-1}, which show red shift by lowering the temperature. The behavior of E1 band

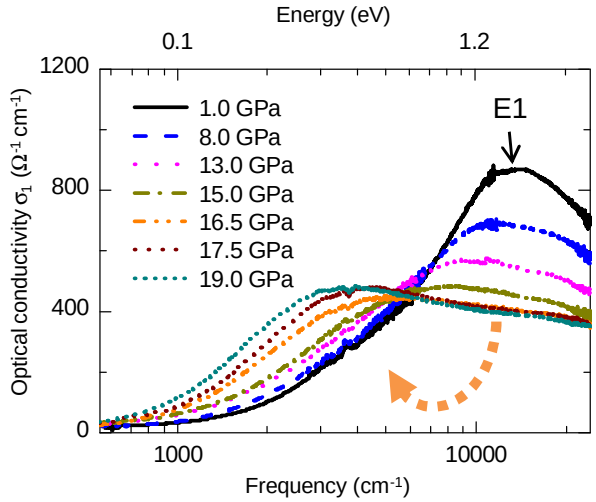

Figure 6.25: *Real part of the optical conductivity of $ZnCr_2Se_4$ for few selected pressures obtained from Kramers Kronig relation. The dotted arrow indicates the shift of spectral weight with increasing pressure.*

under pressure is in agreement with its temperature-dependent behavior.

6.5.2 Results and analysis of $HgCr_2S_4$

In Figure 6.26, the measured reflectivity spectra of $HgCr_2S_4$ for few selected pressures in the frequency range 250-24000 cm^{-1} are presented. The reflectivity level grows with increasing pressure in mid infrared frequency range. To see the pressure effect on the phonon modes the reflectivity spectra in the frequency range 250-500 cm^{-1} are plotted in Figure 6.27. The spectra are offset along vertical axis for clarity sake.

The phonon parameters are extracted by fitting the reflectivity data in the FIR frequency region with the Lorentz model. Since, the value of ϵ_∞ is frequency dependent. The reflectivity data up to 700 cm^{-1} at ambient condition was fitted and the ϵ_∞=8 was obtained, which is similar to the values found for $ZnCr_2Se_4$ up to 5000 cm^{-1} [93]. The pressure dependence of ϵ_∞ and the unit cell volume as a function of pressure are illustrated in Figure 6.19 (b).

The results of the fitting of the phonon modes are shown in Figure 6.28. The two observed phonon modes harden with increasing pressure up to 12 GPa. Above 12 GPa the *mode* 1 is not visible any more, and the *mode* 2 softens with increasing pressure. There is no significant change in oscillator strengths of *mode* 1 but it starts to become damped at around 8 GPa, and furthere pressure application increases the

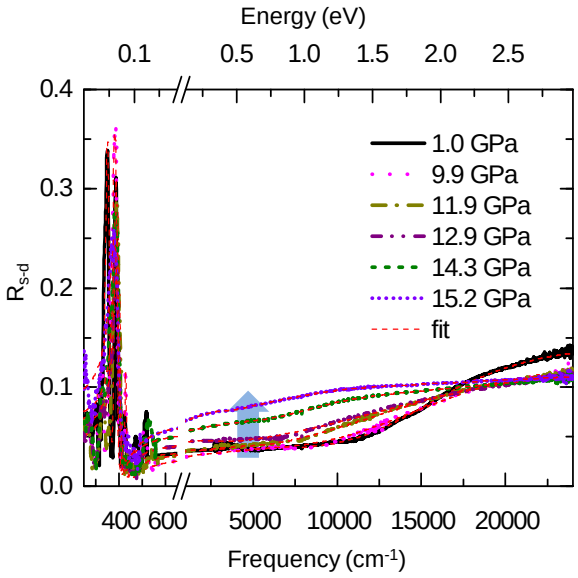

Figure 6.26: *Room-temperature R_{s-d} spectra of $HgCr_2S_4$ for few selected pressures. The red dashed lines show fits with the Lorentz model.*

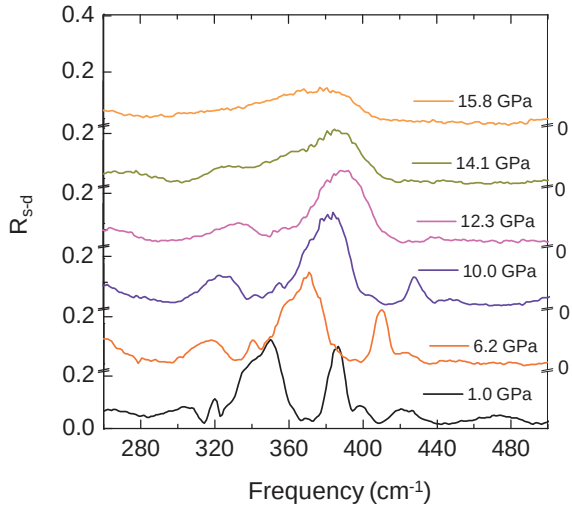

Figure 6.27: *Room-temperature R_{s-d} spectra of $HgCr_2S_4$ in the FIR frequency region showing two observed phonon modes. The spectra are offset along the vertical axis for clarity.*

damping, that it disappear above 12 GPa (see Figure 6.28). The *mode* 2 behaves differently under pressure, there is a continuous increase in oscillator strength, and abrupt enhancement in damping above 11 GPa is observed. One sees anomalous changes in phonon parameters at around 12 GPa (see Figure 6.28 (b)).

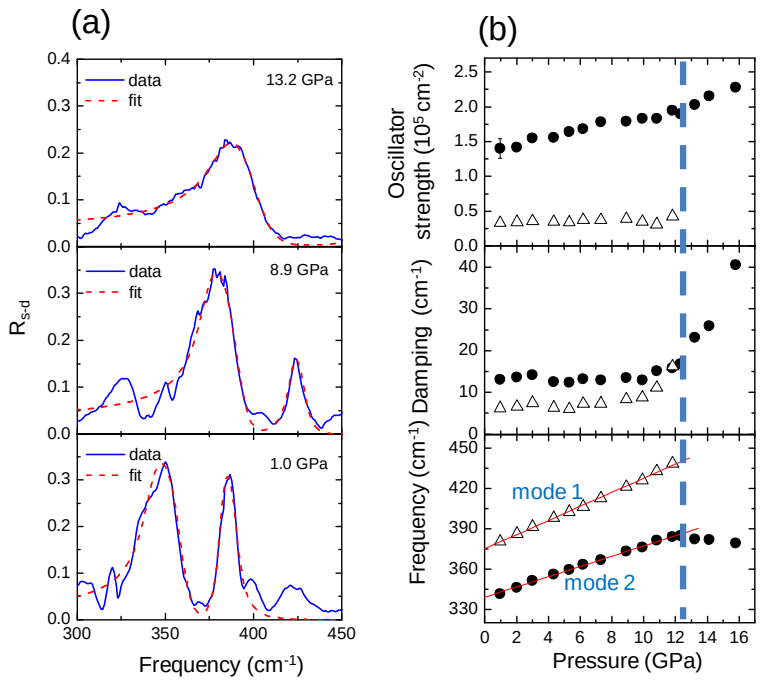

Figure 6.28: *(a)Illustration of the Lorentz fits of the R_{s-d} of $HgCr_2S_4$ for three selected pressures 1.0, 8.9, and 13.2 GPa in FIR frequency range. (b) The oscillator parameters obtained from the fit of the optical phonons are: frequency, damping, and oscillator strength. The red color solid lines show the fits according to Equation 6.12. the vertical dotted line indicates the transition pressure.*

The transition pressure (P_c) is also confirmed by plotting the change in the reflectivity level of measured spectra as a function of pressure at two different energies (5000 cm^{-1} and 7500 cm^{-1}), where the system show electronic response (see Figure 6.29). The significant change in the reflectivity versus pressure curve at around 12 GPa is observed. The anomalous increase of the infrared reflectivity and the anomaly in the phonon parameters at around 12 GPa are interpreted as a structural phase transition from cubic to tetragonal symmetry, which is discussed in later section

The frequencies of phonon modes as a function of pressure were fitted according to Equation 6.12 to determine the pressure coefficient (A) for two observed phonons. The value of A=5.25±0.08 cm^{-1}/GPa for *mode* 1 is comparatively higher than that of *mode* 2 , which is A=3.80±0.06 cm^{-1}/GPa. The value of A tells about the strength of the bonding of respective mode, higher the value of A, stiffer the bonding belonging to that mode is. In this compound *mode* 2 is less compressible because the bonds belong

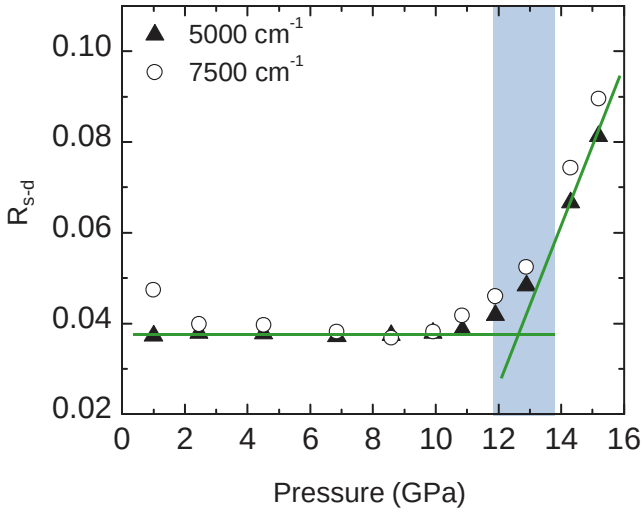

Figure 6.29: *The change in reflectivity R_{s-d} of $HgCr_2S_4$ with the increase of pressure at 5000 cm^{-1} and 7500 cm^{-1} shown with solid triangles and open circles, respectively. The green colour solid lines are guide to eye to follow the P_c.*

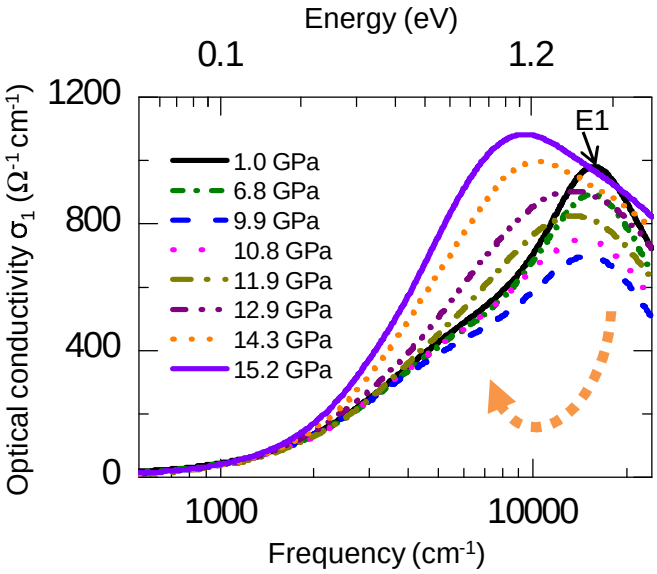

Figure 6.30: *Real part of the optical conductivity of $HgCr_2S_4$ for few selected pressures, obtained from fit curves of room temperature R_{s-d} data.*

to it are rigid compared to the bonds of *mode* 1.

The red shift of the phonon frequencies of $HgCr_2S_4$ was observed with lowering the temperature [85] and assigned to ferromagnetic interactions which are dominating in

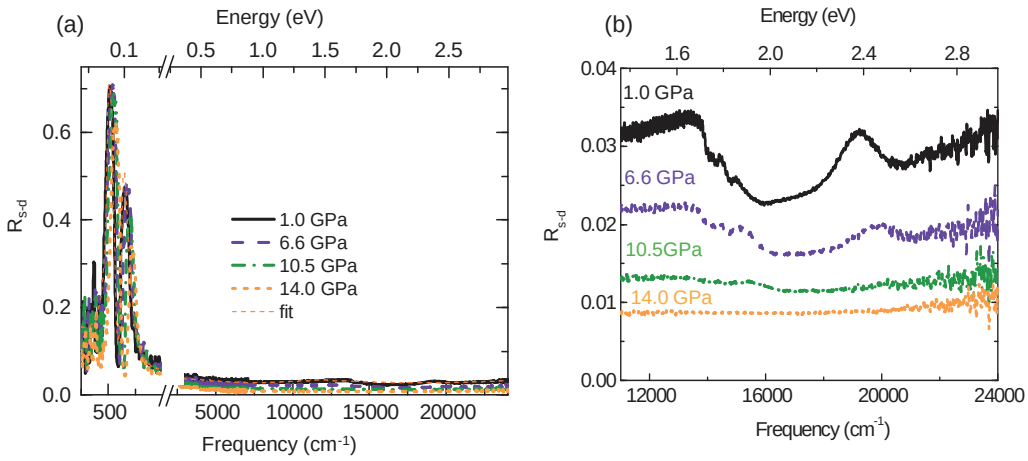

Figure 6.31: *(a)Room-temperature R_{s-d} spectra of $CdCr_2O_4$ for few selected pressures (1.0, 6.6, 10.5, 14.0 GPa). The red dashed lines are fits with the Lorentz model. (b)Magnification of (a) in the spectral range 10000-24000 cm^{-1}.*

this compound. In our data the softening of the *mode* 2 above 12 GPa is assigned to the FM behavior of the bonds, which are actively involved in that specific IR active mode.

The real part of the optical conductivity calculated from the fit is shown in Figure 6.30. At higher frequency the electronic transition are observed in optical conductivity spectra. The absorption band E1 observed at lowest measured pressure (1.0 GPa) with center of gravity at 15800 cm^{-1}, interpreted as an intra-atomic *d-d* transitions becomes broader and gradually shifts towards the low-frequency region with increasing pressure.

6.5.3 Results and analysis of $CdCr_2O_4$

Reflectivity measurements

The measured reflectivity (R_{s-d}) spectra of $CdCr_2O_4$ for few selected pressures in the frequency range 250-24000 cm^{-1} are shown in Figure 6.31 (a). The magnifying part of the reflectivity spectra in the spectral range 10000-24000 cm^{-1} show the electronic excitations (see Figure 6.31 (b)). These excitations are more pronounced in transmission spectra presented in later sections.

The measured reflectivity spectra R_{s-d} in the FIR frequency-range are shown in Figure 6.32. To get the information about pressure-dependence of phonon modes, the reflectivity spectra were fitted with Lorentz model. The illustration of the fits for

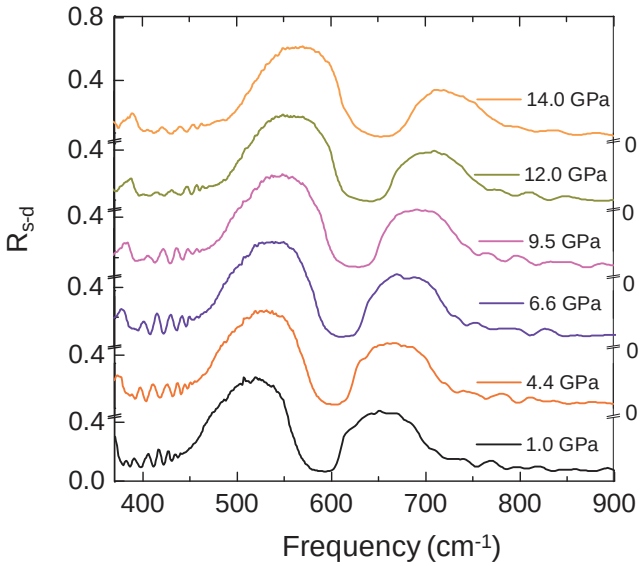

Figure 6.32: *Room-temperature reflectivity R_{s-d} spectra of $CdCr_2O_4$ in FIR frequency region, showing two observed phonon modes. The spectra are offset along the vertical axis for clarity.*

three selected pressures, and obtained results from the fitting of optical phonon modes are presented in Figure 6.33 (a) and (b), respectively. The phonon modes harden with increasing pressure and there is no notable change in oscillator strengths of both *mode* 1 and *mode* 2 up to highest measured pressure (P $\approx$ 14 GPa) (see Figure 6.33). The *mode* 1 becomes damped upon pressure application, but *mode* 2 stays intense up to P $\approx$ 14 GPa.

The linear pressure coefficient (A) for two phonon modes was calculated by fitting the frequencies of the phonons according to Equation 6.12. For *mode* 1, A=5.41$\pm$0.25 cm^{-1}/GPa and for *mode* 2, A=3.75$\pm$0.17 cm^{-1}/GPa. The small value of A for *mode* 2 indicates that the bonding of *mode* 2 is stiffer compared to *mode* 1, therefore it is less compressible.

The pressure-dependent optical conductivity spectra obtained by KK analysis show no significant change in all frequency and pressure ranges, as shown in Figure 6.34. For all studied pressures the best correspondence between the optical conductivity spectra obtained by fitting and the output of the KK analysis is achieved for the parameter ω_β=2800 cm^{-1}.

To clearly see the effect of pressure on the high frequency excitation transmission measurements were carried out on a single crystal of $CdCr_2O_4$.

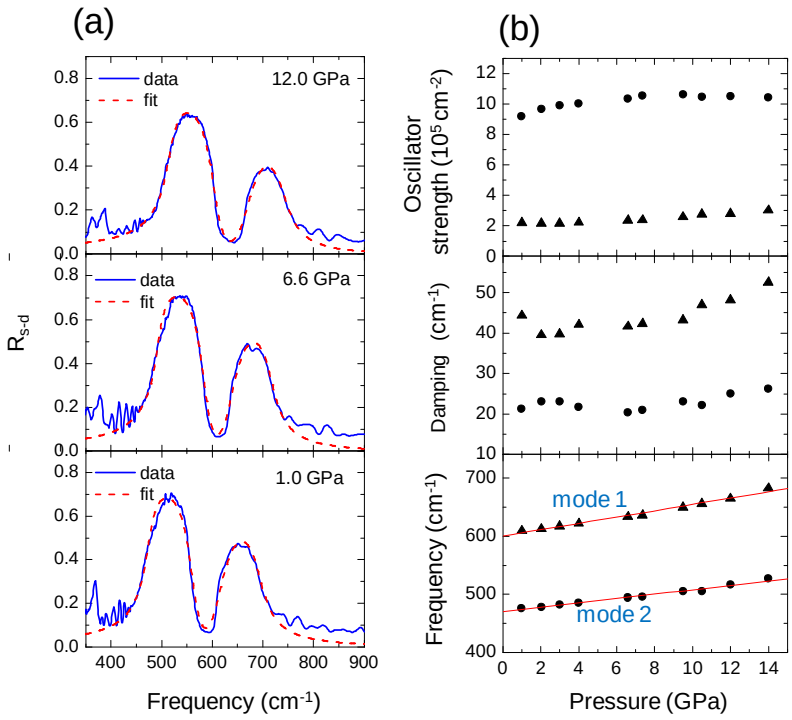

Figure 6.33: *(a) Illustration of the Lorentz fits of R_{s-d} of $CdCr_2O_4$ for three selected pressures 1.0, 6.6, and 12 GPa in FIR frequency range. (b) The phonon parameters obtained from the fit of the optical phonons are: frequency, damping, and oscillator strength. The red color solid lines show the fits according to equation (6.12)*

Transmission measurements

The pressure-dependent transmission measurements were performed on single crystals of $CdCr_2O_4$ up to 20.2 GPa in the frequency range 8000-25000 cm^{-1}. The transmittance and absorbance spectra for few selected pressures in the measured frequency range are shown in Figure 6.35. In order to determine the energy of optical transitions as a function of pressure, the fit of the absorbance spectra was done by using the Lorentz model. For absorbance spectrum at 1.1 GPa, the four absorption features contribute to it. The strong absorption band at ≈16760 cm^{-1} is first spin allowed CF excitation (E1) (see Figure 6.36 (a)), at low-frequency side three weak absorption features marked with arrows are spin forbidden transitions and their frequency positions are 14784 cm^{-1}, 14271 cm^{-1}, and 14036 cm^{-1} at 1.1 GPa.

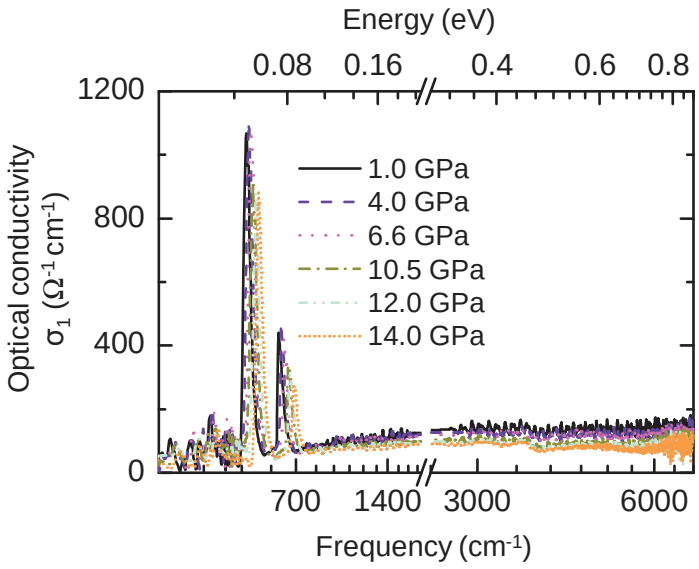

Figure 6.34: *Real part of the optical conductivity of $CdCr_2O_4$ for selected pressures.*

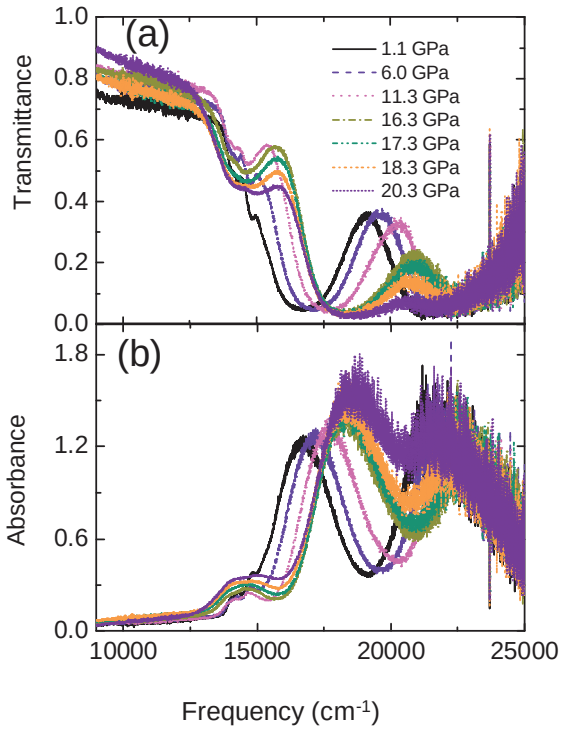

Figure 6.35: *(a) Transmittance and (b) absorbance spectra of $CdCr_2O_4$ for few selected pressures.*

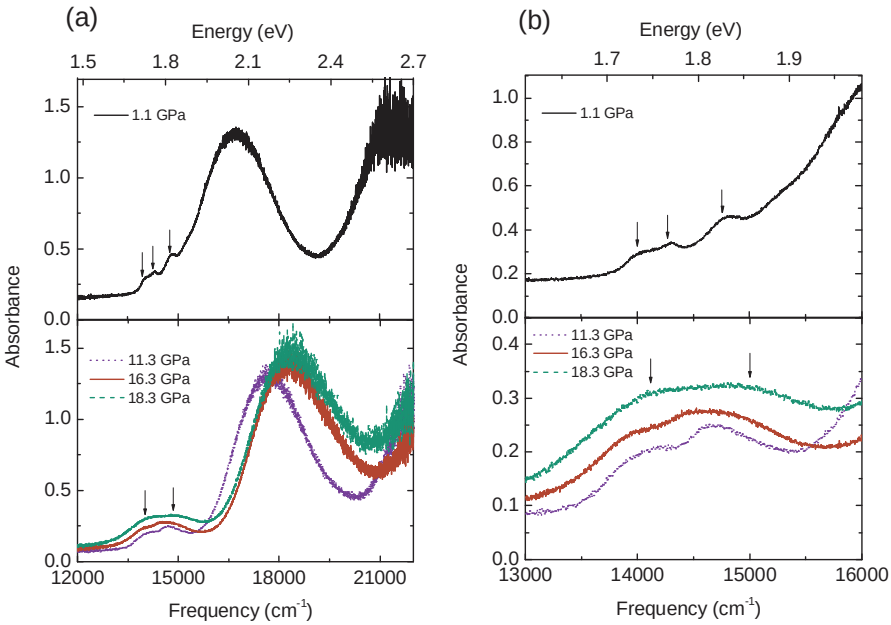

Figure 6.36: *(a) Absorbance spectrum of $CdCr_2O_4$ at 1.1 GPa shows four features: one strong feature at ≈ 16760 cm^{-1}, and three week features marked with black arrows, which are spin forbidden transitions. At higher pressures (11.3, 16.3 and 18.3 GPa) the low-energy absorption features marked with black arrows are not distinguishable any more. (b) The magnification of the low-energy part of the spectra in (a), to clearly show the spin forbidden transitions.*

The onset of second spin allowed CF excitation (E2) is seen, but its position can not be marked easily because spectra are noisy in this frequency range (see Figure 6.35).

With increasing pressure E1 band shows a blue shift, and the spin-forbidden transitions do not show significant shift in frequency position with increasing pressure up to ≈ 15 GPa, as shown in Figure 6.37 (b). Above 8 GPa, the spin forbidden transitions marked with arrow at 1.1 GPa are not distinguishable any more, and spectra could be fitted with only two Lorentzians (see Figure 6.37). These two spin-forbidden transitions are not clearly resolved at higest pressures (see Figure 6.36 (b)). The error in frequency positions is more at higher pressures as compared to the lower pressures. Above 15 GPa the pronounced blue shift of the higest-frequency spin-forbidden transition is observed, as shown in Figure 6.37 (b).

Qualitatively, the absorbance spectra can be compared with optical conductivity spectra of the system. The spectral weight of electronic excitations were calculated

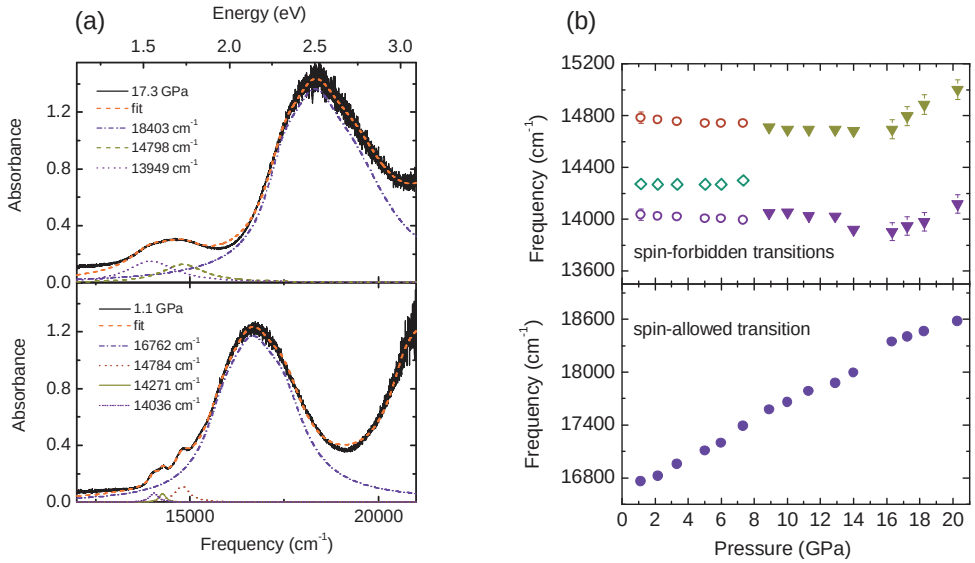

Figure 6.37: *(a) Fit of the two absorption spectra of $CdCr_2O_4$ at 1.1 GPa and 17.3 GPa consisting of four and three absorption features, respectively. (b) Frequencies of the absorption features as a function of pressure.*

according to the Equation 6.13.

$$SW(\omega) = \int_0^{\omega_c} \sigma_1(\omega) d\omega, \tag{6.13}$$

The spectral weight of E1 increases with increasing pressure. The three spin-forbidden transitions contribute very little to the total spectral weight, but over all the spectral weight of these features enhances with pressure upto ≈16 GPa, as shown in Figure 6.38 (a). Above 16 GPa the spectral weight of low-frequency spin-forbidden transition decreases by increasing pressure.

The P_c was calculated by plotting the absorbance intensity of E1 with respect to pressure as shown in Figure 6.39. The intensity of E1 increases linearly with increasing pressure upto 15 GPa, above it, there is an abrupt enhancement in the intensity with further increase of pressure. The anomalies in the frequency position of the observed excitations and also their spectral weight indicate the transition pressure region above 15 GPa.

Another absorption measurement on single crystal of $CdCr_2O_4$ was made at ambient conditions in higher-frequency range, as one of the test measurement of Vis-UV microspectrometer, which is described in Chapter 3.

The absorption spectrum along with measured spectrum at 1.0 GPa by using commer-

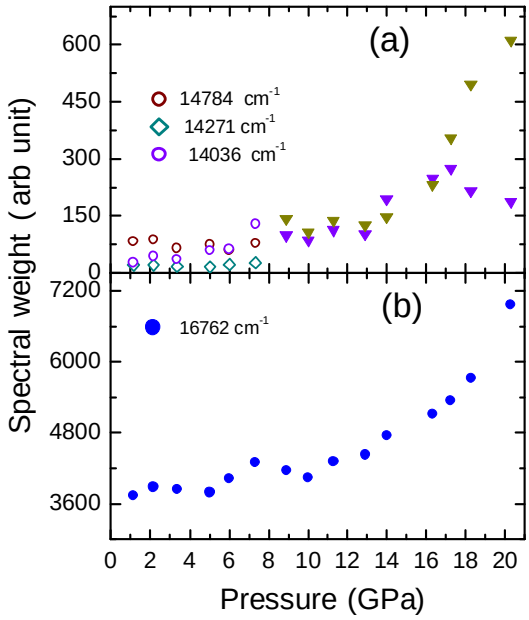

Figure 6.38: *Spectral weight of the absorption features of $CdCr_2O_4$ as a function of pressure,(a) spin forbidden transition and (b) the spin allowed transition E1. The values given in the ligand are for 1.1 GPa.*

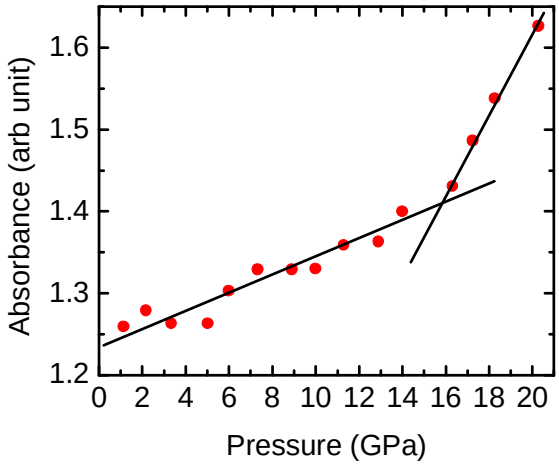

Figure 6.39: *The change in intensity of E1 in absorbance spectra of $CdCr_2O_4$ with increasing pressure. The black solid lines are guide to eye to see the transition pressure region.*

cial Bruker FTIR spectrometer is shown in Figure 6.40, there is consistency within the overlap frequency range. The pressure-dependent absorption measurement at higher frequency was not accomplished due to time constraint. The observed electronic excitations (*d-d* transition) are marked with numbers. These observed excitations are interpreted by using the Tanabe-Sugano diagram. The Cr^{3+} with $3d^3$ configuration has three spin allowed CF excitations and these excitations are stronger compared to spin forbidden transition. The small peaks within the frequency region 13785-15320 cm^{-1} marked by (1) are spin-forbidden transitions from ground state $^4A_{2g}$ to $^2E_g(^2G)$ and $^2T_{1g}(^2G)$. The peaks at $\approx$ 17760 cm^{-1} and at $\approx$ 22800 cm^{-1} marked by number (2) and (3) are the two spin-allowed transition from ground state $^4A_{2g}$ to $^4T_{2g}(^4F)$ and $^4T_{1g}(^4F)$, respectively. The absorption peaks marked by (4) and (5) at $\approx$ 29850 cm^{-1} and $\approx$ 34714 cm^{-1} are spin-forbidden transitions from ground state to $^2T_{1g}(^2G)$ and $^2T_{1g}(^2H)$, respectively. The third spin-allowed CF excitation at $\approx$ 39130 cm^{-1} marked by (6) is from ground state to $^4T_{1g}(^4P)$.

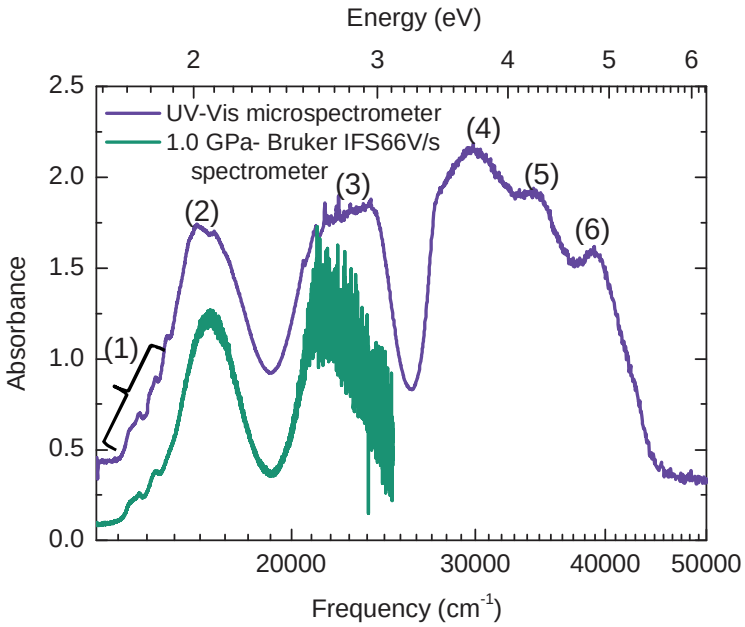

Figure 6.40: *Comparison of absorption spectrum measured in Vis-UV microspectrometer (this data is already shown in Chapter 3 as a test measurement of setup) with the room temperature measured spectrum at 1.0 GPa in Bruker FTIR spectrometer. The numbers show the observed crystal field excitations, their interpretation is given in text.*

6.6 Discussion

6.6.1 Low-energy excitation (phonons)

In order to compare the investigated Cr-spinel compounds, the two important facts are inferred from the phonon behaviour under pressure.
(i) The strength of the phonon modes, which reveals the ionic or covalent character of the particular compound.
(ii) The anomalies in the phonon parameters, which can attribute to the change in the symmetry of the crystal structure.
In order to find the compressibility factor of the compounds, the pressure coefficient A (cm^{-1}/GPa) of phonon modes for each compound are listed in Table 6.3. In all

Compounds	High-frequency phonon/*mode* 1	Low-frequency phonon/*mode* 2
$CdCr_2O_4$	5.41±0.25	3.75±0.17
$HgCr_2S_4$	5.25±0.08	3.80±0.06
$ZnCr_2Se_4$	3.68±0.1	3.28±0.07

Table 6.3: *Pressure coefficient A (cm^{-1}/GPa) of the phonon frequency as a function of pressure for three Cr-spinel compounds.*

investigated Cr-spinel compounds, the value of A for *mode* 2 is smaller compared to *mode* 1, which attributes to the fact that the respective bonding of *mode* 2 is stiffer compared to *mode* 1. Moreover the A values for the phonon modes of $CdCr_2O_4$ and $HgCr_2S_4$ are similar but larger than that $ZnCr_2Se_4$.

If i compare the compressibility of the three investigated Cr-spinel compounds the $ZnCr_2Se_4$ is more compressible compared to $HgCr_2S_4$ and $CdCr_2O_4$. In Ref [112] the compressibility difference between the $CdCr_2Se_4$ and oxide spinels is explained in terms of the size of the anions. Since most of the unit cell volume is occupied with anions, therefore the number of X-X bonds will be more compared to the other bonds i.e., X-X > Cr-X > A-X. In a periodic table from oxygen (O) to selenium (Se), the electronegativity of the elements decreases while the size of ion increases. The selenium (Se^{2-}) ion is bigger as compared to sulpher (S^{2-}) and the oxygen (O^{2-}) and bigger size of the ion corresponds to the longer bond length. On the application of external pressure the longer bond length will be affected more compared to the shorter bond length. The higher compressibility corresponds to the more metallic character of the chemical bond and lower ionicity of the anions [111]. $ZnCr_2Se_4$ shows metallic character, while $CdCr_2O_4$ shows insulating behavior because covalency increases from oxide to the selenide. In this way the overall compressibility is determined mainly by

the anion sublattice.

The character of the bond can also be obtained from the intensities of phonon modes. Higher intensity shows less covalent character of the bond. The mode intensities decreases moving from the oxide over the sulfide to the selenides, which gives the signal of an increasing covalency of the bonds [85].

Comparing the phonon anomalies of the investigated Cr-spinel compounds, $ZnCr_2Se_4$ shows the anomaly at around 10 GPa, which is interpreted in terms of structural phase transitions from cubic to tetragonal symmetry. This interpretation is supported by X-ray powder diffraction study [112], where a pressure-induced structural phase transformation from cubic ($Fd\bar{3}m$) to tetragonal ($I\bar{4}$)was reported for $CdCr_2Se_4$ at around 10 GPa. The phonon parameters of $HgCr_2S_4$ show an anomaly at around 13 GPa. The tentative assignment for it, is also structural phase transformation from cubic to tetragonal phase. In general, the solids containing ions with larger ionic radius have lower transition pressures. The oxide spinels are comparatively harder than sulphide and selenide spinels, therefore the structural phase transition in oxide spinels would occur at higher pressure. The Raman study of $ZnCr_2O_4$ under pressure reveals a sluggish structural phase transition which starts at 17.5 GPa and completes at around 35 GPa [113]. The infrared results of the $CdCr_2O_4$ show no anomaly up to the highest measured pressure (14.0 GPa), is in agreement with Raman Studies.

6.6.2 High-energy (CF) excitations

The energy values of the first spin allowed *d*-*d* transition (E1) for $ZnCr_2Se_4$, $HgCr_2S_4$ and $CdCr_2O_4$ are summarized in Table 6.4. The large value of Δ_{oct} for $CdCr_2O_4$ reveals that the *d*-orbitals of Cr^{3+} splits with a large energy difference, compared to sulphide and selenide compounds. The energy of E1 for $CdCr_2S_4$ [114] and for $ZnCr_2S_4$ [115] is reported as 14195 cm^{-1}, which suggests that the energies are independent of *A*-site ions, but the present results of $HgCr_2S_4$ show the center of gravity of E1 at 15500 cm^{-1} at lowest measured pressure (see Figure 6.30), which is cotradicting the above statement. In Ref [116] the center of gravity of crystal-field excitations for many chromium complexes are given, where Cr^{3+} is in octahedral environment e.g. $Cr(S,Se)_6$. The energies of two spin-allowed transitions from ground state $^4A_{2g}$ to the excited levels $^4T_{2g}$ and $^4T_{1g}$ vary from $\approx$ 13000-17000 cm^{-1} and $\approx$17000-22000 cm^{-1}, respectively. The spin-forbidden transitions $^4A_{2g}$ to ^2E_g, and $^2T_{2g}$, vary from 13000-14400 cm^{-1} and 18000-19200 cm^{-1}. The spin-forbidden transitions are narrower than spin-allowed transitions, and become allowed due to spin-orbit coupling [110, 117].

These high-frequency excitations E1 and E2 shift strongly with temperature and pressure. Previously there was a controversial discussion about the onset of two peak

Compounds	Δ_{oct}=10Dq
$CdCr_2O_4$	16760 cm^{-1}
$HgCr_2S_4$	15800 cm^{-1}
$ZnCr_2Se_4$	15000 cm^{-1}

Table 6.4: *The energies of the E1 transition from the ground state to* $^4T_{2g}$*, located at 10 Dq=*Δ_{oct} *for three investigated Cr-spinel compounds at 1.0 GPa.*

structure, the strong shift of absorption edge with temperature and magnetic field was assigned to interband transition [118–122]. Later on there have been suggestions that these absorption edges are not due to interband transitions but correspond to intraband *d*-*d* excitations [123–125].

For $ZnCr_2O_4$ the main absorption features at frequencies of 17450 cm^{-1} and at 23000 cm^{-1} are interpreted as two spin allowed CF excitations [126] and narrow features near to the two spin-allowed transition and interpreted as transitions inside the $t^3{}_{2g}$ band. In present infrared data of $CdCr_2O_4$, the CF excitations are weak in the reflectivity measurement but clearly visible in the absorption spectra. In chalcogenide spinels ($ZnCr_2Se_4$, $HgCr_2S_4$) the CF excitations are strong in the reflectivity measurement compared to oxide spinels ($CdCr_2O_4$). The strength of the CF excitations is attributed to strong hybridization effects in chalcogenide spinels between the chalcogenide *p* and the chromium *d*states [127].

The behavior of E1 under pressure is different for $CdCr_2O_4$ and chalcogenides spinels ($HgCr_2S_4$ and for $ZnCr_2Se_4$). In case of $CdCr_2O_4$, there is blue shift in frequency position of E1 with application of pressure, which reveals the enhancement of the crystal-field splitting with increasing pressure. This is consistent with the behavior of crystal-field excitations under pressure of other transition-metal oxides with transition-metal ion in octahedral environment [128]. In case of $HgCr_2S_4$ and $ZnCr_2Se_4$, there is E1 shows a red shift upon pressure application, which indicates that the crystal-field splitting reduces under pressure.

6.7 Physical properties of AV_2O_4

AV_2O_4 forms a cubic spinel structure, where the V sites form a pyrochlore lattice with geometrically frustrated antiferromagnetic interactions between the V sites. Vanadium V^{3+}, with electronic configuration $3d^2$ has total spin S=1. The two spins occupy the triply degenerate t_{2g} orbitals and the orbital degree of freedom is unfrozen in the system, which makes the system more complex. All vanadium spinel compounds

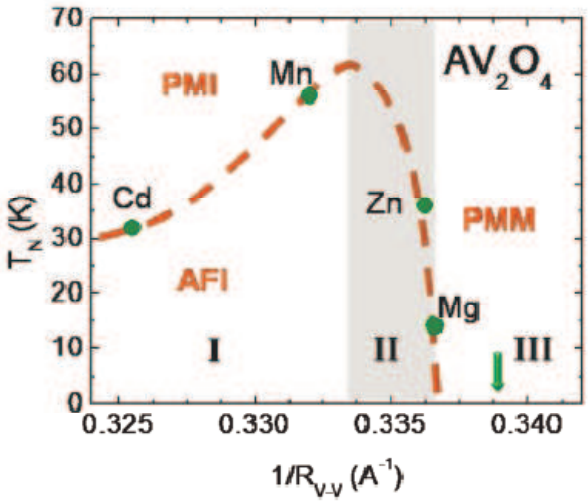

Figure 6.41: *Magnetic Phase diagram of AV_2O_4 spinels as a function of inverse V-V separation ($1/R_{V-V}$). The dotted line is guide to the eye. The vertical green arrow represents the critical distance for itinerant-electron behavior. The abbreviation PMI, AFI and PMM stands for paramagnetic insulator, antiferromagnetic insulator and paramagnetic metal, respectively. The figure is adopted from Ref [129].*

with *A*-site magnetic divalent ion like Cd^{2+}, Zn^{2+}, or Mg^{2+} show qualitatively similar structural and magnetic behavior with a structural transition at a higher temperature and an antiferromagnetic (AFM) transition at a slightly lower temperature [130, 131]. In ZnV_2O_4 and MgV_2O_4, there is a structural phase transition from cubic (Fd3m) to tetragonal (I41/amd) with c/a=0.9948 at 51 K and 65 K, respectively. At T_N=40 K, and 45 K, the tetragonal phase shows the paramagnetic to antiferromagnetic transition for ZnV_2O_4 and MgV_2O_4, respectively by lifting of the geometrical frustration [130–133].

The magnetic phase diagram of AV_2O_4 (A=Cd, Mn, Zn, Mg), where the evaluation of T_N with inverse V-V separation ($1/R_{V-V}$) is plotted, shown in Figure 6.41. The region I represents the localized-electron systems, i.e. A=Cd and Mn, while the systems (A=Zn, Mg) are located in the intermediate regime II between localized and itinerant electron phase. The value of T_N will increase as the V-V distance decreases due to chemical pressure when going from Cd to Mn. There is an anomalous variation in T_N as it reaches the intermediate regime II, which is interpreted in terms of U/t ratio, where U is the on-site coulomb repulsion considered to be pressure independent and t is the band width (hopping integral) which is a pressure dependent parame-

ter. First the ratio of U/t reduces as the V-V separation decreases and then collapses near the itinerant limit because of the electron delocalization along V-V bonds [129], which manifest that U is no longer pressure independent in the intermediate regime (for ZnV_2O_4 and MgV_2O_4). The orbital order in AV_2O_4 is a subject of controversy

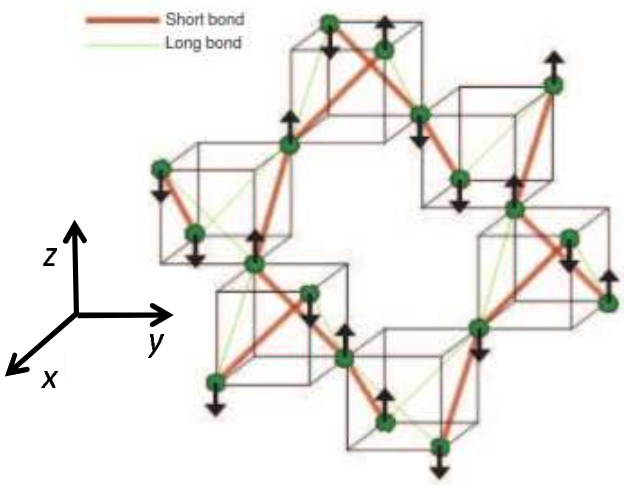

Figure 6.42: *Schematic representation of the dimerized structure resulting from ab-initio calculations for ZnV_2O_4. Bold line represents short bonds and thin lines show long bonds in-chain. The magnetic structure is indicated by arrows. The figure is adopted from Ref [134].*

because of competing spin, orbital, and lattice degrees of freedom. which makes the nature of the system complicated. In literature few groups [135–137] claim orbital ordering in vanadium spinels. They proposed that the high temperature structural transition (≈50 K for ZnV_2O_4) is due to orbital ordering assisted by the Jahn-Teller distortion. Consecutively there is a magnetic transition (AFM at ≈40K for ZnV_2O_4), which is due to lifting of geometrical spin frustration because of orbital ordering. In this scenario in all V-sites the d_{xy} orbital is occupied with an electron and the other electron occupies d_{xz} and d_{yz} orbitals alternatively along the c-direction. This uniform occupation of d_{xy} orbitals leads to an enhancement of the anti-ferro (AF) spin correlation along one dimensional chain lying in the xy-planes, thus the magnetic frustration is partially lifted. In case of no orbital ordering the system remains strongly frustrated, e.g., chromium spinels, where the Cr^{3+} ion has the $3d^3$ electron configuration with total spin of 3/2 and no orbital degrees of freedom. These compounds show only one transition at very low temperature (between 10-20K). Pardo et al, [134] claims

that there is no orbital ordering in the AV_2O_4 compounds, only the higher occupancy of d_{xy} orbital is observed. The V-V dimerization along [011] and [101] direction (see Figure 6.42) due to small values of U lead to the lattice distortion. With pressure the U/t ratio decreases and the partial electronic delocalization in the systems occurs in the itinerant-electron limit. The magnetic transition below 50 K for ZnV_2O_4 and MgV_2O_4 is due to V-V bond in the dimer.

6.8 Investigated AV_2O_4 compounds

The pressure-dependent transmittance and absorbance of ZnV_2O_4 and MgV_2O_4 was studied in the frequency range (550-7000 cm^{-1}) up to ≈20.5 GPa.

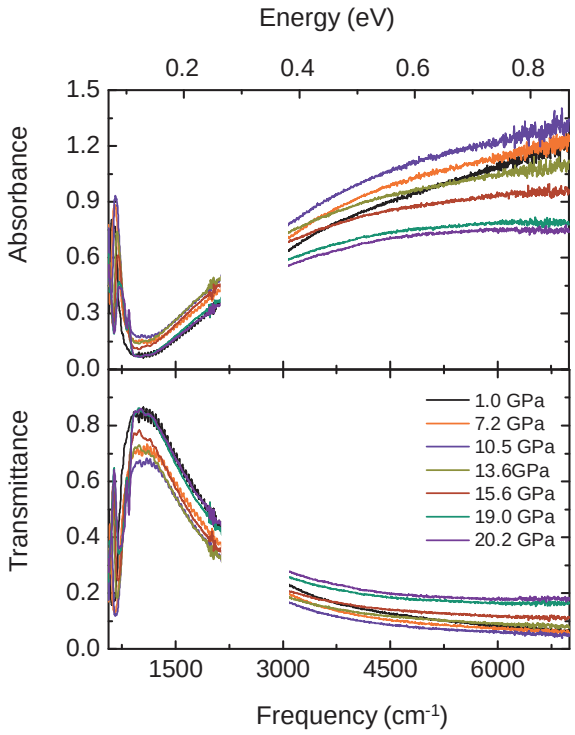

Figure 6.43: *Pressure-dependence of the transmittance and the absorbance spectra of ZnV_2O_4 for selected pressures.*

Figure 6.43 and 6.44 shows the transmittance and the absorbance spectra of ZnV_2O_4 and MgV_2O_4, respectively in the mid-infrared frequency range. There are two main contributions to the mid-infrared spectra, at lower-frequency side there is one of the four phonon modes expected for cubic spinel compounds and the optical charge gap manifested by the rapid increase in the absorbance intensity at higher-frequency side.

The diamond multiphonon absorption in the frequency range 1700-4200 cm^{-1} causes artifacts, and in some frequency region it can not be ruled out completely from the spectra measured with DAC, and therefore they are cut out from the data.

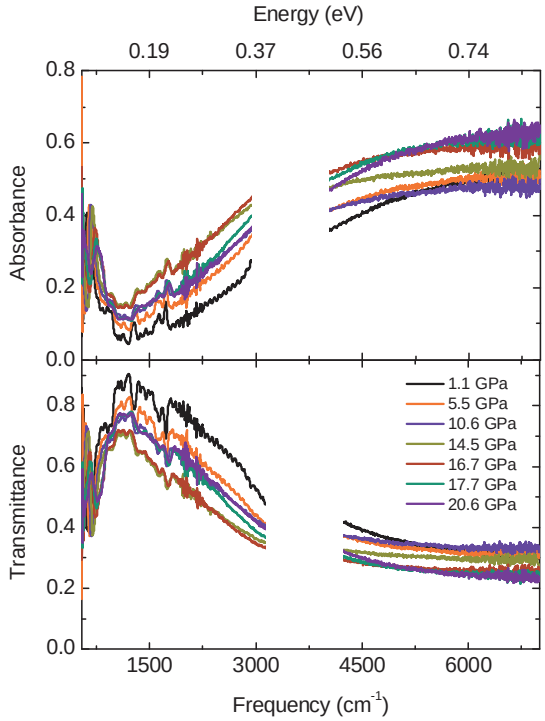

Figure 6.44: *Pressure-dependence of the transmittance and the absorbance spectra of MgV_2O_4 for selected pressures.*

The phonon modes in the cubic spinel compounds are already discussed in the previous section (see Section 6.4.1) of this chapter. For ZnV_2O_4, the measurements were extended to far-infrared frequency range up to 14.2 GPa. The absorbance spectra at 1.0 GPa and 14.2 GPa are shown in Figure 6.45. The lowest-frequency phonon mode (*mode* 4) is beyond of our experimental limit, only the onset of this mode is observed in measured spectra. The phonon modes are quite broad even at the lowest measured pressure (1.0 GPa) as compared to the single crystal data [138]. The broadening of the modes increases significantly with increasing pressure (see Figure 6.45), which makes the quantitative analysis of the data more difficult. The broadening of the phonon modes is attributed to the polycristallinity of the sample.

In Figure 6.46 the absorbance spectra are divided into two different pressure regions, low pressure range and high pressure range. Initially, with the application of pressure the absorbance level increases up to a certain pressure P_c for both compounds (ZnV_2O_4

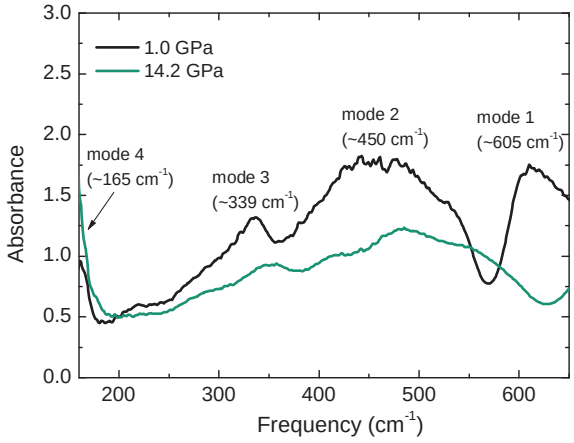

Figure 6.45: *Far-infrared absorbance spectra of ZnV_2O_4 for two selected pressures. The phonon frequencies of four IR active modes at 1.0 GPa are indicated.*

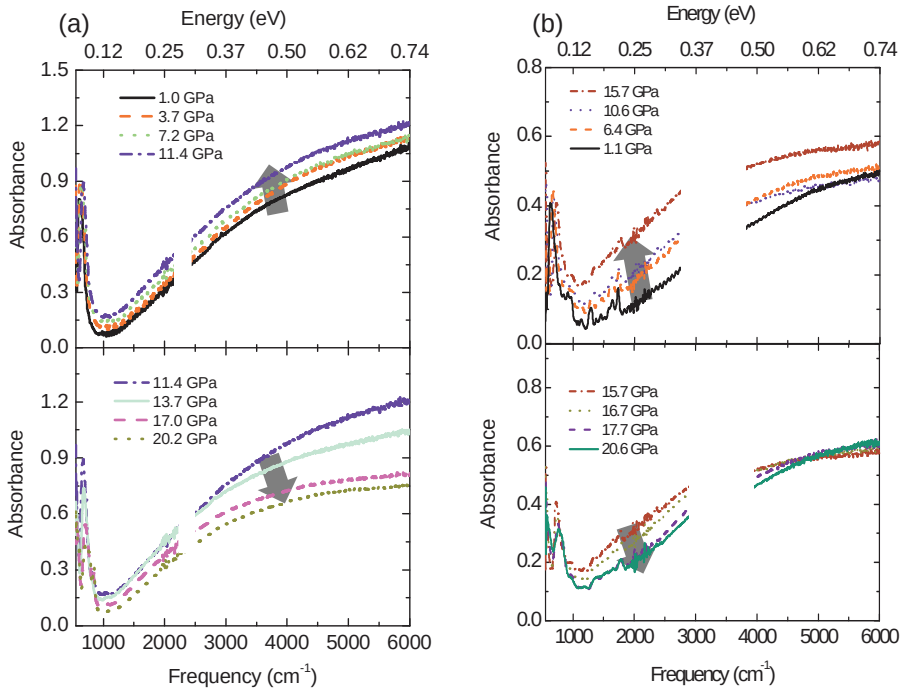

Figure 6.46: *Absorbance spectra of (a) ZnV_2O_4 and (b) MgV_2O_4 in the mid-infrared range. The upper panels of the figures represents the low-pressure region and spectra measured in high- pressure range are plotted in lower panels of the figures.*

and MgV_2O_4). Above P_c the absorbance level decreases and the shape of the spectra also change. The P_c value for ZnV_2O_4 and MgV_2O_4 is ∼12 GPa and ∼15.7 GPa, respectively.

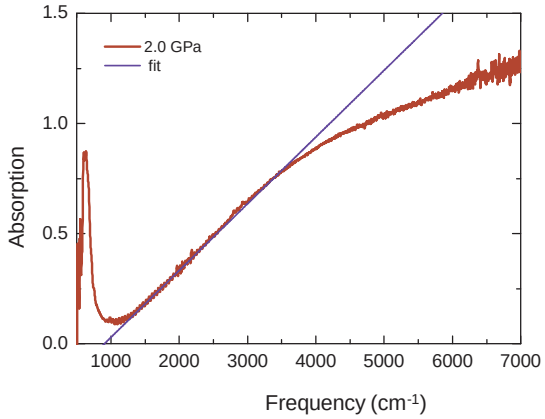

Figure 6.47: *The estimation of the charge gap by the intersection of the linear extrapolation of the absorption edge with the frequency axis for the lowest measured pressure (1.0 GPa) of ZnV_2O_4.*

From the absorbance spectra, the charge gap as a function of pressure was obtained by the intersection of the linear extrapolation of the absorption edge with the frequency axis, as illustrated in Figure 6.47. For pressures below P_c the absorption edge shifts to lower energies,i.e., the charge gap is reduced and for pressures above P_c the absorption edge gradually shifts to higher frequency with increasing pressures manifesting the opening of the charge gap (see Figure 6.48).

Moreover the pressure-induced instability is also found from the behavior of the observed phonon mode (*mode* 1) in both vanadium compounds. The pressure-dependent behavior of *mode* 1 of ZnV_2O_4 and MgV_2O_4 is shown in Figure 6.49 (a)and (b), respectively. Although the phonon excitation is quite broad already at the lowest pressure, a three-fold splitting of the phonon mode is clearly visible, starting at around P_c≈12 GPa for ZnV_2O_4 and P_c≈15 GPa for MV_2O_4 . The low-frequency part of the absorbance spectra of ZnV_2O_4 and MgV_2O_4 were fitted to obtain the contributions to the phonon excitation.

For ZnV_2O_4 and MgV_2O_4 the illustration of the fitting for three selected pressures and the results of the fitting are presented in Figure 6.50 and 6.51. Below P_c the phonon mode can be describe with one Lorentz oscillator, while above P_c three-fold splitting of the mode is observed for both compounds and three oscillators are needed to explain the phonon excitation. The phonon modes harden upon pressure applica-

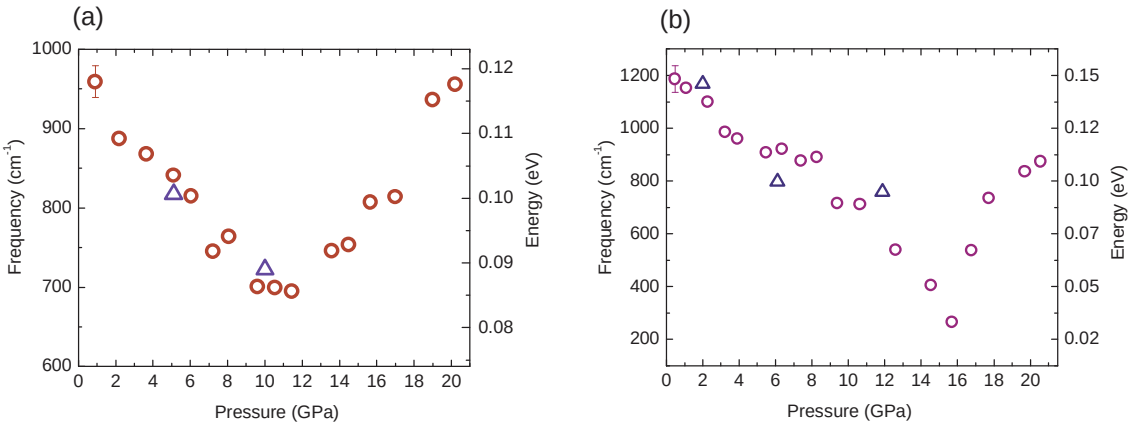

Figure 6.48: *The position of the absorption edge as a function of pressure for (a) ZnV_2O_4 and (b) MgV_2O_4. The blue triangles show the releasing pressures.*

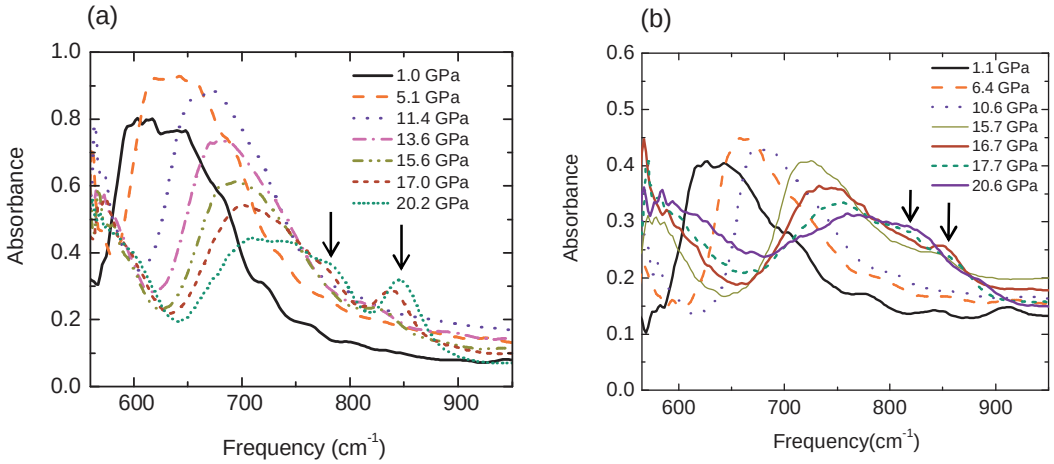

Figure 6.49: *The pressure effect on the highest-frequency phonon mode (mode 1)of (a) ZnV_2O_4 and (b) MgV_2O_4 . The three-fold splitting of this phonon mode with increasing pressure is indicated by the arrows, for the highest measured pressures.*

tion and these pressure-induced changes are reversible (see Figure 6.50 (b) and Figure 6.51 (b)). The ZnV_2O_4 and MgV_2O_4 being Mott-Hubbard insulators are located in the crossover regime between the localized and itinerant electron phase [129]. By applying pressure the V-V separation will decrease which increasing the t (hopping integral) and consequently the U/t ratio decreases and the system goes to the

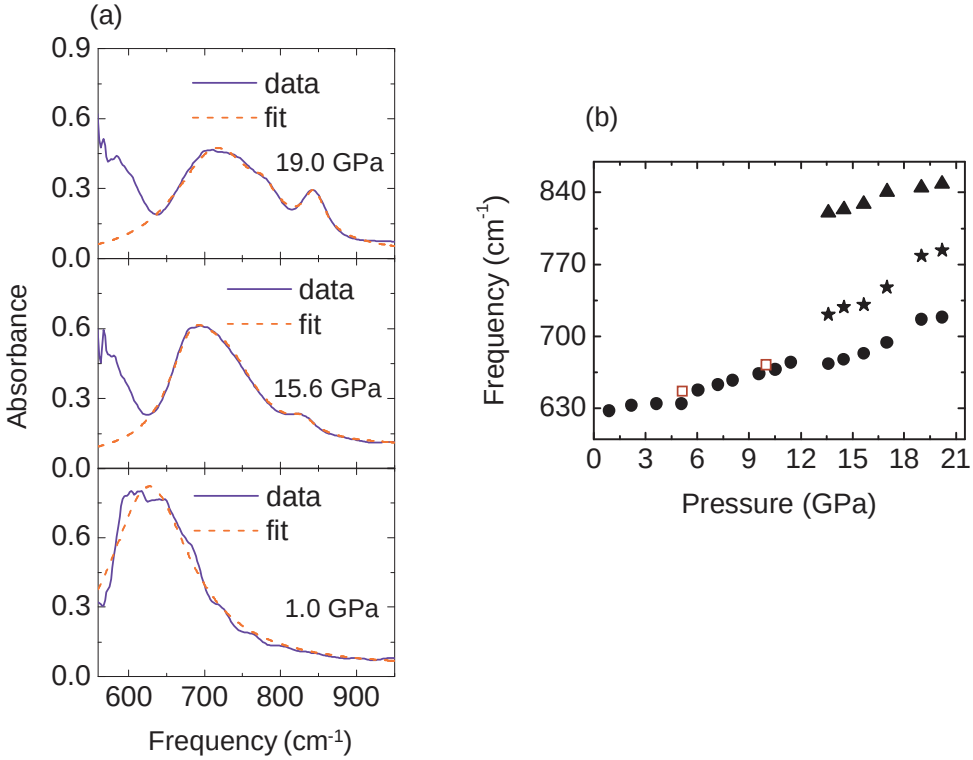

Figure 6.50: *(a) Fit of the mode 1 of ZnV_2O_4 with the Lorentz model for three different pressures. Above P_c≈12 GPa three oscillators are necessary to describe the excitation. (b) Frequency of the mode 1 as a function of pressure, obtained from the fitting. The open red squares indicate the frequency of mode 1 for releasing pressures.*

metallic phase. In case of ZnV_2O_4, the charge gap decreases from 960 cm^{-1}(0.12 eV) to 695 cm^{-1}(0.086 eV) at pressure ≈12 GPa, further increase in pressure opens the gap. MgV_2O_4 also show the similar behaviour, first the charge gap reduced from 1243 cm^{-1}(0.15 eV) to 107 cm^{-1}(0.013 eV) with increase in pressure up to ≈15.7 GPa, upon further application of pressure the charge gap starts to increase.

Ab initio calculations predict an insulator-to-metal transition at around 6.5 GPa for MgV_2O_4 with a critical V-V distance of 2.937 Å, if the crystal symmetry remains unchanged [129, 139]. The density of states plots (DOS) at ambient conditions and at 8GPa are shown in Figure 6.52 (a) and (b), respectively. At ambient conditions the system is Mott-Hubbard insulator with a *d-d* gap of 0.2 eV.By applying pressure the V-V separation will decrease leads to a stronger *d-d* interaction. At high enough pressure, the valence and conduction bands overlap and a metallic behavior is expected

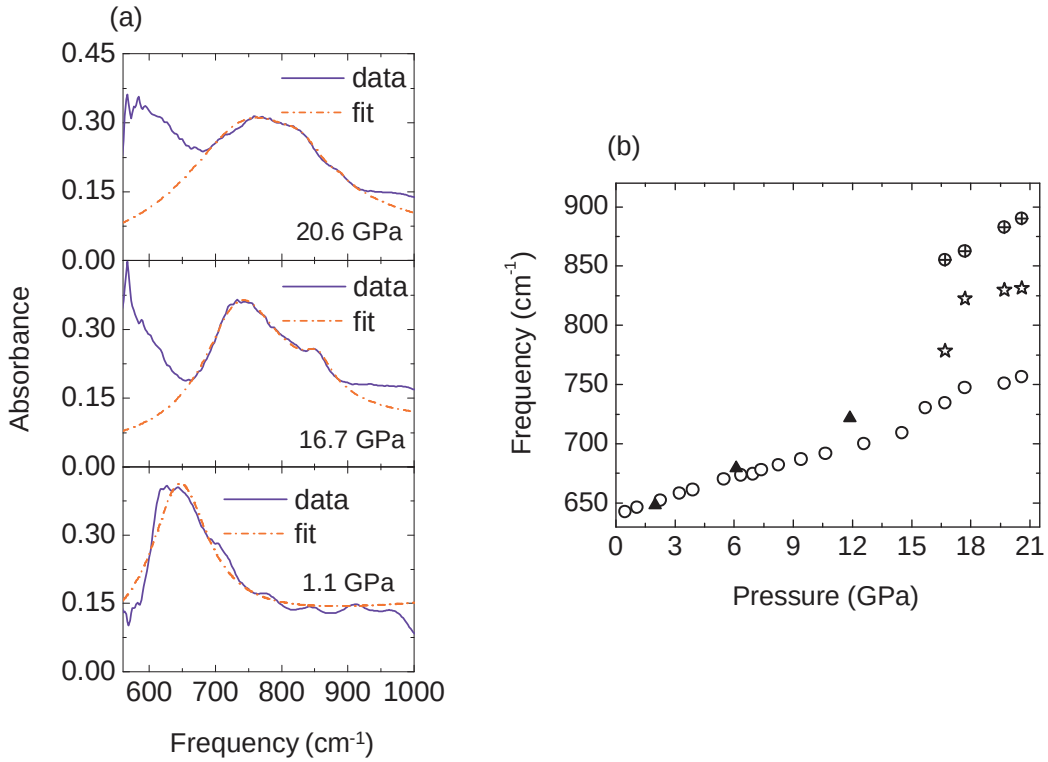

Figure 6.51: *(a) Fit of the mode 1 of MgV_2O_4 with the Lorentz model for three different pressures. Above $P_c \approx 15$ GPa three oscillators are necessary to describe the excitation. (b) Frequency of the mode 1 as a function of pressure, obtained from the fitting. The black triangles indicate the frequency of mode 1 for releasing pressures.*

in the system.

The prediction of a pressure-induced insulator-to-metal transition is in agreement with our findings of the shift of the absorption edge (charge gap) to lower frequency with increasing pressure up to P_c. The charge gap is reduced, and thus the insulator-to-metal transition is approached. However, above P_c the trend is reversed, i.e., the charge gap increases with increasing pressure. The pressure-dependent investigation of phonon reveals an anomaly at around P_c for ZnV_2O_4 and MgV_2O_4 (see Figure 6.50(b) and 6.51(b)).The new phonon modes appear, which reveal the lowering of the symmetry of the system. This symmetry change is attributed to the structural phase transition at critical pressure.

Since, the size of A-site ionic radii affects the distortion of VO_6 octahedron, larger the size of divalent cation makes the octahedra more distorted [140]. By comparing

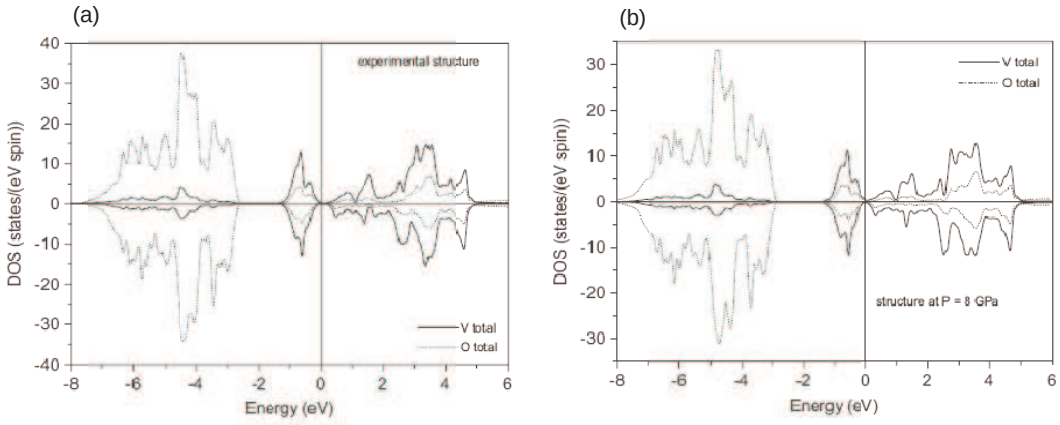

Figure 6.52: *DOS plots for all the V and O levels in the unit cell for MgV2O4, upper (lower) panels show the spin-up (down) channel. (a) The d-d character of the narrow gap of only 0.2 eV can be observe at ambient conditions, (b) at pressure of 8 GPa, due to the small V-V distance the overlapping of d-bands occur and consequently metallic character of the system is observed. The figure is adopted from Ref [139].*

the infrared results of both compounds ZnV_2O_4 and MgV_2O_4, the pressure-induced changes in ZnV_2O_4 are observed at lower pressure compared to the MgV_2O_4. Thus it can be concluded that ZnV_2O_4 system become more delicate because of strongly distorted octahedra due to the larger size of the Zn ion compared to the Mg ion. Therefore the system ZnV_2O_4 becomes more sensitive to the external parameters compared to MgV_2O_4, and consequently pressure-induced transitions occur at lower pressure.

7 Summary and outlook

The influence of high hydrostatic pressures on electronic and structural properties of various transition metal compounds is the subject of this thesis. A large part of the measurements has been performed using high brilliance far-infrared and X-ray radiation of synchrotron sources. Combined with in-house experimental facility, our optical spectroscopy covers a very broad frequency range from 200 up to 25000 cm^{-1} (25 meV-3 eV). In addition, in order to extend high-pressure low-temperature spectroscopic measurements in UV range (above 3 eV), a Vis-UV microspectrometer has been set up and tested.

The XRD study of $\beta-Na_{0.33}V_2O_5$ under pressure was performed in order to investigate the structural changes in a higher pressure regime (P>12 GPa). The recent optical study on single crystal of $\beta-Na_{0.33}V_2O_5$ under pressure manifest that some structural changes are happening at around 12 GPa. In Raman data there are the anomalous changes in pressure range 9-12 GPa, but most of the structural features in infrared and Raman data remains up to 20 GPa. From XRD study, it is shown that the room-temperature crystal structure of $\beta-Na_{0.33}V_2O_5$ remains monoclinic with space group C2/m up to 20 GPa. We observe anomalies for all lattice parameters in the pressure range 12-15 GPa, in full agreement with recent optical study of this compound which showed that all spectroscopic signatures are present up to high pressure.

The pressure-dependent infrared spectroscopic measurements on $BiFeO_3$ were performed in the frequency range 200-700 cm^{-1}. The behavior of phonons under pressure reveals two structural phase transitions. The first structural phase transition occurs at 3 GPa toward a distorted monoclinic perovskite structure, which is characterized by the superimposition of tilts and cation displacement. With further increasing pressure the cation displacements of $BiFeO_3$ are reduced and finally suppressed at around 7 GPa leading to the nonpolar *Pnma* structure. The observed structural instabilities confirm the theoretical predictions and are in agreement with other experimental data obtained by Raman and XRD under pressure.

Among chromium spinels, three compounds $ZnCr_2Se_4$, $HgCr_2S_4$, and $CdCr_2O_4$ were investigated in a broad spectral range. These compounds showed different compressibilities under pressure, which are interpreted in terms of different size of anions. The

anomalous changes in phonon parameters of $ZnCr_2Se_4$, $HgCr_2S_4$ were interpreted as a signature of structural phase transitions. The effect of pressure on $CdCr_2O_4$ is weaker compared to the other two chalcogenide spinels. In $CdCr_2O_4$, no anomaly in the phonon parameters was observed up to the highest measured pressure. For $ZnCr_2Se_4$ and $HgCr_2S_4$ the crystal field excitations exhibit a red shift upon pressure application, which indicates the splitting of d-orbital is reduced with pressure. The opposite behavior was observed for $CdCr_2O_4$, the crystal-field excitations show blue shift with increasing pressure revealing the enhancement of crystal-field splitting.

Among vanadium spinels, the ZnV_2O_4 and MgV_2O_4 was investigated by pressure-dependent transmittance measurement in mid-infrared frequency range up to ≈20 GPa. The behavior of the absorption edge shows that the charge gap is monotonically reduced with increasing pressure up to about P_c, but increases at pressures above P_c. Further indications of a pressure-induced instability are found in the phonon spectra. A three-fold splitting of the phonon mode was observed at around P_c, indicating a symmetry lowering.

The technique of infrared spectroscopy under pressure utilized in this work has provided a vast information about structural phase transitions and electronic structure and, thus, proved to be an efficient tools for study of transition metal compounds. In every frequency range (from FIR up to UV) important changes occur under pressure and one gets a lot of information about the material´s properties. The new Vis-UV microspectrometer can provide the frequency range, to investigate about d-d transitions and the charge transfer excitations as a function of pressure, in Cr-spinel compounds and other transition metal compounds.

It would be interesting to investigate the Cr-spinels in higher frequency (>3 eV) range in order to cover all d-d crystal-field excitations. Indeed the Cr-spinels show a rich magnetic phase diagram, the ferromagnetic exchange is strongly increased in compounds with larger lattice constant, while the compounds with smaller lattice constants show antiferromagnetic exchange. It has been demonstrated that the magnetic exchange interaction and the onset of the magnetic order strongly influences the phonon modes, which could be probed by infrared spectroscopy. Thus the application of external pressure provides an efficient way to tune the magnetic properties in these system. Our results clearly demonstrate that the utilized high-pressure infrared spectroscopy possesses high enough sensitivity for tracing these effects. Infrared measurements under pressure at low temperatures are desirable in order to investigate the interplay of spin and lattice degrees of freedom at the magnetic phase transition.

Bibliography

[1] D. Fan, W. Zhou, C. Liu, Y. Liu, X. Jiang, F. Wan, J. Liu, X. Li, and H. Xie, J. Mater. Sci. **43**, 5546 (2008).

[2] G. Huber, K. Syassen, and W. B. Holzapfel, Phys. Rev. B **15**, 5123 (1977).

[3] M. I. Eremets, *High pressure experiemental methods* (Oxford university press, New York, 1996).

[4] S. Klotz, J.-C. Chervin, P. Munsch, and G. L. Marchand, J. Phys. D: Appl. Phys **42**, 075413 (2009).

[5] K. Syassen and I. Loa, private communication.

[6] D. F. Nelson and M. D. Sturge, Phys. Rev **137**, A1117 (1965).

[7] H. K. Mao, J. Xu, and P. M. Bell, J Geophys. Res **91**, 4673 (1986).

[8] A. Jayaraman, Rev. Mod. Phys **55**, 65 (1983).

[9] A. Jayaraman, Rev. Sci. Instrum **57**, 1013 (1986).

[10] R. Letoullec, J. P. Pinceaux, and P. Loubeyre, High Pressure Research **1**, 77 (1988).

[11] K. Thirunavukkuarasu, *PhD Thesis: Carbon Nanostructurees Under High Pressure Studied By Infrared Spectroscopy* (University of Augsburg, Augsburg, 2009).

[12] M. I. Eremets and Y. A. Timofeev, Rev. Sci. Instrum. **63**, 3123 (1992).

[13] W. Hayes and R. Loudon, *Scattering of light by crystals* (John Wiley and sons, UK, YEAR).

[14] F. Wooten, *Optical properties of Solids* (Academic press, USA, 1972).

[15] M. Fox, *Optical properties of Solids* (Oxford University press, New York, USA, 2001).

[16] M. Dressel and G. Grüner, *Electrodynamics of Solids* (Cambridge University press, UK, 2002).

[17] A. S. Barker, Phys. Rev B **12**, 4071 (1975).

[18] F. Gervais, *in Infrared and Millimeter Waves, edited by K. J. Button* (Academic, New York, USA, 1983).

[19] J. S. Plaskett and P. N. Schatz, J. Chem. Phys **38**, 612 (1963).

[20] M. M. Woolfson, *An introduction to X-ray crystallography;Second Edition* (Cambridge University Press, United Kingdom, 1997).

[21] H. P. Klug and L. E. Alexander, *X-ray diffraction procedure:Second Edition* (John wiley and Sons, Inc, New York, 1954).

[22] H. Yamada and Y. Ueda, J. Phys. Soc. Jpn **68**, 2735 (1999).

[23] M. Wunsche, phD thesis, 2003.

[24] A. L. Bail, H. Duroy, and J. L. Fourquet, Material Research Bulletin **23**, 447 (1988).

[25] H. M. Rietveld, J.Appl.Cryst **2**, 65 (1969).

[26] R. A. Young and D. I. Wiles, J.Appl.Cryst **15**, 430 (1982).

[27] K. Syassen and R. Sonnenschein, Rev. Sci. Instrum **53**, 644 (1982).

[28] K. Y. Vohra, Scripta Metallurgica **22**, 145 (1988).

[29] Kato, US patent. **19**, 1 (1992).

[30] A. Pashkin, unpublish work.

[31] Manual, andor Shamrock spectrograph SR-303i.

[32] Kathrin Mattern, *Master Thesis: Einführung in Zemax: Grundlegende Funktion und ein einführendes Beispiel* (University of Augsburg, Augsburg, 2010).

[33] A. Huber, phD project (continue).

[34] S. Frank, I. Gregora, J. Petzelt, T. Yamauchi, Y. Ueda, and C. A. Kuntscher, Phys. Rev. B **76**, 075128 (2007).

[35] A. D. Wadsley, Acta Cryst **8**, 695 (1955).

[36] T. Yamauchi and Y. Ueda, Phys. Rev. B **77**, 104529 (2008).

[37] C. A. Kuntscher, S. Frank, I. Loa, K. Syassen, T. Yamauchi, and Y. Ueda, Phys. Rev. B **71**, 220502 (2005).

[38] F. D. Murnagghan, Proc. Natl. Acad. Sci. USA **30**, 244 (1944).

[39] J.Yamaura, T.Yamauchi, E. Ninomiya, H. Sawa, M. Isobe, H.Yamada, and Y. Ueda, J. Magn. Magn. Mater **272-276**, 438 (2004).

[40] C. Ederer and N. A. Spaldin, Phys. Rev. B **71**, 224103 (2005).

[41] H. Béa, M. Bibes, S. Fusil, K. Bouzehouane, E. Jacquet, K. Rode, P. Bencok, and A. Barthélémy, Phys. Rev. B **74**, 020101(R) (2006).

[42] S. Picozzi and C. Ederer, J. Phys.: Condens, Matter. **21**, 303201 (2009).

[43] P. D. Thang, M. T. N. Pham, G. Rijnders, D. H. A. Blank, N. H. Duc, J. C. P. Klaasse, and E. Brück, J. Korean Phys. Soc. **52**, 1406 (2008).

[44] G. Hallinger, F. J. Himpsel, B. Reihl, P. Pertosa, and J. P. Doumerc., Solid. Stat. Com **44**, 1221 (1982).

[45] R. Haumont, J. Kreisel, and P. Bouvier, Phase Transitions **79**, 1043 (2006).

[46] J. T. Last, Phys. Rev **105**, 1740 (1957).

[47] C. Michel, J.-M. Moresu, G. D. Achenbechi, R. Gerson, and W. James, Solid State Comm **7**, 701 (1969).

[48] F. Kubel and H. Schmid, Acta Cryst. B **46**, 698 (1990).

[49] R. P. S. M. Lobo, R. L. Moreira, D. Lebeugle, and D.Colson, Phys. Rev. B **76**, 172105 (2007).

[50] G. A. Smolenskii, V. A. Isupov, A. I. Agranovskay, and N. N. Krainik, Sov. Phys. Solid state **2**, 2651 (1961).

[51] J. Wang, J. B. Neaton, H. Zheng, V. Nagarajan, S. B. Ogale, B. Liu, D. Viehland, V. Vaithyanathan, D. G. Schlom, U. V. Waghmare, N. A. Spaldin, K. M. Rabe, M. Wuttig, and R. Ramesh, Science **299**, 1719 (2003).

[52] Y. P. Wang, L. Zhou, J.-M. L. M. F. Zhang and, X. Y. Chen and, and Z. G. Liua, Appl. Phys. Lett. **84**, 1731 (2004).

[53] J. B. Neaton, C. Ederer, U. V. Waghmare, N. A. Spaldin, , and K. M. Rabe, Phys. Rev. B **71**, 014113 (2005).

[54] V. V. Shvartsman, W. Kleemann, R. Haumont, and J. Kreisel, Appl. Phys. Lett **90**, 172115 (2007).

[55] Y. Yang, L. G. Bai, K. Zhu, Y. L. Liu, S. Jiang, J. Liu, J. Chen, and X. R. Xing, J. Phys.: Condens. Matter **21**, 385901 (2009).

[56] R. Haumont, P. Bouvier, A. Pashkin, K. Rabia, S. Frank, B. Dkhil, W. A. Crichton, C. A. Kuntscher, and J. Kreisel, Phys. Rev. B **79**, 184110 (2009).

[57] P. Ravindran, R. Vidya, A. Kjekshus, H. Fjellvag, and O. Eriksson, Phys. Rev. B **74**, 224412 (2006).

[58] A. G. Gavriliuk, V. V. Struzhkin, I. S. Lyubutin, S. G. Ovchinnikov, M. Y. Hu, and P. Chow, Phys. Rev. B **77**, 155112 (2008).

[59] A. G. Gavriliuk, V. V. Struzhkin, I. S. Lyubutin, M. Y. Hu, and H. K. Mao, JETP.Lett **82**, 224 (2005).

[60] A. G. Gavriliuk, I. S. Lyubutin, and V. V. Struzhkin, JETP.Lett **86**, 532 (2007).

[61] J. F. Scott, R. Palai, A. Kumar, M. K. Singh, N. M. Murari, N. K. Karan, and R. S. Katiyar, J. Am. Ceram. Soc **91**, 1762 (2008).

[62] O. E. González-Vázquez and J. I. Niguez, Phys. Rev. B **79**, 064102 (2009).

[63] N. W. Ashcroft and N. D. Mermin, *Solid State Physics* (Harcourt Brace College Publishers, Fort Worth, 1976).

[64] F. Birch, J. Geophys. Res **83**, 1257 (1978).

[65] W. B. Holzapfel, Rep. Prog. Phys **59**, 29 (1996).

[66] S. Kamba, D. Nuzhnyy, M. Savinov, J. Sebek, J. Petzelt, J. Prokleska, R. Haumont, and J. Kreisel, Phys. Rev. B **75**, 024403 (2007).

[67] P. Hermet, M. Goffinet, J. Kreisel, and P. Ghosez, Phys. Rev. B **75**, 220102(R) (2007).

[68] R. Haumont, J. Kreisel, P. Bouvier, and F. Hippert, Phys. Rev. B **73**, 132101 (2006).

[69] H. Fukumura, S. Matsui, H. Harima, T. Takahashi, T. Itoh, K. Kisoda, M. Tamada, Y. Noguchi, and M. Miyayama, J. Phys.:Condens. Matter **19**, 365224 (2007).

[70] P. Lunkenheimer, T. Rudolf, J. Hemberger, A. Pimenov, S. Tachos, F. Lichtenberg, and A. Loidl, Phys. Rev. B **68**, 245108 (2003).

[71] P. Fischer, M. Polomska, I. Sosnowska, and M. Szymanski, J. Phys.C: Sol. Stat. Phys **13**, 1931 (1980).

[72] M. Guennou, P. Bouvier, R. Haumont, G. Garbarino, and J. Kreisel, arXiv:1105.2676v1 (2011).

[73] A. A. Belik, H. Yusa, N. Hirao, Y. Ohishi, and E. Takayama-Muromachi, Chem. Mater **21**, 3400 (2009).

[74] K. E. Sickafus and J. M. Wills, J. Am. Ceram. Soc., **82**, 3279 (1999).

[75] E. J. W. Verwey and J. H. de Boer, Recl. Trav. Chim. Pays-Bas., **55**, 531 (1936).

[76] E. J. W. Verwey, P. W. Haayman, and F. C. Romeijn, Recl. Trav. Chim. Pays-Bas., **15**, 181 (1947).

[77] E. J. W. Verwey and E. L. Heilmann, J. Chem. Phys., **15**, 174 (1947).

[78] M. Imada, A.Fujimori, and Y. Tokura, Rev.Mod.Phys. **70**, 1039 (1998).

[79] B. N. Figgis and M. A. Hitchman, *Ligand Field Theory and its Applications* (Wiley-VCH, New York., 1999).

[80] A. D. Liehr, J. Phys. Chem. **67**, 1314 (1963).

[81] P. Jacobs, *Group Theory With Applications in Chemical Physics* (Cambridge University Press, The Edinburgh Building, Cambridge cb2 2ru,UK., 2005).

[82] P.A.Cox, *Transition metal oxides* (Clarendon Press, Oxford,UK., 1992).

[83] P. Sahebsara and S. D, Phys. Rev. Lett. **100**, 136402 (2008).

[84] A. P. Ramirez, Ann. Rev. **24**, 453 (1994).

[85] T. Rudolf, C. Kant, F. Mayer, J. Hemberger, V. Tsurkan, and A. Loidl, New J. Phys **9**, 76 (2007).

[86] Y. Yamashita and K.Ueda, Phys. Rev. Lett. **85**, 4960 (2006).

[87] O. Tchernyshyov, R. Moessner, and S. L. Sondhi, Phys. Rev. Lett. **88**, 067203 (2002).

[88] C. Kant, J. Deisenhofer, T. Rudolf, F. Mayer, F. Schrettle, and A. Loidl, cond-mat. **arXiv:0906.3639v1**, 1 (2009).

[89] H. Ueda, H. A. Katori, H. Mitamura, T. Goto, and H. Takagi, Phys. Rev. Lett. **94**, 047202 (2005).

[90] V. Tsurkan, J. Hemberger, A. Krimmel, H.-A. K. von Nidda, P. Lunkenheimer, V. Z. S. Weber, and A. Loidl, Phys. Rev. B **73**, 224442 (2006).

[91] N. Menyuk, K. Dwight, R. J. Arnott, and A. Wold, J. Appl. Phys. **37**, 1387 (1966).

[92] P. K. Baltzer, P. J. Wojtwicz, M. Robbins, and E. Lopatin, Phys. Rev. **151**, 367 (1966).

[93] T. Rudolf, C. Kant, F. Mayr, M. Schmidt, V. Tsurkan, J. Deisenhofer, and A. Loidl, Eur. Phys. J. B **68**, 153 (2009).

[94] T. Watanabe, J. Phys. Soc. Japan **37**, 140 (1974).

[95] S. Weber, P. Lunkenheimer, R. Fichtl, J. Hemberger, V. Tsurkan, and A. Loidl, Phys. Rev. Lett. **96**, 157202 (2006).

[96] J. Hemberger, T. Rudolf, H.-A. K. von Nidda, F. Mayr, A. Pimenov, V. Tsurkan, and A. Loidl, Phys. Rev. Lett. **97**, 087204 (2006).

[97] K. Wakamura, T. Arai, and K. Kudo, J. Phys. Soc. Japan. **40**, 1118 (1976).

[98] J. Zwinscher and H. D. Lutz, J. Solid State Chem. **118**, 43 (1995).

[99] D. Basak and J. Ghose, Spectrochimica Acta **50A**, 713 (1994).

[100] T. Rudolf, C. Kant, F. Mayr, J. Hemberger, V. Tsurkan, and A. Loidl, Phys. Rev. B **75**, 052410 (2007).

[101] C. J. Fennie and K. M. Rabe, Phys. Rev. B **72**, 214123 (2005).

[102] J. Preudhomme and P. Tarte, Spectrochimca. Acta. **27A**, 1817 (1971).

[103] K. Thirunavukkuarasu, F. Lichtenberg, and C. A. Kuntscher, Cndens. Matter. **18**, 9173 (2006).

[104] H. D. Lutz, J. Himmrich, and J. Haeuseler, Z. Naturforsch. **45a**, 893 (1990).

[105] C. Kringe, B. Oft, V. Schellenschläger, and H. D. Lutz, J. Mol. Struct **596**, 25 (2001).

[106] H. D. Lutz and H. Haeuseler, J. Mol. Struct. **511-512**, 69 (1999).

[107] J. Zwinscher and H. D. Lutz, J. Alloys Compd. **219**, 103 (1995).

[108] J. Himmrich and H. D. Lutz, J. Solid State Comm. **79**, 447 (1991).

[109] R. Ruckamp, E. Benckiser, M. W. Haverkort, H. Roth, T. Lorenz, A. Freimuth, L. Jongen, A. Moller, G. Meyer, P. Reutler, B. Büchner, A. Revcolevschi, S.-W. Cheong, C. Sekar, G. Krabbes, and M. Grüninger, New J. Phys. **7**, 144 (2005).

[110] S. Sugane, Y. Tanabe, and H. Kamimura, *Multiplets of transition-metal ions in crystals* (Academic Press, New York and London., 1970).

[111] A. Waśkowska, L. Gerward, J. S. Olsen, and E. Malicka, J. Phys.: Condens. Matter **14**, 12423 (2002).

[112] A. Waśkowska, L. Gerward, J. S. Olsen, M. Feliz, R. Llusar, L. Gracia, M.Marqúes, and J. M. Recio, J. Phys.: Condens. Matter **16**, 53 (2004).

[113] S. K. S. Z. Wang, P. Lazor and G. Artioli, J. Solid State Chem. **165**, 165 (2002).

[114] P. K. Larsen and S. Wittekoek, Phys. Rev. Lett. **29**, 1597 (1972).

[115] L. L. Golik, Z. Kunkova, T. Aminov, and G. Shabunina, Phys. Solid State. **38**, 717 (1996).

[116] C. K. Jorgensen, Inorg. Chem. Acta Rev. **2**, 65 (1968).

[117] B. N. Figgis, *Introduction to legend fields* (Robert E. Krieger publishing company,INC, Krieger Drive, Malabar, Florida 32950, 1986).

[118] G. Harbeke and H. Pinch, Phys. Rev. Lett. **17**, 1090 (1966).

[119] E. Callen, Phys. Rev. Lett. **20**, 1045 (1968).

[120] R. White, Phys. Rev. Lett. **23**, 858 (1969).

[121] T. Kambara and Y. Tanabe, J. Phys. Soc. Jpn. **28**, 628 (1970).

[122] H. Lehmann and G. Harbeke, Phys. Rev. B. **1**, 319 (1970).

[123] S. Berger and L. Ekstrom, Phys. Rev. Lett. **23**, 1499 (1969).

[124] S. Wittekoek and P. Bongers, Solid State Commun. **7**, 1719 (1969).

[125] S. Wittekoek and P. Bongers, Solid State Commun. **8**, 1281 (1969).

[126] H. Szymczak, W. Wardzyński, and A. Pajaczkowska, J. Magn. Magn. Mater. **15-18**, 841 (1980).

[127] M. Taniguchi, A. Fujimori, and S. Suga, Solid State Commun. **70**, 191 (1989).

[128] C. A. Kuntscher, M. Klemm, S. Horn, M. Sing, and R. Claessen, EUR. Phys. J **180**, 29 (2010).

[129] S. Blanco-Canosa, F. Rivadulla, V. Pardo, D. Baldomir, J.-S. Zhou, M. Garcia-Hernandez, M. A. Lopez-Quintela, J. Rivas, and J. Goodenough, Phys. Rev. Lett. **99**, 187201 (2007).

[130] Y. Ueda, N. Fujiwara, and H. Yasuoka, J. Phys. Soc. Jpn **66**, 778 (1997).

[131] M. Reehuis, A.Krimmel, N.Büttgen, A.Loidl, and A. Prokofiev, Eur. Phys. J. B. **35**, 311 (2003).

[132] P. Radaelli, New J. Phys **7**, 53 (2005).

[133] H. Mamiya, M. Onoda, T. Furubayashi, J. Tang, and I. Nakatani, (1997).

[134] V. Pardo, S. Blanco-Canosa, F. Rivadulla, D. I. Khomskii, D. Baldomir, H. Wu, and J. Rivas, Phys. Rev. Lett. **101**, 256403 (2008).

[135] T. Maitra and R. Valenti´, Phys. Rev. Lett **99**, 126401 (2007).

[136] H. Tsunetsugu and Y. Motome, Phys. Rev. B **68**, 060405(R) (2003).

[137] S. D. Matteo, G. Jackeli, and N. B. Perkins, Phys. Rev. B **72**, 020208(R) (2005).

[138] S. H. Jung, J. H. Noh1, J. Kim, C. L. Zhang, S. W. Cheong, and E. J. Choi, (2008).

[139] D. Baldomir, V. Pardo, S. Blanco-Canosa, F. Rivadulla, J. Rivas, A. Pineiro, and J. Arias, Physica B. **403**, 1639 (2008).

[140] Z. Zhang, D. Louca, A. Visinoiu, S.-H. Lee, J. D. Thompson, T. Proffen, A. Llobet, Y. Qiu, S. Park, and Y. Ueda, (2006).

Acknowledgements

In the name of almighty ALLAH, the most merciful and beneficent, who blessed with knowledge and enabled me to fulfill this task successfully. All respects are for His Holy Prophet Muhammad (peace be upon him) who is forever a torch of guidance and knowledge for humanity.

First and foremost, I would like to express my deep gratitudes to my supervisor, Prof. Dr. Christine Kuntscher for providing me an opportunity to work in her group. She endowed me with continuous guidance, valuable suggestions during my PhD project.

Many thanks to group members; Abid Karim, Ahmed Abouelsayed, Ali Al-Hadithy, Jihaan Ebad Allah and Anis Badawi, for helping me whenever i needed them. I am thankful to my friends who are/were also my colleagues Estaline Amitha Francis, Dr. Komalavalli Thirunavukkuarasu, Sindu John Louis and Dr. Leonetta Baldassarre and Dr. Simone Frank for their suggestion, encouragement, fruitful discussion, and moral support during this work . My deepest sense of aknowledgement goes to Dr. Alexej Pashkin for his cooperation and also his supervision to get start with Vis-UV microspectrometer project of my thesis. I am thankful to Kathrin Mattern and Armin Huber for their later help (part of their projects) to improve Vis-UV microspectrometer. I am grateful to Dr. Joachim Deisenhofer for his timely help in reading my thesis and his valuable suggestion to improve the same. I convey my thanks to Ms. Beate Spörhase for her technical assistants. I also thank all my other friends who have helped me through this journey in their own way.

I can never forget the cooperation, encouragement and guidance of Prof. M. Zafar Iqbal and I am thankful to him. Last but not the least, I thank my parents, brothers and sisters who always support me. They are my strength, without their support it would have been impossible for me to pursue my PhD. I am thankful of my husband Ali Bin Bakhtiar for his patience, encouragement and support during the last phase of this work.

Curriculum Vitae

Personal information

Date of birth	:	14 May 1977
Nationality	:	Pakistani
Gender	:	Female
Martial status	:	Married

Education

March 1983 - March 1994	Secondary School Examination, Dera Ghazi Khan Board, Pakistan.
August 1994 - August 1999	Bachelor's degree in Physics, Bahauddin Zakariya University, Multan, Pakistan.
September 1999 - December 2001	Master's degree in Physics, Islamia University Bahawalpur, Pakistan.
August 2003 - August 2005	M.Phil in Physics, Quaid-i-Azam University, Islamabad, Pakistan. Title: *Temperature Dependence of Optical Absorption by Common Impurities in Silicon.*
August 2005 - February 2007	Master's degree in Material Science, Linköping University, Sweden. Title: *An Electron Paramagnetic Resonance study of Defects in Electron-irradiated 3C-SiC.*
March 2007 - May 2012	Ph.D in Physics, Universität Augsburg, Germany. Title: *Structural and optical properties of transition-metal compounds under pressure.*

List of publications

- Metal-insulator transition in $NiS_{2-x}Se_x$.
  J. Kunes, L. Baldassarre, B. Schächner, K. Rabia, C. A. Kuntscher, Dm. M. Korotin, V. I. Anisimov, J. A. McLeod, E. Z. Kurmaev, and A. Moewes,
  Phys. Rev. B. **81**, 035122 (2010).

- High-pressure XRD study of $\beta-Na_{0.33}V_2O_5$.
  K. Rabia, A. Pashkin, S. Frank, G. Obermeier, S. Horn, M. Hanfland, and C. A. Kuntscher,
  High Pressure Research. **29**, 504 (2009).

- High-pressure Phase Transition and Properties of Cu_3N: An Experimental and Theoretical Study.
  Aron Wosylus, Ulrich Schwarz, Lev Akserlrud, Matt G. Tucker, Michael Hanfland, Kaneez Rabia, Christine Kuntscher, Jörg van Appen, Richard Dronskowski, Dieter Rau and Rainer Niewa,
  ZAAC. **635**, 1959 (2009).

- Effect of high pressure on multiferroic $BiFeO_3$.
  R. Haumont, P. Bouvier, A. Pashkin, K. Rabia, S. Frank, B.Dkhil, W. A. Crichton, C. A. Kuntscher, and J. Kreisel,
  Phys. Rev. B. **79**, 184110 (2009).

- Electron Paramagnetic Resonance study on n-type electronirradiated 3C-SiC.
  P. Carlsson, K. Rabia, N. T. Son, T. Ohshima, N. Morishita, H. Itoh, J. Isoya and E. Janzén,
  Journal of Physics: Conference Series. **100**, 042032 (2008).